

Defining Machine Capability of Metals Additive Manufacturing Machines

Master's thesis in Master Programme Materials Engineering

THOMAS DAM
NAPON RAVIRUJIPHANT

MASTER'S THESIS 2018

Defining Machine Capability for Metals Additive Manufacturing Machines

THOMAS DAM
NAPON RAVIRUJIPHANT



CHALMERS
UNIVERSITY OF TECHNOLOGY

Department of Industrial and Materials Science
Division of Product Development
Geometry Assurance & Robust Design
CHALMERS UNIVERSITY OF TECHNOLOGY
Gothenburg, Sweden 2017

Defining Machine Capability for Metals Additive Manufacturing Machines
THOMAS DAM
NAPON RAVIRUJIPHANT

© THOMAS DAM, NAPON RAVIRUJIPHANT, 2018.

Industrial Supervisor: Johan Berglund, Swerea IVF
Academic Supervisor: Vaishak Ramesh Sagar, Department of Industrial and Materials Science
Examiner: Kristina Wärmefjord, Department of Industrial and Materials Science

Master's Thesis 2018
Department of Industrial and Materials Science
Division of Product Development
Geometry Assurance & Robust Design
Chalmers University of Technology
SE-412 96 Gothenburg
Telephone +46 31 772 1000

Cover: Areal surface roughness profile and 3D scanned mesh points cloud as extracted from the sample build.

Printed by Chalmers University of Technology
Gothenburg, Sweden 2018

Defining Machine Capability for Metals Additive Manufacturing Machines
THOMAS DAM
NAPON RAVIRUJIPHANT
Department of Industrial and Materials Science
Chalmers University of Technology

Abstract

Additive manufacturing of metal parts has opened up another opportunity for the industries by allowing unlimited possibilities revolving around the choices of product design as well as internal features. Still, a problem arises when the surface integrity and geometrical accuracy are involved. The aim of the thesis is to determine the machine capability of metal AM machines in terms of geometrical accuracy, surface area roughness and chemical composition. A test artifact which can reflect the geometrical accuracy as well as positional accuracy had been developed as a part of the investigation. Model stability and alignment were kept in mind during the design. Two builds of the test artifact were manufactured with the SLM 125 HL machine with the material 316L and 410. One build was manufactured in 316L with the EOS M290 machine. The geometrical acquisition and inspection is done in combination with the ATOS III Triple Scan 3D scanner and the GOM Inspect software. The surface area roughness acquisition was performed with the optical microscope Sensofar S neox. MountainsMap was used to process the result with noise filter, form removal and calculate desired parameters. The microstructure and chemical composition was analyzed using an SEM with an EDS detector. The geometrical inspection result was highly dependent on the positioning system of the test artifact. The trend in geometrical accuracy was commonly shared between builds of different material from the same machine but not the ones of same material by different machine. The surface evaluation shows that the surface area roughness parameters do not change with height, position or orientation on the vertical surfaces of the test artifact. SLM 125 HL produced parts with similar surface area roughness parameters using two different materials. While the build from EOS M290 showed significantly higher surface area roughness parameter values that might be due to powder condition, process parameters or machine itself. The 316L build from SLM showed no difference in chemical composition in the bulk material for different height or position so further analysis on the other two builds was not performed.

Keywords: additive, manufacturing, geometry, assurance, capability, machine, SLM, EOS, roughness, surface

Acknowledgements

We would like to express our gratitude to our supervisor Johan Berglund at Swerea IVF for the thesis opportunity and supervision during the thesis period. Special thanks goes to our examiner Kristina Wärmefjord at Chalmers University of Technology for her guidance and support throughout the thesis.

Many thanks goes to our colleagues at Swerea IVF, Anton Dahl-Jendelin, Lars-Olof Ingemarsson and Per-Johan Wahlborg, for their help and service in the field of AM and GD&T. We would like to acknowledge Monica Cristea and Melina Da Silva for their support in materials characterization.

Finally, last but not least we would also like to acknowledge the staffs at Chalmers University of Technology, Marie Fischer, Vaishak Ramesh Sagar and Rikard Söderberg, for their feedback and support.

Thomas Dam and Napon Ravirujiphant, Gothenburg, June 2018

Contents

List of Figures	xiii
List of Tables	xv
1 Introduction	1
1.1 Background	1
1.2 Aim	1
1.3 Limitations	1
1.4 Specification of issue under investigation	1
2 Theory	3
2.1 Capability	3
2.1.1 Machine and process capability	4
2.2 Geometrical Dimensioning and Tolerancing	5
2.2.1 Tolerances of Location	7
2.2.1.1 Position	7
2.2.2 Test artifact for AM	7
2.2.2.1 NIST test artifact	8
2.3 SLM-machine	9
2.3.1 Process Parameters	9
2.3.1.1 Build Direction	9
2.3.1.2 Scan Strategy	10
2.3.1.3 Hatch Angle	12
2.3.1.4 Energy Density	13
2.3.2 Metal Powder	14
2.3.2.1 Powder Morphology	14
2.3.2.2 Powder Granulometry	14
2.3.2.3 Powder Surface Chemistry	15
2.3.2.4 Powder Packing Density	16
2.3.2.5 Powder Rheology	17
2.3.2.6 Powder Thermal Properties	17
2.3.2.7 Optical properties	17
2.3.3 Heat Treatment	18
2.4 Geometrical Assurance	18
2.4.1 3D Scanner	18
2.4.2 Geometry Evaluation	19

2.4.3	3-2-1 Alignment	19
2.5	Surface Roughness	19
2.5.1	Surface Profile Acquisition	19
2.5.1.1	Focus Variation Microscopy	20
2.5.1.2	Confocal Microscopy	20
2.5.1.3	Coherence Scanning Interferometry	21
2.5.1.4	Confocal Fusion	22
2.5.2	Surface Profile Analysis	23
2.5.2.1	Arithmetical Mean Height, Sa	23
2.5.2.2	Root Mean Square Height, Sq	23
2.5.2.3	Skewness, Ssk	23
2.5.2.4	Kurtosis, Sku	24
2.5.2.5	Root Mean Square Gradient, Sdq	24
2.5.2.6	Developed Interfacial Area Ratio, Sdr	24
2.5.2.7	Texture Aspect Ratio, Str	24
2.5.2.8	Texture Direction, Std	25
2.6	Microstructure	25
2.6.1	Scanning Electron Microscopy	25
2.6.1.1	Secondary electron	25
2.6.1.2	Backscattered electron	26
2.6.1.3	Characteristic X-ray	26
2.7	Sources of variations	27
2.7.1	Machine variations and errors	27
2.7.2	Process parameter variations and errors	28
2.7.3	Material variations and errors	28
2.7.4	Measurement variations and errors	28
2.7.5	Inspection variations and errors	29
2.7.6	Model variations and errors	29
3	Methods	31
3.1	Design of model	31
3.2	Build volume test artifact	31
3.2.1	Revision of build volume test artifact	34
3.2.2	Model stability	35
3.3	AM machine settings and process parameters	37
3.4	Measurement strategy	37
3.4.1	3D scanner measurement strategy	37
3.4.2	Surface area roughness measurement strategy	38
3.5	Inspection strategy	39
3.5.1	Geometry inspection strategy	39
3.5.2	Surface area roughness inspection strategy	41
3.6	Microstructure and chemical composition analysis strategy	41
3.6.1	Sample preparation	41
3.6.2	Microstructure and chemical composition analysis	43
4	Results	45
4.1	Geometrical analysis	45

4.1.1	Acquisition of geometry	45
4.1.2	X-, Y-, Z-direction and sphere diameter accuracy	46
4.1.2.1	Alignment 1	46
4.1.2.2	Alignment 2	50
4.1.3	Reference spheres and locating scheme	54
4.2	Surface area roughness analysis	54
4.2.1	Acquisition of surface area roughness	55
4.2.2	Overall height, spatial and hybrid parameter	55
4.2.3	Surface roughness parameters at different heights	58
4.2.4	Surface roughness parameters at same orientation	59
4.2.5	Surface area roughness anomalies	60
4.3	Microstructure and chemical analysis	63
4.3.1	Microstructure difference at different positions and heights	63
4.3.2	EDS spectrum and quantification	66
5	Conclusion	71
5.1	Methodology	71
5.2	Geometrical accuracy of laser beam melting additive manufacturing	71
5.3	Surface area roughness of laser beam melting additive manufacturing	72
5.4	Microstructure and chemical composition	72
5.5	Discussion	73
	Bibliography	75
A	Appendix 1	I
A.1	Geometrical inspection	I
A.1.1	316L-SLM; Alignment 1	I
A.1.2	316L-EOS; Alignment 1	I
A.1.3	410-SLM; Alignment 1	II
A.1.4	316L-SLM; Alignment 2	II
A.1.5	316L-EOS; Alignment 2	II
A.1.6	410-SLM; Alignment 2	III
A.2	Surface area roughness measurements	IV
A.2.1	316L-SLM	IV
A.2.2	316L-EOS	V
A.2.3	410-SLM	VI

List of Figures

2.1	A normal curve and its standard deviation σ tolerance limits.	4
2.2	Illustration of natural machine deviation and natural process deviation.	5
2.3	Example of a feature control frame and positional tolerancing.	6
2.4	3D-CAD model of the NIST test artifact.	9
2.5	Common scan strategies used in SLM process [8].	11
2.6	Stripe pattern scan strategy.	12
2.7	Examples of hatch angles and respective interval number.	12
2.8	Spherical 316L powder produced by gas atomization method (left); Irregular shape 316L powder produced by water atomization method (right) [14].	14
2.9	Examples of different particle size distribution [15].	15
2.10	D_{10} , D_{50} , D_{90} in cumulative density function curve [15].	15
2.11	Bi-modal relationship between volume fraction of small and large par- ticle vs packing density.	16
2.12	Schematic of transmission, reflection and absorption phenomena.	18
2.13	Focus variation microscopy working principle schematic.	20
2.14	Confocal microscopy working principle schematic.	20
2.15	Overall surface roughness profile (upper left); Conjugate points with respect to height for the lowest layer (upper right), middle layer (lower left) and highest layer (lower right).	21
2.16	Coherence scanning interferometry working principle schematic.	21
2.17	An interaction volume with signals emitting from different depth.	26
3.1	Build volume test artifact with the lowest height configuration.	32
3.2	Build volume test artifact assembly.	32
3.3	Top view of the build volume test artifact assembly.	33
3.4	Drawing of the build volume test artifact assembly.	33
3.5	Samples classified by row number.	34
3.6	Top view of the revised build volume test artifact assembly.	35
3.7	Stability analysis of the build volume test artifact with first locating scheme configuration.	36
3.8	Stability analysis of the build volume test artifact with second locat- ing scheme configuration.	36
3.9	Measurement area specified by area marked in red.	38
3.10	Nomenclature of sides name according to the sample orientation.	39
3.11	Locations of reference spheres (hatched) along with their locking axes.	40

3.12	Alternative locating scheme.	40
3.13	Locations of the cross sections of interest on the 100 mm sample.	41
3.14	Nomenclature of the 100 mm samples.	42
4.1	Shiny surface leads to missing data points.	45
4.2	Surface comparison between two different scans of 316L-EOS.	46
4.3	Deviation of each sample on 316L-SLM build under alignment 1.	47
4.4	Deviation of each sample on 316L-EOS build under alignment 1.	48
4.5	Deviation of each sample on 410-SLM build under alignment 1.	48
4.6	Tolerance limits for the deviation in geometrical accuracy and sphere diameter of 316L-SLM under alignment 1.	49
4.7	Tolerance limits for the deviation in geometrical accuracy and sphere diameter of 316L-EOS under alignment 1.	49
4.8	Tolerance limits for the deviation in geometrical accuracy and sphere diameter of 410-SLM under alignment 1.	50
4.9	Deviation of each sample on 316L-SLM build under alignment 2.	51
4.10	Deviation of each sample on 316L-EOS build under alignment 2.	51
4.11	Deviation of each sample on 410-SLM build under alignment 2.	52
4.12	Tolerance limits for the deviation in geometrical accuracy and sphere diameter of 316L-SLM under alignment 2.	53
4.13	Tolerance limits for the deviation in geometrical accuracy and sphere diameter of 316L-EOS under alignment 2.	53
4.14	Tolerance limits for the deviation in geometrical accuracy and sphere diameter of 410-SLM under alignment 2.	54
4.15	Surface texture of sample 20 mm s1 y- from 316L-SLM.	55
4.16	Diagram of Sa and Sq for 316L-SLM, 316L-EOS and 410-SLM.	57
4.17	Diagrams of Sdr, Sdq, Ssk and Sku for 316L-SLM, 316L-EOS and 410-SLM.	58
4.18	Overview of the 100 mm s1 x+ surface from the 316L-SLM build.	60
4.19	Surface area roughness image of 100 mm s1 x+ band 2 from the 316L-SLM build. Top image is before form removal, middle image is form removed and bottom image is after form removal.	61
4.20	Surface area roughness image of 20 mm s2 x- from the 316L-SLM build.	62
4.21	Surface area roughness image of 20 mm s2 x- from the 410-SLM build.	63
4.22	SE and BSE images of sample 1A, 1B and 2A at 50x magnification	64
4.23	SE and BSE images of sample 2B, 3A and 3B at 50x magnification.	65
4.24	SE and BSE images of sample 1A, 1B and 2A at 50x magnification.	66
4.25	EDS spectra of the 316L build.	67
4.26	Elemental mapping of Fe, Cr and Ni in the 316L build by Swerea.	68
4.27	Elemental mapping of Mo, C and Mn in the 316L build by Swerea.	69
4.28	Elemental mapping of S, Si and O in the 316L build by Swerea.	70

List of Tables

2.1	Standard deviation tolerance limits with its corresponding percentage of parts produced within tolerance limits.	4
2.2	Geometric tolerancing chart.	6
2.3	Example of features for geometrical tolerance evaluation.	8
2.4	A summary of the main sources of variations.	27
2.5	A summary of the main sources of variations (continued).	27
3.1	AM machine settings and process parameters.	37
3.2	Summary of all the grinding and polishing steps.	43
4.1	Average deviation in X- and Y- direction and their standard deviation for 316L-SLM, 316L-EOS and 410-SLM under alignment 1.	47
4.2	Tolerance limits for the deviation in geometrical accuracy and sphere diameter under alignment 1: 316L-SLM, 316L-EOS and 410-SLM.	49
4.3	Average deviation in X- and Y- direction and their standard deviation for 316L-SLM, 316L-EOS and 410-SLM under alignment 2.	50
4.4	Tolerance limits for the deviation in geometrical accuracy and sphere diameter under alignment 2: 316L-SLM, 316L-EOS and 410-SLM.	52
4.5	Deviation in X-, Y- and Z-direction of the reference spheres in 316L-SLM, 316L-EOS and 410-SLM.	54
4.6	Non-measured points ratio and its standard deviation for the builds: 316L-SLM, 316L-EOS and 410-SLM.	55
4.7	Average height, spatial and hybrid parameters with corresponding standard deviation for the builds: 316L-SLM, 316L-EOS and 410-SLM.	56
4.8	Tolerance limits for the height parameters for the builds: 316L-SLM, 316L-EOS and 410-SLM.	56
4.9	Tolerance limits for the spatial and hybrid parameters for the builds: 316L-SLM, 316L-EOS and 410-SLM.	56
4.10	Height, spatial and hybrid parameters for the 316L-SLM build at different heights.	58
4.11	Height, spatial and hybrid parameters for the 316L-EOS build at different heights.	59
4.12	Height, spatial and hybrid parameters for the 410-SLM build at different heights.	59
4.13	Height, spatial and hybrid parameters for the 316L-SLM build for different orientations	59

4.14	Height, spatial and hybrid parameters for the 316L-EOS build for different orientations.	59
4.15	Height, spatial and hybrid parameters for the 410-SLM build for different orientations.	60
4.16	Height, spatial and hybrid parameters for the 100 mm s1 x+ band 2 surface before and after form removal.	62
4.17	Height, spatial and hybrid parameters for the 20 mm s2 x- surfaces from the 316L-SLM and 410-SLM builds.	63
4.18	Chemical composition of the 316L build.	66

1

Introduction

This chapter presents the background of the thesis, problem formulation, aim and limitations.

1.1 Background

Additive manufacturing (AM) of metal parts has shown its promising capability in regard to an industrializing aspect. AM allows production of parts with unlimited possibilities revolving around the achievable design as compared to conventional machining. Internal structure tinkering is performed easily with AM allowing the products to attain striking properties such as lightweight while preserving the functionality. The main concern about metal part AM arises when the surface integrity, residual stresses and microstructure are involved. Without any finishing process, the manufactured AM parts are considered to have rough surface which can lead to a problematic situation in an industrial scale. At the moment, the understanding with respect to geometrical tolerance and machine capability is insufficient.

1.2 Aim

The aim is to determine the machine capability of metal AM machines in terms of geometrical accuracy, surface area roughness and chemical composition by developing a novel methodology.

1.3 Limitations

The thesis work will not cover the quality assurance in terms of microstructural effects and residual stresses, instead only macroscopic and microscopic dimensional accuracy will be concentrated on. In additions, the AM machines are limited to machines from SLM Solutions at Swerea IVF and EOS at Chalmers.

1.4 Specification of issue under investigation

Currently, the knowledge behind quality assurance of AM parts is limited as different machines and process parameters are being used. Hence, a more designated protocol

is desired in order to get a predictable printing product. The thesis aims to answer the following questions regarding quality assurance:

- How does X-, Y-, Z-position accuracy vary with build height and build location?
- How does the surface area roughness vary with build height, build location and build orientation?
- Is a sphere a valid model for alignment and evaluating positional accuracy?
- Will a different material affect the positional accuracy and surface area roughness?
- Will a different AM machine with its own recommended process parameters have a different positional accuracy and surface area roughness?
- How does the material affect the measurement strategy for the part?
- Does the chemical composition change with build height or build location?

2

Theory

This chapter covers the literature study performed on the subject geometry assurance relevant to metal additive manufacturing. Background information on the equipment used during the thesis is also covered.

2.1 Capability

Capability is defined as the ability of a process to produce products according to a specified requirements [1]. This definition is wide to cover all processes and different types of capabilities such as machine capability and process capability. A capability value is calculated statistically by defining a tolerance range for important parameters and gathering a measured data set of the parameters. A process with a high capability value has the ability produce most products within specified tolerance range. The capability value can be manipulated by changing the tolerance range without any change in the data set. That means a "good" capability value cannot be defined and the calculated value has to be evaluated individually. A commonly used target capability value is 1.33 (=4/3). 1.33 is equivalent to a tolerance limits range of $\pm 3.99\sigma$ which gives a probability value of 0.999967 [2]. That is the probability that any given value within the data set used is inside the tolerance limits. Process capability and machine capability are calculated using equations 2.1 and 2.2. The equations assumes a normal distribution when calculating the capability value. The standard deviation is multiplied by six to give a tolerance limits of $\pm 3\sigma$.

$$C_p = \frac{T_u - T_l}{6\sigma} \quad (2.1)$$

$$C_m = \frac{T_u - T_l}{6\sigma} \quad (2.2)$$

where C_p is the process capability
 C_m is the machine capability
 T_u is the upper tolerance limit
 T_l is the lower tolerance limit
 σ is the standard deviation

The standard deviation σ is calculated with equation 2.3.

$$\sigma = \sqrt{\frac{\sum_{i=1}^n (x_i - \mu)^2}{n}} \quad (2.3)$$

where x_i is a i -th value from the data set
 μ is the mean value of the data set
 n is the data set size

Figure 2.1 illustrates the normal distribution curve with its tolerance limits marked out with steps of one standard deviation. A normal curve is symmetrical and always has the same shape. The area under the curve in each standard deviation tolerance limit step corresponds to a percentage of values that is within the tolerance limit. Examples of the percentage of values for one, two and three standard deviation is shown in table 2.1. Other values with higher amount of standard deviations exists.

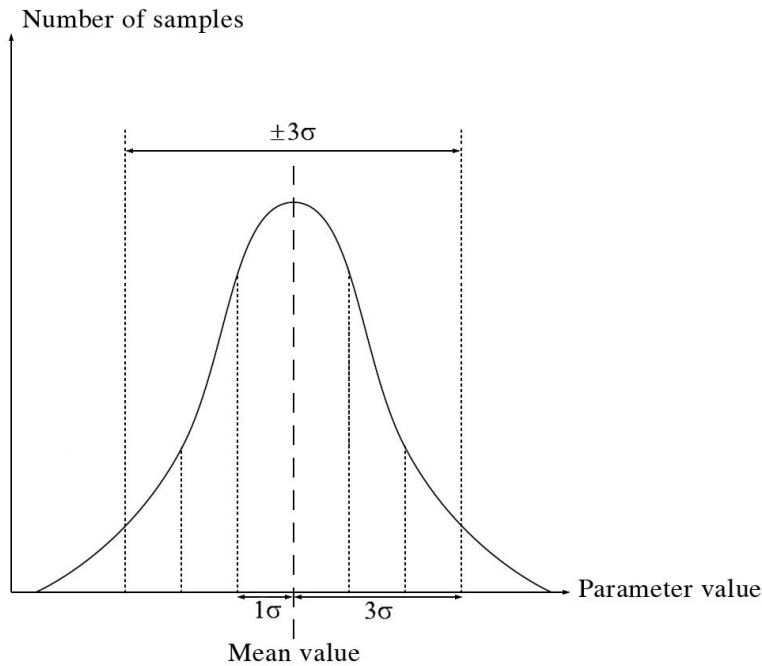


Figure 2.1: A normal curve and its standard deviation σ tolerance limits.

Table 2.1: Standard deviation tolerance limits with its corresponding percentage of parts produced within tolerance limits.

Standard deviation tolerance limits	% of parts within tolerance limits
$\pm 1\sigma$	68.26 %
$\pm 2\sigma$	95.46 %
$\pm 3\sigma$	99.73 %

2.1.1 Machine and process capability

The equation for machine capability and process capability are near identical but the data set used for them are different and is gathered in a different way. For studying the machine capability, variations have to be minimized, e.g. for AM, same material and powder size needs to be chosen. On the other hand, process

capability studies a process's performance with influence from different material and input settings. Process capability has to be studied for a longer time period and include all variations that influence the production process. Figure 2.2 shows how the natural machine deviation changes with time because of variations such as different material and input settings. The natural process variation take account of the natural machine deviation with time.

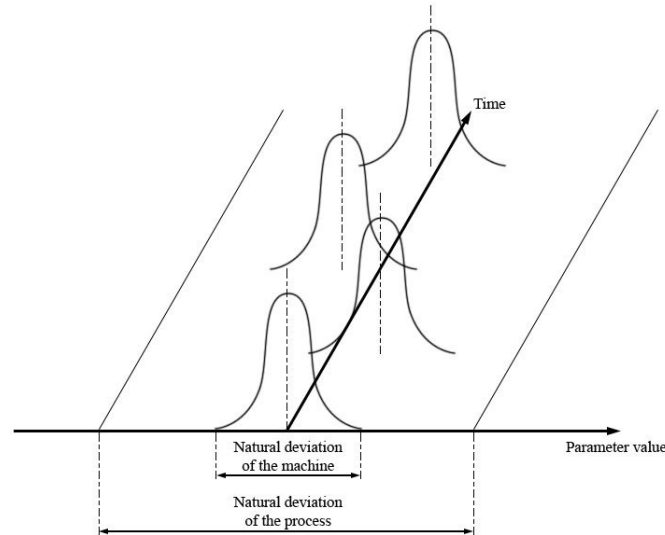


Figure 2.2: Illustration of natural machine deviation and natural process deviation.

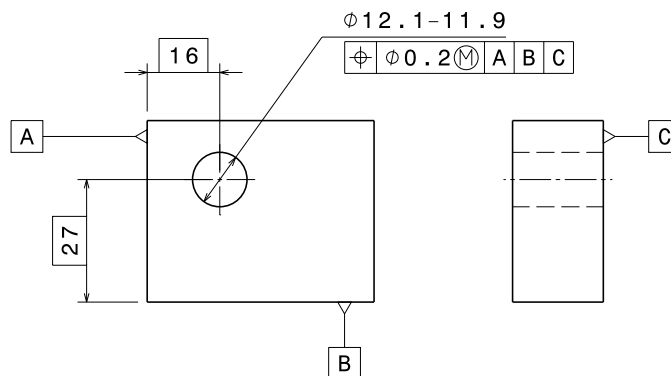
2.2 Geometrical Dimensioning and Tolerancing

Geometrical Dimensioning and Tolerancing (GD&T) is a standardized system used for defining and communicating engineering tolerances such as the size, shape, form, orientation, and location of features on a part. It describes the nominal geometry and the allowed tolerances of a part. GD&T allows more control over the tolerances than the traditional plus and minus tolerancing system. The geometrical characteristics defined by The American Society of Mechanical Engineers (ASME) are shown in table 2.2 Geometric tolerancing chart [3].

Table 2.2: Geometric tolerancing chart.

Tolerance	Geometric characteristic	Symbol
Form	Flatness	\square
Form	Straightness	—
Form	Circularity	\circ
Form	Cylindricity	⌀
Profile	Profile of a line	\frown
Profile	Profile of a surface	\cap
Orientation	Perpendicularity	\perp
Orientation	Angularity	\sphericalangle
Orientation	Parallelism	\parallel
Location	Symmetry	\equiv
Location	Position	\oplus
Location	Concentricity	\odot
Run-out	Circular run-out	\nearrow
Run-out	Total run-out	\nearrow

International Organization for Standardization (ISO) has their own standards for GD&T which has a few differences compared with the standard from ASME. For instance, the ISO standards are split up into multiple documents such as ISO 286 and ISO 1101, etc, whereas the latter one describes form, orientation, location, and run-out. One conceptual difference between the ASME and ISO standards that form and size is controlled at the same time under ASME but they are independent under the ISO standard if it is not specified with the Envelope principle. There are also nomenclature differences. The geometrical characteristics are used in feature control frames along with a tolerance, modifiers and datum references to specify tolerances in drawings. An example of a feature control frame is shown in figure 2.3. In this example, the position tolerance is used in the feature control frame.

**Figure 2.3:** Example of a feature control frame and positional tolerancing.

Dimensions and geometry of a produced part are always subject to variation which is why tolerances are needed. The same goes for geometrical characteristics which are of interest in geometry assurance. The tolerances are widely used in the industry to ensure produced parts meet their functional requirements set by the design [4].

2.2.1 Tolerances of Location

The principles of tolerances of location for position are established in this subsection. Other geometrical characteristics are outside the scope of the thesis.

2.2.1.1 Position

Position is the location of a feature relative to one or several features or one or several datums. Positional tolerancing defines the zone of which a feature's center, axis or center plane may lie within. Material conditions such as LMC (Least Material Condition), MMC (Maximum Material Condition) and RFS (Regardless of Feature Size) can be applied to positional tolerancing. In figure 2.3, positional tolerancing with MMC is applied to a hole with datums A,B and C. The true position of the hole is shown with basic dimensions.

2.2.2 Test artifact for AM

In manufacturing metrology, there are two common approaches for measuring machine performance, one is by direct measurements on the machine itself and the second one is by producing a test artifact. The common way to benchmark the capability of an AM machine is by using test artifacts as it is difficult to mount sensors to the moving components of an AM machine for instance[5]. Test artifacts are designed to evaluate the geometrical accuracy, repeatability and minimum feature size of the machine. Repeatability in this case refers to building the same geometry at a different location. Process repeatability is not measured. Many different designs of test artifacts have been produced to evaluate different parameters or suit a specific machine, they range from simple to complex. Nonetheless, the test artifacts are usually composed of simple features such as pins, holes, squares, cones, stairs, wedge and other fine features to test the geometrical tolerance of the machine. Rebaioli et. al. reviewed a wide amount test artifacts for geometrical performance evaluation and have summarized the main general features used to evaluate the geometrical tolerances [6]. It is shown in table 2.3. One of the most common test feature for AM machines are overhangs. Overhangs test the steepest building angle and how the surface roughness changes with the angle. The roughness will change because the underside will fuse with the powder under it during melting and the top side is affected by the staircase effect. The building angle affects the design of features such as horizontal holes, lattice structure and the overall part orientation. The disadvantage of test artifacts is the difficulty to directly link a specific part error in the test artifact to a specific part of the machine because there are multiple machine errors that can contribute to a part error.

Table 2.3: Example of features for geometrical tolerance evaluation.

Tolerance	Feature
Flatness	Cubes, slots, rectangular bosses, thin walls, base surface
Straightness	Cubes, slots, rectangular bosses, thin walls, base surface
Circularity	Circular holes, cylinders
Parallelism	Cubes, rectangular bosses and holes, thin walls, square holes
Perpendicularity	Cubes, circular bosses and holes, square holes
Cylindricity	Circular holes, solid and hollow cylinders
Angularity	Inclined surfaces
Position	Holes, cylinders
Profile	Spheres, hemispheres

There is no standardized test artifact available yet but one is under development by ISO and ASTM International (ASTM) under the title ISO/ASTM CD 52902. However, National Institute of Standardization and Technology (NIST) has published their own test artifact intended for standardization [5]. The design contains simple features mentioned before and a guideline on measuring and evaluation of the physical part.

2.2.2.1 NIST test artifact

The design of the NIST test artifact is inspired by previously proposed AM test artifacts and machining test artifacts. The artifact is shown in figure 2.4. The model characterizes the geometrical accuracy of the AM machine and its limitation e.g. minimum feature size. Practical problems, such as measuring, are also considered. It was designed to be measured with commonly available equipments such as coordinate measuring machine (CMM), 3D scanner, optical microscope, etc. The model is orientated in such a way to minimize the impact from the recoater blade that spreads the powder over the build plate. No support structures are used in the model to reduce post-processing. It is built directly on the building plate instead. The test artifact does not evaluate the entire build volume of the AM machine due to long build time and material cost of a larger part. The main limitation is in evaluating the accuracy in Z-direction.

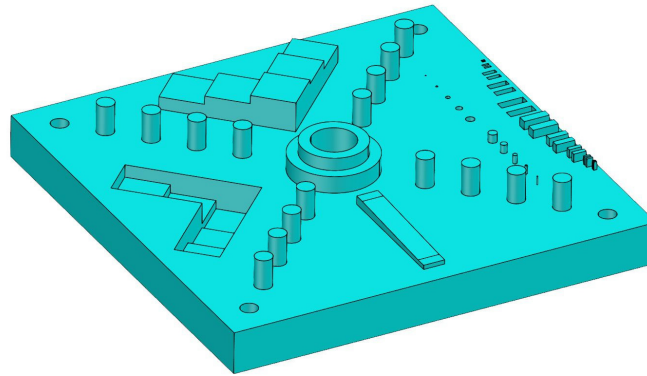


Figure 2.4: 3D-CAD model of the NIST test artifact.

2.3 SLM-machine

Selective Laser Melting (SLM) is an additive manufacturing process which has its underlying working principle based on that of Powder Bed Fusion (PBF) technique. The SLM process has been designed for melting metal powder bed due to high power density laser input. Initially, 3D-CAD model is imported into the SLM machine as 2D sliced-up layers designated with printing pattern on each layer. The SLM process is set in motion by first spreading powder bed onto the build plate. Laser is then guided onto several locations on the powder bed according to the printing pattern on that specific layer, melting the powder bed in process. Once all locations specified by the printing pattern on that layer have been exposed to the laser, the build plate is lowered according to the layer height which cooperates with how the 3D-CAD model is sliced and the printing process continues for the upcoming layers. The process is repeated until every layer has been printed resulting in a additive manufactured part. Laser pattern can be either sequential or random.

2.3.1 Process Parameters

The term 'Process parameters' only concern parameters in pre-processing steps. Varying process parameters can contribute to the deviating final mechanical and geometrical build properties. Across different machines, unfitting process parameters can give rise to many sources of variations. Hence, process parameters must be carefully controlled otherwise the final can be undesirable. Such process parameters are build direction, scan strategy, hatch angle and energy density.

2.3.1.1 Build Direction

Since laser path is in lateral direction while grain growth direction is in transverse direction, how the part model has been oriented will have a significant effect on mechanical property of the build. W.Shifeng et al. has investigated that stainless steel 316L shows higher strength and ductility when the manufactured part has its longitudinal axis parallel to the vertical axis of AM machine as compared to the part

that has its longitudinal axis parallel to the horizontal axis of AM machine [7]. The reason behind such occurrence is the grain texture which is elongated grains along the build direction but this trend is not always true. EOS company tested a flat and cylindrical sample using MaragingSteel MS1 as printing material and the result shows that Young's Modulus, yield strength, ultimate tensile strength and ductility of horizontally printed part exhibits higher values than those of the vertically printed part. Hence, the build geometry and build direction alone are not only governing the mechanical properties but also the type of material.

2.3.1.2 Scan Strategy

Laser scan strategy can greatly affected the microstructure of the build. Two commonly known laser scan strategies are 'line' scan strategy and 'island' scan strategy. 'Line' scan strategy is where the laser beam travels back and forth after each hatch is melted while 'island' scan strategy divides the print pattern into checkerboard pattern that contains several small squares in which each square is exposed to the melting laser randomly. Both scan strategies along with other scan strategies are depicted in figure 2.5.

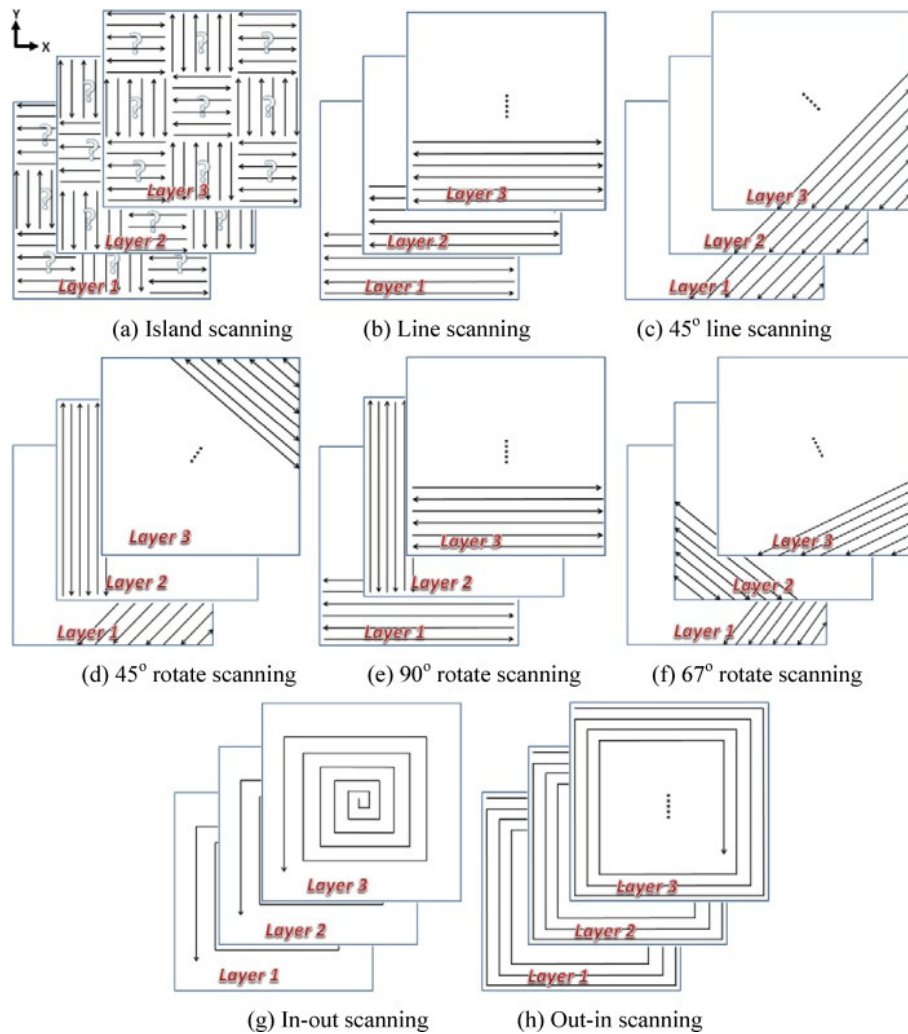


Figure 2.5: Common scan strategies used in SLM process [8].

Luke N. Carter et al. had studied the effect of selected scan strategy on the microstructure [9]. The grains appear to be homogeneously elongated as the 'back-and-forth' scan strategy was applied while bimodal texture between elongated grains and fine equiaxed grains was obtained when 'island' scan strategy was implemented. This study has emphasized the scan strategy effect on grain texture.

The scan strategy implemented in manufacturing samples used in this thesis is the stripe pattern in which its characteristic is governed by hatch distance, stripe width and overlapping area. Stripe scanning strategy is illustrated in figure 2.6.

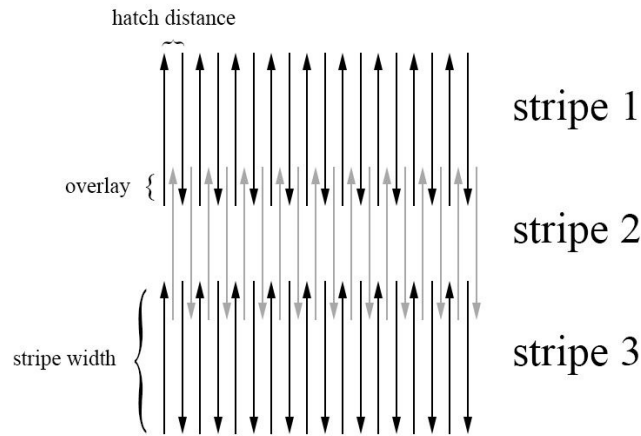


Figure 2.6: Stripe pattern scan strategy.

2.3.1.3 Hatch Angle

Hatch angle is the angle of the laser direction changed between consecutive layers. Hence, hatch angle of 0° means that every layer is printed in the same direction. Hatch angle of 90° implies that 4 layers need to be printed before the laser direction comes back to the original direction. These aforementioned 4 layers indicates the 'interval number', layers required until the laser direction is the same as the starting direction. The interval number (N) of hatch angle (θ) is calculated through the equation:

$$N = \frac{360^\circ}{gcd(\theta, 360^\circ)} \quad (2.4)$$

where $gcd(\theta, 360^\circ)$ is the greatest common divisor between θ and 360° .

A study by Kai Guan et al. of Stainless Steel 304 with differing hatch angles has concluded that the mechanical properties are proportionally related to the interval number [10]. But a study by Christ P. Paul et al. has, in contrast to Kai Guan et al., found out that mechanical properties of Inconel 625 are insensitive to different hatch angles [11]. Therefore, the conclusion on the actual effect of hatch angle is still debatable. Figure 2.7 gives examples of hatch angles and their interval number.

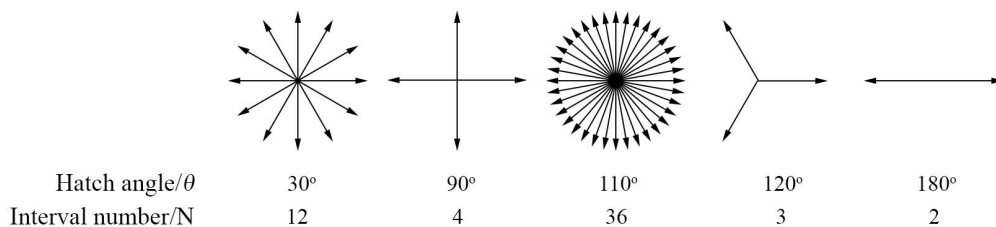


Figure 2.7: Examples of hatch angles and respective interval number.

2.3.1.4 Energy Density

The term 'Energy Density' describes the amount of heat per volume the powder bed is subjected to. Energy density is also another crucial parameter that determines the melt characteristic of the powder. Four main parameters that governs the energy density are laser beam power, scanning speed, hatch distance and layer thickness.

Laser Beam Power Laser beam power is defined by the input energy from the laser per time unit.

Scanning Speed Laser moves along the guided line according to the sliced-up layer with the velocity designated as scanning speed. Faster scanning speed means less exposure time.

Hatch Distance Distance between the centers of the two adjacent laser beams on the scanning pattern. Low hatch distance means more overlapping area.

Layer Thickness Layer thickness is, as stated by the name, thickness of each layer of the build. Layer thickness is directly related to the volume of the powder bed being fused. In addition, layer thickness has also been shown to be connected to the outcome of the staircase effect which affects the surface roughness of the build.

Combination of the four parameters contributes to the energy density and the melt pool characteristics. A simple way to visualize each parameter is to look at them as amount of energy input, exposure time, overlapping area, and powder volume for laser beam power, scanning speed, hatch distance and layer thickness, respectively. Equation 2.5 shows the relationship between energy density and the four parameters [12]:

$$E = \frac{P}{\nu * h * t} \quad (2.5)$$

where E is the energy density in [J/mm³]
 P is the power of the laser in [W]
 ν is the scanning speed in [mm/s]
 h is the hatch distance in [mm]
 t is the layer thickness in [mm]

Unoptimized energy density could lead to an undesirable melt pool characteristics and print quality. Having too low energy density will result in an incomplete melting which gives rise to many defects such as porosity and lack of fusion. On the other way round, too high power can cause evaporation of the melt pool. Laser beam profile (e.g. uniform, Gaussian) should also be specified since the melt pool width and penetration depth vary between different laser beam profiles [13].

2.3.2 Metal Powder

Aside from processing parameters, metal powder used in AM process can influence the result of the final build as well. Main powder characteristics that will be discussed are powder morphology, powder granulometry, surface chemistry, packing density, powder rheology, thermal properties and its optical properties.

2.3.2.1 Powder Morphology

Metal powder exists in many forms with different size and shape since metal powder can be prepared through various preparation methods or subjected to variform conditions. For an instance, metal powder manufactured by gas atomization and water atomization can have totally different morphology. Another example includes metal powder manufactured by the same preparation method but one is virgin powder and another is recycled powder. Powder overall appearance can be similar among the two nonetheless their morphologies can diverge and greatly affect the final build quality. As elaborated by Sheng Zhang et al., aerosol spherical powder and water atomized irregular powder in figure 2.8, with same processing parameters, yield higher and lower bulk density, respectively [14]. Morphology of the powder can affect the powder packing density, hence the volume shrinkage; lower packing density means more volume shrinkage. Factors such as coefficient of friction, wettability and particle contact area are also affected by the powder morphology as well.

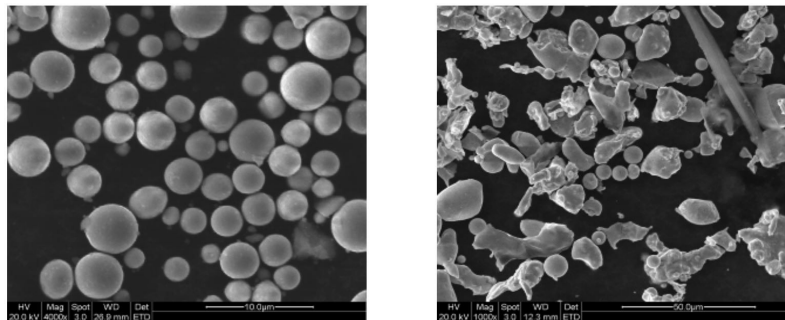


Figure 2.8: Spherical 316L powder produced by gas atomization method (left); Irregular shape 316L powder produced by water atomization method (right) [14].

2.3.2.2 Powder Granulometry

Granulometry, or particle size distribution (PSD), is a terminology used for addressing particle sizes in terms of composition. PSD is usually represented by a size versus volume percentage graph as shown in figure 2.9 or by size gauges (D_{10} , D_{50} , D_{90}) shown in figure 2.10; by saying $D_x = y$, it means that $x\%$ of the total powder has its size less than y . PSD can be altered through out the AM process with, for example, recycling of powder. Mean of PSD curve will shift towards the larger size after recycling possibly due to droplets ejected from the melt pool that drops down to the powder bed and stick to the unmelted particles resulting in a larger irregular shape particle. PSD can be tweaked by sieving the powder or adding a powder to

obtain the preferred PSD [15]. Broad PSD will allow the powder to have higher flowability, better packing density and more particle contact area.

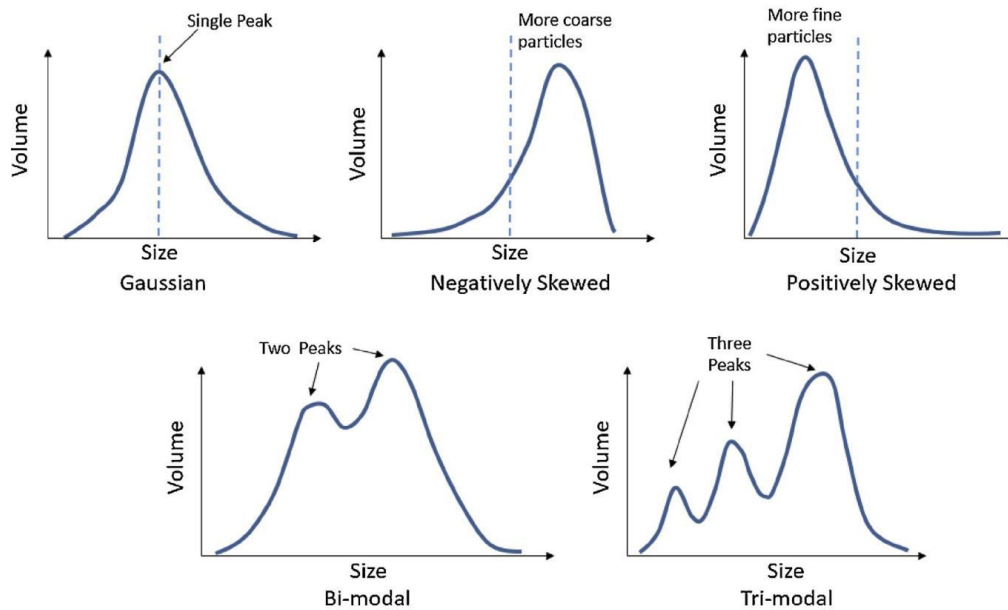


Figure 2.9: Examples of different particle size distribution [15].

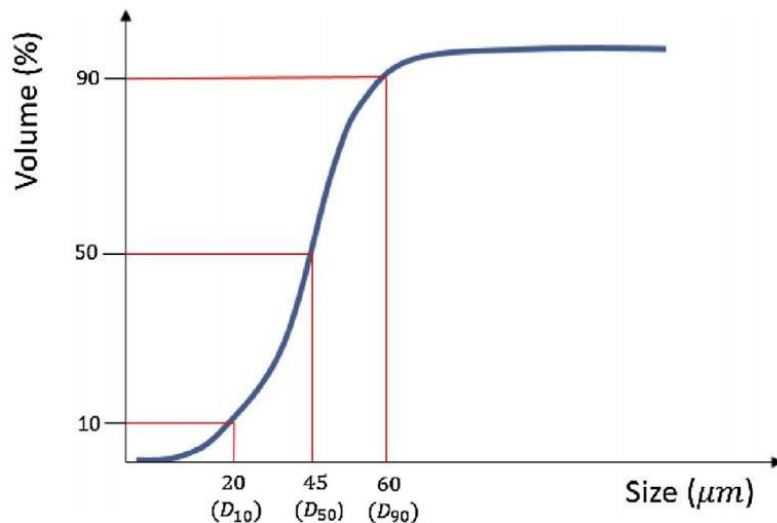


Figure 2.10: D_{10} , D_{50} , D_{90} in cumulative density function curve [15].

2.3.2.3 Powder Surface Chemistry

For assuring low-defects build from AM process, the powder used usually has fine size and, preferably, spherical shape. Fine spherical powder comes with high surface area as well as surface energy and this makes surface chemistry another important aspect of the powder characteristics. One notorious example would be Oxygen. Oxygen content associated in metal AM process can threaten the build integrity by oxidation

reactions of the powder during the printing process [16]. An oxidation reaction leads to formation of an oxide film which lower wettability between consecutive layers. Unstable and low wettability melt pool will shrink into a spherical shape and promote balling effect [17]. Therefore, the powder used in the SLM process should have high initial purity and the least possible contamination from the environment. The process itself should be operated under controlled inert atmosphere and the unsintered powder that will be used in consecutive builds should have a record of previous builds to keep track of the general trend of the contamination concentration.

2.3.2.4 Powder Packing Density

Powder packing density is a parameter that state how well the powder is packed. The key to obtain maximum particle contact area is to maximize the powder packing density. As mentioned before, the factors that affect the powder packing density are morphology and PSD. In addition to those, resultant forces between each particle will determine the coefficient of friction of the powder bed which affect the flow of the powder bed during spreading step [15]. Powder packing density shows how much void volume exists which governs how many layers are required before achieving the stable effective layer thickness; melted consecutive powder bed layer will fill in the void fraction first, and for that reason, the first few layers will not have stable effective layer thickness [18]. Also, poorly packed powder can result in higher void fraction which would lead to higher shrinkage after consolidation. Figure 2.11 illustrates the relationship between volume fraction of small and large particle and the packing density.

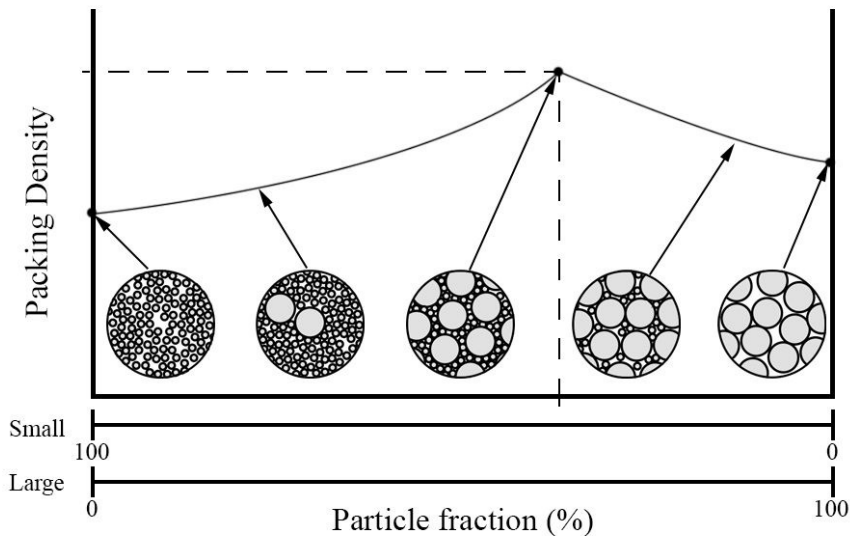


Figure 2.11: Bi-modal relationship between volume fraction of small and large particle vs packing density.

2.3.2.5 Powder Rheology

Powder rheology is more concerned in term of flowability, the ability for something to flow. Fine powder with broad PSD can flow and behave like liquid. Factors affecting flowability are, again, powder morphology, PSD and powder surface chemistry [15]. Flowability is described through the parameter called *Hausner Ratio* (H). Hausner ratio is evaluated by the following equation

$$H = \frac{\rho_T}{\rho_B} \quad (2.6)$$

where ρ_T is the tap density and ρ_B is the apparent density. Indication of friction conditions between powder particle is perceived through Hausner ratio [19]. High flowability will allow the powder spread to be homogeneous. With Hausner ratio higher than 1.25, the powder is considered to possess poor flowability. Different standards can be applied to measuring the tap density making values of tap density dependent on methodology.

2.3.2.6 Powder Thermal Properties

Powder thermal properties connect the powder characteristics and the processing parameters. Heat capacitance and melting temperature of the material are directly related to the layer thickness and the energy density. Thermal conductivity is related to powder packing density. It describes how efficient can heat be conducted either through the solidified layers or the powder bed. Coefficient of thermal expansion, in cooperation with void fraction, dictates the amount of shrinkage expected after the build is completed [15].

2.3.2.7 Optical properties

When electromagnetic wave propagates through a barrier between medium with different refractive indices, it can succumb to three phenomena, *Transmission*, *Reflection* and *Absorption*, which are represented in term of fractions of the incident energy by *Transmittance* (T), *Reflectance* (R) and *Absorptance* (A), respectively [20] as illustrated in figure 2.12. The relationship between the three terms is governed by:

$$T + R + A = 1 \quad (2.7)$$

Both *transmission* and *reflection* are scattering processes which are enhanced in the powder bed due to void space that promotes the scattering effect. Scattering effect allows the laser to penetrate deeper into the powder bed layer while another portion of energy is undergoing an *absorption* process which is wavelength dependent. Nd-YAG laser which has a wavelength of about 1.06 μm has been shown to be more absorbed by metallic powders when compared to CO₂ laser which have a higher wavelength of 10.6 μm .

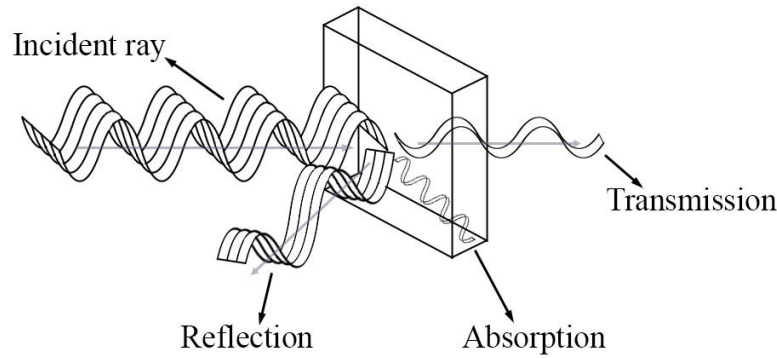


Figure 2.12: Schematic of transmission, reflection and absorption phenomena.

2.3.3 Heat Treatment

Due to the thermal gradient and cooldown of the top layer that occurs during the melting process, residual stresses arise in the parts produced by SLM additive manufacturing [21]. Deformations and cracks in the material can form because of the residual stresses. The amount of residual stresses is linked to thermal volume changes in the material when it cools down, the surface cools down faster than the core. The volume changes will produce thermal stresses which can be described by equation 2.8 [22].

$$\sigma_{th} = E \times \Delta T \times \alpha \quad (2.8)$$

where σ_{th} is thermal stress, E is the elastic modulus, ΔT is the temperature gradient and α is the thermal coefficient of expansion. Thermal stresses are highest for materials with both high modulus and coefficient of expansion. The thermal gradient is controlled by the cooling of the material and also the material's thermal conductivity. A high thermal conductivity reduces the thermal gradient due to higher rate of heat transfer. Materials such as tool steels tend to have higher residual stresses as phase transformation to martensite will cause volume changes. To reduce the residual stresses, heat treatment is performed on the manufactured parts while they are still attached to the build plate. The parts go through a stress relieving cycle at an elevated temperature. The cycle does not affect the grain size of the material.

2.4 Geometrical Assurance

The artifacts undergo a 3D scanning process following by geometry measurement done digitally by the designated software. Sphericity of the build along with effect of parts' orientations, locations and heights will be inspected.

2.4.1 3D Scanner

ATOS III Triple Scan functions through the means of *projection* and *acquisition*. *Projection* is initiated by a pattern of parallel light fringes being illuminated onto the interested surface where the *acquisition* is performed by having two cameras recording the distorted aforementioned pattern on the scanned surface [23].

ATOS III Triple Scan in particular applies “Blue Light Technology” to avoid interference of ambient light in the background. In one orientation, the scanned sample is subjected to fringes pattern with different frequencies for more sampling points hence higher resolution in each iteration. The sample is rotated after it has been fully scanned at specific orientation and is scanned with the same manner in the following orientations. A 3D mesh grid of the sample is obtained after it is scanned from all directions.

2.4.2 Geometry Evaluation

The 3D scanned mesh file is inspected according to the nominal CAD file through the use of GOM Inspect 2017 software. Several alignments regarding the nominal CAD file can be applied. The program is capable of making GD&T analysis. Since, the model will contain a sphere, one example of the aspects that will be looked into is the radius. Radius will be measured from the center of the sphere in several axes and sphericity can be evaluated. Effect of location, orientation and part height will also be observed as well. GOM Inspect 2017 is capable of yielding the surface comparison profile which can be translated into radius deviation map further in latter step of the inspection.

2.4.3 3-2-1 Alignment

3-2-1 Alignment, so called plane line point alignment, is a locating scheme that utilize 6 points to lock 6 degrees of freedom, 3 translations and 3 rotations. First 3 points selected, plane, are responsible for locking 1 translational axis and 2 rotational axes. Another 2 points selected, line, then proceed on locking another translational axis along with the last rotational axis. Finally, the last point locks the last rotational axis. 3-2-1 alignment should be done such that the deviation is kept as low as possible. The different location scheme and locking points will effect the outcome of the geometrical evaluation [24].

2.5 Surface Roughness

Surface roughness characterizes the surface texture through various parameters. The essence of surface roughness revolves around the post-manufacturing performance of the product in term of lifetime and capability.

2.5.1 Surface Profile Acquisition

Various modes of operation can be performed to achieve the surface profile depending on the required sampling area and resolution. The acquisition machine used is Sensofar S neox installed along with Accurion Halcyonics_i4 active vibration isolation platform allowing dynamical control over external vibration which reduce vibrational errors. The machine allows 3 modes of acquisition, namely, *focus variation microscopy*, *confocal microscopy*, and *coherence scanning interferometry*.

2.5.1.1 Focus Variation Microscopy

Height map created through the mean of *focus variation* solely relies on image processing operations. First, the image is taken at a starting focal plane with a fixed depth of field. The focus is then varied by an increment and then the next picture is taken. This process is repeated until the focus has swept across the designated sweeping range as specified by the user [25]. Height map is obtained numerically by the relationship between pixels that are in focus and focus distance of that image. *Focus variation microscopy* allows surface profiling of a steep surface at a lower magnification while its vertical and lateral resolution is limited to about 100 nm and several pixels, respectively. Acquired layers and how they stack is shown in figure 2.13.

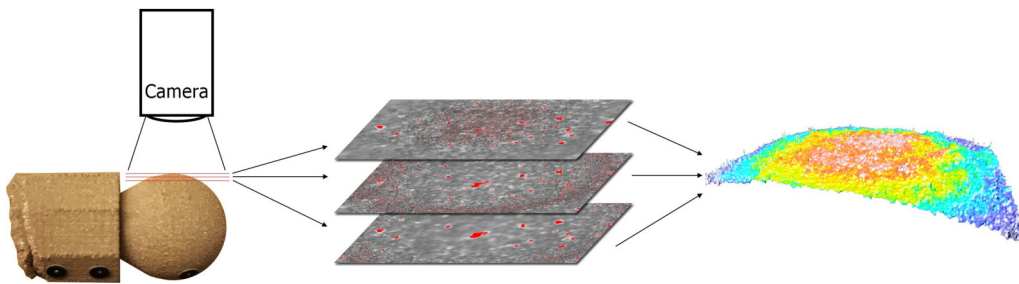


Figure 2.13: Focus variation microscopy working principle schematic.

2.5.1.2 Confocal Microscopy

Confocal microscopy places a pinhole at the confocal plane of the objective allowing signal only from conjugate points to be transmitted. For *confocal microscopy*, the conjugate points are the focal point of the objective and the confocal point at the aperture. Hence, all lights that are not a part of conjugate points, out-of-focus lights, will not reach the photodetector granting *confocal microscopy* very high vertical and lateral resolution [25]. Finer vertical resolution and conjugate points in confocal microscopy are seen in figure 2.14 and 2.15, respectively.

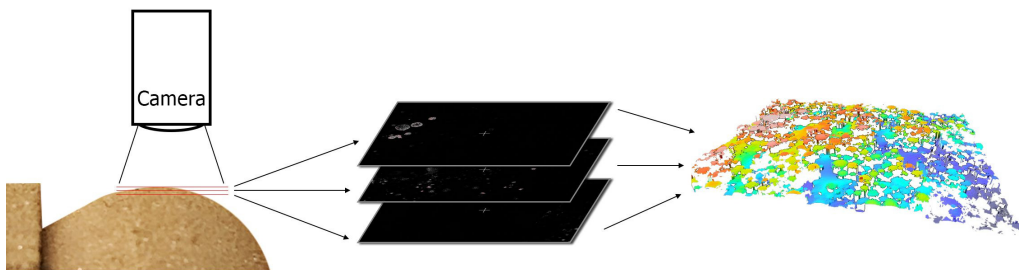


Figure 2.14: Confocal microscopy working principle schematic.

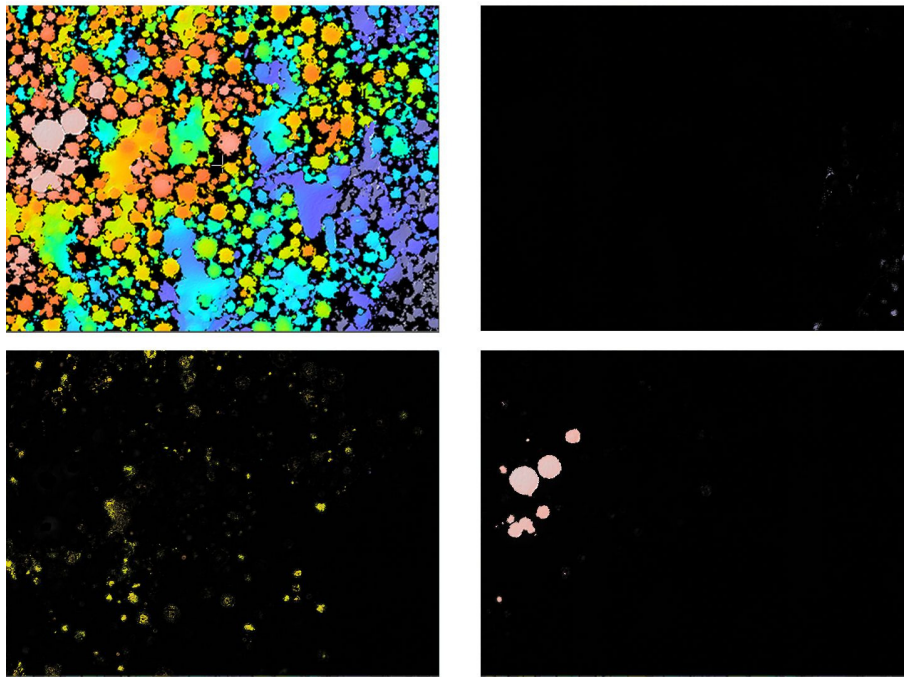


Figure 2.15: Overall surface roughness profile (upper left); Conjugate points with respect to height for the lowest layer (upper right), middle layer (lower left) and highest layer (lower right).

2.5.1.3 Coherence Scanning Interferometry

Coherence scanning interferometry (CSI) detects the surface height by identifying the locations where the interference effect of the infrared signal is most significant and is most constructive [25]. CSI has its lateral resolution of about $1\ \mu\text{m}$ and vertical resolution about $3\ \text{nm}$. As compared to *focus variation* and *confocal microscopy*, *coherence scanning interferometry* gives the finest vertical resolution as shown in figure 2.16.

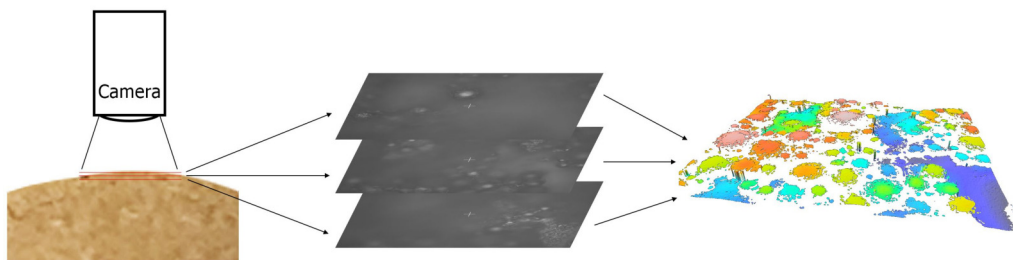


Figure 2.16: Coherence scanning interferometry working principle schematic.

For surface roughness in AM parts, the mode that will be used is called 'Confocal Fusion' which is using an algorithm that combines together for obtaining result with steep angle as well as fine lateral resolution.

2.5.1.4 Confocal Fusion

To simply explain the mechanism of *confocal fusion*, it can be said that *confocal fusion* is a mixture of the best of *confocal microscopy* and the fillers from *focus variation microscopy*. Before going into more details on *confocal fusion*, justification on why *coherence scanning interferometry* is not used should be stated first. CSI certainly gives the most accurate result in term of height resolution but CSI's underlying working mechanism and its optical pathway does not allow images to be sampled simultaneously but desirably with *focus variation microscopy* technique due to bright field image nature of *focus variation microscopy* that will decrease the dynamic range hence bright field contrast of the texture of the surface. *Focus variation microscopy* and *confocal microscopy* that is based on microdisplay, on the other hand, share similar optical sectioning characteristics and depth of focus property [26].

Confocal microscopy can take care of smooth surface better than *focus variation microscopy* while *focus variation microscopy* will help *confocal microscopy* out on the sample with rough surface. There are 3 main fusion techniques that are used in confocal fusion which will be easily explained below.

Topographical fusion	Data points from focus variation microscopy are added to the data points of the confocal microscopy according to the location of non-measured points in confocal microscopy.
Image fusion	Optically sectioned images from both techniques are averaged together into a new image plane which will then be stacked together to make a surface profile as the acquisition goes on.
Axial response pixel-by-pixel fusion	Each pixel undergoes a boolean statement that will decide whether the height value should come from either of the two techniques or a combination of both while preserving all of the accurate confocal pixels. This boolean statement is dependent on the signal strength and signal-to-noise ratio of confocal microscopy and focus variation microscopy.

Topological fusion can give good results but the algorithm itself is not dynamic unlike image fusion and axial response pixel-by-pixel fusion that is dynamic and can yield results with spatial frequencies close to confocal data.

2.5.2 Surface Profile Analysis

The obtained surface profile is analyzed through MountainsMap Premium 7.4 surface analysis software. The program is capable of mesh points interpolation, flat surface leveling and surface form removing. Flattened height maps can be utilized to yield many essential surface roughness parameters. Three-dimensional data set, areal profile, can allow abundant sampling points across the whole observed area. Calculations of all parameters are based on ISO 25178 standard in part 2.

2.5.2.1 Arithmetical Mean Height, Sa

Arithmetical mean height shows the average height of the height map [27]. For data mesh with a sampling area, A , with the measured height, $z(x, y)$, where x and y denote a coordinate, the surficial arithmetical mean height, Sa , is calculated by:

$$Sa = \frac{1}{A} \iint_A |z(x, y)| dx dy \quad (2.9)$$

Sa gives a quick review on how much the surface height map has varied from its mean plane. Sa can be less statistical significant when compared to root mean square height, Sq .

2.5.2.2 Root Mean Square Height, Sq

Root mean square height, Sq , is a parameter that announces the standard deviation of heights [27] and it can be calculated by:

$$Sq = \sqrt{\frac{1}{A} \iint_A z(x, y) dx dy} \quad (2.10)$$

where A and $z(x, y)$ are the same as the case of Sa .

Sa and Sq can be both misleading if implemented only by themselves since both parameters are insensitive to spacing and surface features such as peaks or valleys.

2.5.2.3 Skewness, Ssk

Skewness exhibits how the height distribution histogram is spread with respect to the mean plane [27]. The skewness value is governed by the equation,

$$Ssk = \frac{1}{Sq^3} \frac{1}{A} \iint_A z^3(x, y) dx dy. \quad (2.11)$$

The surface height distribution profile is symmetrical around the mean plane if the value of $Ssk = 0$. For $Ssk > 0$, the height distribution profile is skewed below the mean plane, vice versa for the case of $Ssk < 0$.

2.5.2.4 Kurtosis, Sk_u

Kurtosis states the sharpness of the surface height distribution profile [27]. Kurtosis value can be computed by

$$Sk_u = \frac{1}{Sq^4} \frac{1}{A} \iint_A z^4(x, y) dx dy. \quad (2.12)$$

When Sk_u is 3, the surface height distribution profile is expected to have the normal distribution curve while $Sk_u > 3$ indicates that the distribution is sharp. Lastly, $Sk_u < 3$ means that the distribution curve is skewed above the mean plane.

2.5.2.5 Root Mean Square Gradient, Sdq

Root mean square gradient, Sdq , represents root mean square of the surface slopes which can be useful to distinguish the surface texture of surfaces with similar Sa [27]. A completely flat surface will have the Sdq value of 0 and an increasing Sdq value with surface slope more than 0° . The parameter Sdq is calculated by:

$$Sdq = \sqrt{\frac{1}{A} \iint_A \left(\frac{\partial z^2}{\partial x} + \frac{\partial z^2}{\partial y} \right) dx dy} \quad (2.13)$$

where A is the projected area and z is the height map.

2.5.2.6 Developed Interfacial Area Ratio, Sdr

Developed interfacial area ratio, Sdr , is explained as a ratio between an interfacial area and a projected area on a flat plane [27]. Sdr is sensitive to both spacing and amplitude. Surfaces with same height variation but different spacing will give different Sdr ; smaller spacing gives more interfacial area to projected area ratio hence Sdr will be larger in this case. Sdr is calculated by:

$$\begin{aligned} Sdr &= \frac{\sum \sum A_{ij} - A}{A} \\ &= \frac{1}{A} \iint_A \left(\sqrt{1 + \frac{\partial z^2}{\partial x} + \frac{\partial z^2}{\partial y}} - 1 \right) dx dy \end{aligned} \quad (2.14)$$

where A and z are the same as the case of Sdq .

2.5.2.7 Texture Aspect Ratio, Str

To understand the texture aspect ratio, Str , the concept of autocorrelation function (ACF) must be elaborated first. ACF is a function describing similarity between the original surface, $z(x, y)$, and the original surface displaced by distance of Dx in x -direction and Dy in y -direction, $z(x-Dx, y-Dy)$. ACF is calculated by:

$$ACF(Dx, Dy) = \frac{\iint z(x, y)z(x - Dx, y - Dy) dx dy}{\iint z(x, y)^2 dx dy} \quad (2.15)$$

in which the value of ACF can range from +1 to -1 with +1 showing that Dx,Dy-displaced surface has perfect correlation with the original surface and 0 shows no correlation at all.

With autocorrelation plot, threshold can be applied and central lobe is obtained. The minimum radius, r_{min} , and the maximum radius, r_{max} , can be measured from the center of the central lobe to its perimeter and then used in Str calculation [27] :

$$Str = \frac{r_{min}}{r_{max}} \quad (2.16)$$

Str value is in between 0 and 1. If Str is close to 1, the surface texture is isotropic. In contrast, Str close to 0 indicates the anisotropy of the surface texture.

2.5.2.8 Texture Direction, Std

Std parameter is determined from the Fourier spectrum of the surface. Each spatial frequency is plotted according to their energy content in the Fourier spectrum. At a certain angle θ , the frequency amplitude ($A(\theta)$) can be calculated by integration of two selected spatial frequencies, f_{min} and f_{max} . $A(\theta)$ designates how much spatial frequency content is in that direction. The plot of $A(\theta)$ with θ from 0° to 180° gives semi-circular polar spectrum graph in which the maximum value of this plot is called the main texture direction or Std . Note that the value of Std is regarded as insignificant if Str lies in between 0.6 and 0.8 [27].

2.6 Microstructure

Due to an inhomogeneous nature of the atmosphere circulation in the printing chamber, the concentration of the burnt powders varies with different height and different location in the build volume. Hence, the microstructure is another aspect that needs to be investigated. Specifically, chemical composition will be discussed through elemental mapping with scanning electron microscopy. With the elemental map, the grain size and its distribution could furthermore be obtained.

2.6.1 Scanning Electron Microscopy

Scanning electron microscopy (SEM) is an electron imaging technique that relies on scanning of focused electron beam across the area of interest. SEM is capable of achieving a lateral resolution better than 1 nm. When an incident electron beam comes in contact with the interested surface, interaction volume will be created resulting in several signals that give more than just a visual overview of the surface. Such signals are secondary electrons (SE), backscattered electrons (BSE) and characteristic X-ray.

2.6.1.1 Secondary electron

Secondary electrons are generated from the interaction volume 5-50 nm down from the surface. SE have low energy of about 50 eV due to the inelastic scattering as a

result of energy loss or ejection of loosely bounded electron from a collision between incident electrons and the nucleus. SE signal is obtained through SE detector such as Everhart-Thornley detector and the obtained result is the topological image of the area of interest [28].

2.6.1.2 Backscattered electron

Backscattered electrons are a result of elastic scattering event from a collision of incident electrons with sample atom's core nucleus. Generated BSE will have higher energy than SE, 16-18 keV vs 3-5 eV, allowing the signal to escape from greater depth as compared to SE. Since the probability for the incident electrons to undergo elastic collision with the nucleus is directly proportional to the atomic number, the contrast in BSE imaging comes from difference in atomic numbers [28]. Therefore, BSE mode in SEM is a quick way to observe phase segregation and to look for inclusions.

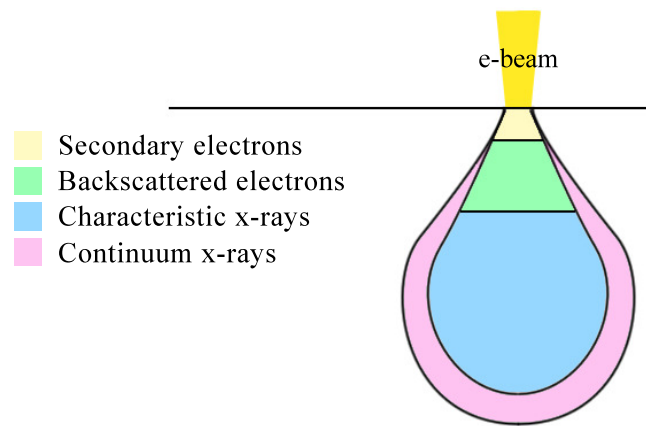


Figure 2.17: An interaction volume with signals emitting from different depth.

2.6.1.3 Characteristic X-ray

Further down from the surface, far beyond the escaping depth of backscattered electrons, the interaction volume can additionally give characteristic x-ray signal which allows semi-quantitative analysis of the chemical composition of the sample. The characteristic x-ray is generated by ejection and transition of electrons of the core atoms of the sample. With the sample being bombarded by electron beam gun, incident electrons can knock out or eject the electron that is initially bounded to the core atom. This ejection makes that core atom unstable. To retain stability, bounded electron in the outer core will transition itself into the unstable shell; this process is called transition. Since electrons from the outer shell have higher energy, in order to ensure complete transition, the atom from outer shell will need to release energy in form of x-ray. With each element possessing unique binding energy in each shell, the x-ray signal emitted from each element will always be unique hence it is called characteristic x-ray [28].

2.7 Sources of variations

Errors and variations from different sources that affect the end result are summarized in table 2.4 and table 2.5. The sources are sorted by different categories such as machine, process parameter, material, measurement, inspection and model. The sources are taken into consideration when designing, measuring, inspecting and evaluating the test artifact.

Table 2.4: A summary of the main sources of variations.

Machine	Process parameter	Material
Build plate geometry	Limited scan strategy	Material composition
Fixing of build plate	Hatch angle	Powder size
Ballscrew/stepper motor	Laser beam power	Powder morphology
Recoater	Scanning speed	Powder size distribution
Gas flow	Hatch distance	Heat treatment
Burnt powder	Layer thickness	Contaminations
Powder distribution	Laser beam profile	Thermal expansion
Laser beam size and shape		Shrinkage
Laser beam positioning		Residual stresses
		Defects

Table 2.5: A summary of the main sources of variations (continued).

Measurement	Inspection	Model
Pixel density of 3D scanner	Fitting of CAD model	Support structure
Resolution limit of optics	Reference points	Aspect ratio
Data points missing	Locating scheme	STL format
Measured area	Filtering	Model stability
Light settings		

2.7.1 Machine variations and errors

Machine variations refer to the errors and variations in the AM machine that could affect the print quality in terms of geometry, surface roughness, microstructure and chemical composition. The build plate geometry changes with every build job as the top surface is ground or milled to create a flat surface. The surface is also sandblasted to create an even surface texture. The height of the build plate changes so it has to be manually corrected in the AM machine by zeroing the build plate by eye. This leads to a thicker first layer of the build job. The build plate is fixed to the heating element by hand tightening normal screws. This leads to an uncertainty in the build plate position in x and y direction compared with the laser coordinates. The z position of the build plate is controlled by a ball screw using a stepper motor with no linear scale sensor that verifies its actual position. The recoater distributes the powder over the build plate and controls the height of the

powder bed with a rubber scraper. The recoater's alignment with the build plate can be fine adjusted and has a detrimental effect on the powder bed's height and powder distribution. Protective argon gas flow is used to protect the melt pool from oxidation. The gas flow can also move burnt powder from the melting spot to another position on the powder bed, contaminate the parts built and affect the chemical composition. It has been observed that parts furthest from the gas flow inlet are affected the most because the flow is only from one direction. The laser beam size, shape and positioning also varies [5]. From these machine variations, the build plate geometry, the recoater alignment, scraper blade quality can be controlled through proper maintenance. The rest of the variations is machine dependent.

2.7.2 Process parameter variations and errors

As discussed in section 2.3.1 '*Process Parameter*' and section 2.3.2 '*Metal Powder*', all the process parameters mentioned are related through the resultant energy density. Differing energy densities can result in different building time as well as different melt pool characteristics and build qualities.

2.7.3 Material variations and errors

Material variations refer to the powder used as raw material for the machine and also the machine's effect on the material itself. The variations are divided into powder quality, material properties of the powder and sources that affect the build quality in terms of material. Powder quality encompasses material composition, powder size, powder morphology and powder size distribution. These factors affect the overall build quality, e.g. mechanical properties, geometrical accuracy, surface roughness, microstructure and residual stress. Powder quality is controlled by using virgin powder or powder that has only been recycled once or twice. Recycled powder is always sieved to regain the desired powder size distribution and remove agglomerates. During the building process, a large thermal gradient exists between the melt pool and the printed part. Each material has its own specific coefficient of expansion and phase transformations sequence, which affect shrinkage and residual stresses in the part. High enough residual stresses will induce warping and cracks on the built parts.

2.7.4 Measurement variations and errors

Prior to 3D scanning, several set up parameters must be defined. Such parameters are camera resolution, measuring volume, measuring point distance, measuring distance, angle between cameras and number of rotations on the rotary plate. Those parameters remain constant or recalibrated on every scan to ensure no variations of the scanned mesh that occur by varying these parameters. Incorrectly scanned point can exist due to the stitching algorithm of the program that can mistakenly place the scanned point in the air, on the area that is not the surface of the build. These points are removed after the scan has been completed nonetheless they could result in variations in the scanned mesh if not treated properly. Reference stickers

adhered to the surface of the build can create inaccurate scan points on the surface because the stickers block a small area from being scanned. Greatest source of errors in the scanned mesh file can arise from the shiny surface of the build. Shiny surface can cause the scan points to be missing or inaccurate.

For areal surface roughness measurement, the method used for aligning the sample on the moving stage could lead to a non standardized and imprecise set up of the upcoming areal surface roughness measurement however extraction of the acquired data later on in inspection step will nullify the effect contributed by alignment of the samples. Parameters such as length per pixel, LED light and ring light intensity, magnification and acquisition mode stay the same throughout every acquisition. Unsuitable vertical sweeping range of the acquisition can generate the data set that is incomplete hence the vertical range of the acquisition is readjusted specifically for every surface to ensure optimal and close-to-complete acquisition.

2.7.5 Inspection variations and errors

Inspection refers to how the measured data is processed from the 3D scanning measurements and the surface area roughness measurements. For the 3D scanning inspection, fitting of the nominal CAD model to the measured data cloud is a large source of variation. The variation depends on what part of the measured data cloud is used as reference points and depends on what kind of locating scheme is used in the geometrical inspection software. The reference points used are from the build itself so they are subjected to variation from machine. To get comparable result, the locating scheme and reference points need to be the same for each build. For the surface area roughness inspection, filtering can be used to suppress anomalies from the measured data set, it can remove waviness or the roughness itself. Filtering can affect the end result significantly so it is important that an appropriate filter is used to extract the wanted data from the measurement.

2.7.6 Model variations and errors

The largest source of error in modelling for evaluating geometry and surface roughness is support structure in the model. Support structure can be built in different shapes with different parameters which give an uncertainty in stability of the structure. Removal of the support structure will affect the geometry and surface of the AM-part. The need for support structure is easily eliminated from the model by not designing large overhangs. Aspect ratio refers to the model's height to thickness ratio. A thin and tall model is unstable and creates a risk of being bent by the scraper blade that moves back and forth. It can be avoided by angling the model against the scraper blade or increasing the base thickness of the model. The format of the 3D CAD models are exported as STL. STL triangulates the surface of the model which makes it suitable for slicing by the data preparation software for importing to the AM machine. The amount of triangles determines the theoretical geometrical accuracy of the model. Setting the triangle small enough will negate the triangulation's effect on the accuracy within the tolerance of the machine. A

2. Theory

data preparation software can also fix errors such as bad edges or holes from the STL file. Model stability is the geometrical robustness of the model's sensitivity to deviation from varying locating scheme. A model with high sensitivity would amplify the deviation induced from a deviating locating scheme. By spreading out the locating points, the stability can be increased.

3

Methods

This chapter covers the design strategy of the test artifacts and overall strategy of measuring and inspecting the manufactured parts.

3.1 Design of model

The information gathered in the literature review of the AM test artifacts tells that there are no test artifacts meant for testing the entire build volume of the machine. Most models are designed to reduce the build time and material usage so the height of the models are low. The model is designed for evaluating the accuracy of geometries built high above the build plate as several factors (e.g. recoater, gas flow, ballscrew for the z-axis) can influence the accuracy of a part depending on the build height.

3.2 Build volume test artifact

The build volume test artifact has an octagonal base for a stable platform. The top of the octagon has a cone with a half sphere on it. An octagon gives multiple surfaces for surface roughness measurements at different angles. The height of the model is adjusted by the octagons's length between different models. The idea behind the spherical shape on the top of the test artifact is to maximize measuring points for locating the center point. All points on the surface of a sphere have the same distance to the center point. Thus makes it possible to evaluate the dimensional accuracy of the part in x-, y- and z-directions. It could not be a complete sphere due the practical problems such as large overhang, instability and worse surface roughness at the bottom. The cone has a conservative 60° angle. The sphere has a diameter of 10 mm and the octagonal base has the dimensions 10 by 10 mm. The models has three different heights ranging from 20 mm, 60 mm and 100 mm. The models are arranged to fit as a 3x3 matrix on the build plate over a 80 by 80 mm area. Even though the build plate is 125 by 125 mm, the holes for mounting the build plate has to be avoided and clearance to the edges is needed which leads to a smaller test area. Figure 3.1 shows the 3D-CAD model of the lowest height variation of the test artifact.

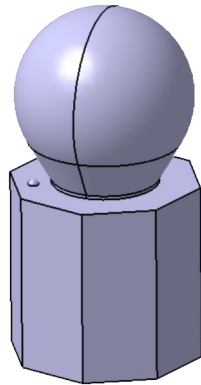


Figure 3.1: Build volume test artifact with the lowest height configuration.

There is a dot on top of the octagon base to help identifying the build orientation. The artifact is built with the dot facing the gas inlet. A 5x5 matrix was considered but experience from previous test builds suggested that it would be difficult to measure all the test artifacts without missing data points. The models would simply block the line of sight for the 3D scanner. The build volume test artifact uses a locating scheme that is built together with the test artifact. The locating scheme is the center point of three reference models surrounding the 3x3 matrix. The reference models look like the build volume test artifact but are shorter and have a cylindrical base instead. The reference models are spread out on the built plate to maximize geometrical stability. A 3x3 matrix of the test artifacts together with its reference models (labeled in green) is shown in figure 3.2.

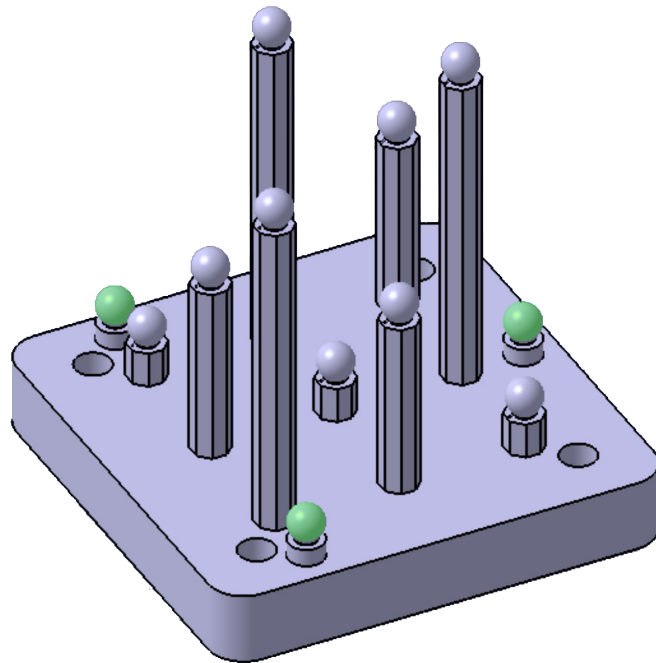


Figure 3.2: Build volume test artifact assembly.

A top view of the test artifact assembly is shown in figure 3.3. The three reference models are located outside of the 3x3 matrix.

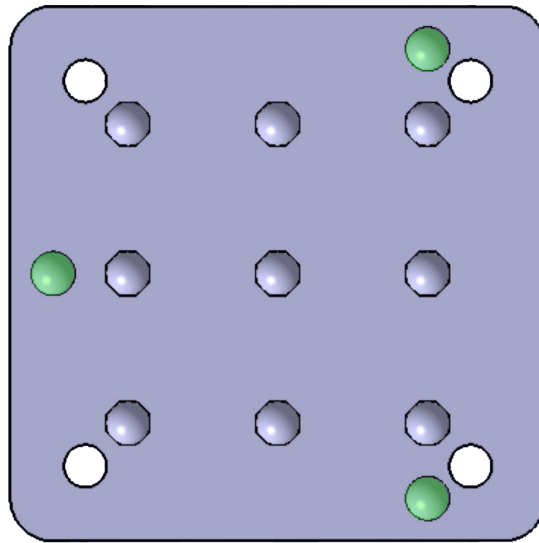


Figure 3.3: Top view of the build volume test artifact assembly.

Figure 3.4 shows a drawing of the assembly with the dimensions from the center point to the various models. The reference spheres used for alignment are also marked out.

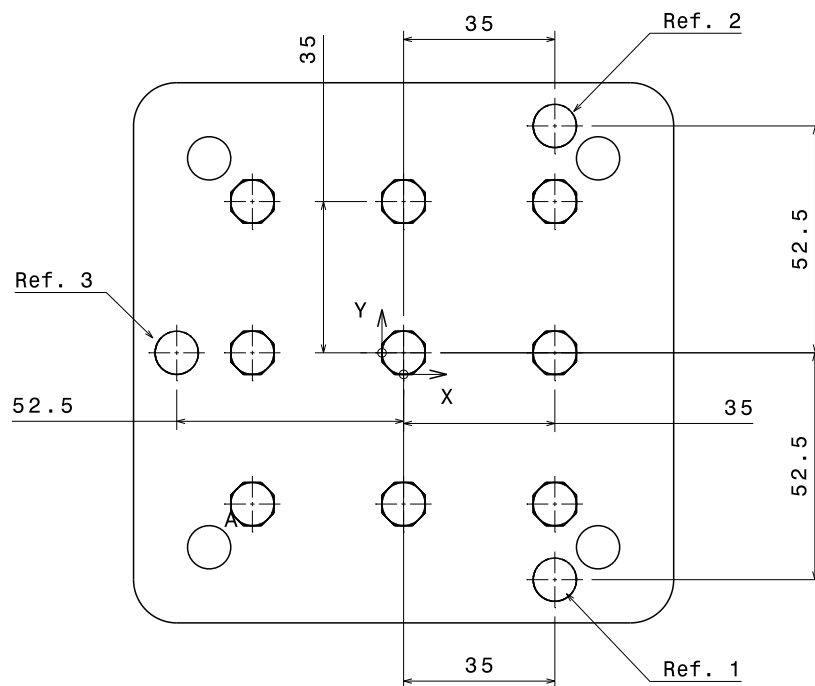


Figure 3.4: Drawing of the build volume test artifact assembly.

With this configuration, each sample is categorized by their respective row as designated in figure 3.5.

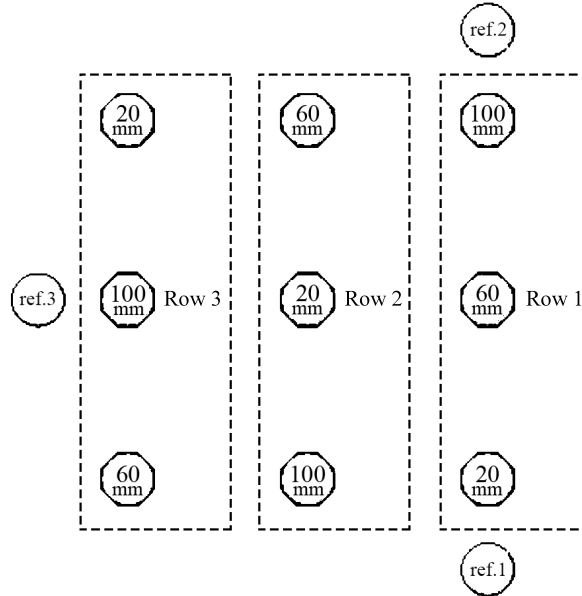


Figure 3.5: Samples classified by row number.

Each sample is named with the following format, "Material + Machine + Print Height + Row Number". For example, sample named "316L EOS 60mm 3" was manufactured by EOS M290 with 316L stainless steel and it is 60mm in height and placed in row 3 according to figure 3.5.

3.2.1 Revision of build volume test artifact

The first print job of the build volume test artifact showed that the reference spheres deviated from its nominal position by over 200 microns. Three additional reference spheres were added to the second revision of the build volume test artifact to get an optional locating scheme if the reference spheres were to deviate and affect the result. The position of the extra reference spheres (red) are mirrored from the original reference spheres (green). See figure 3.6.

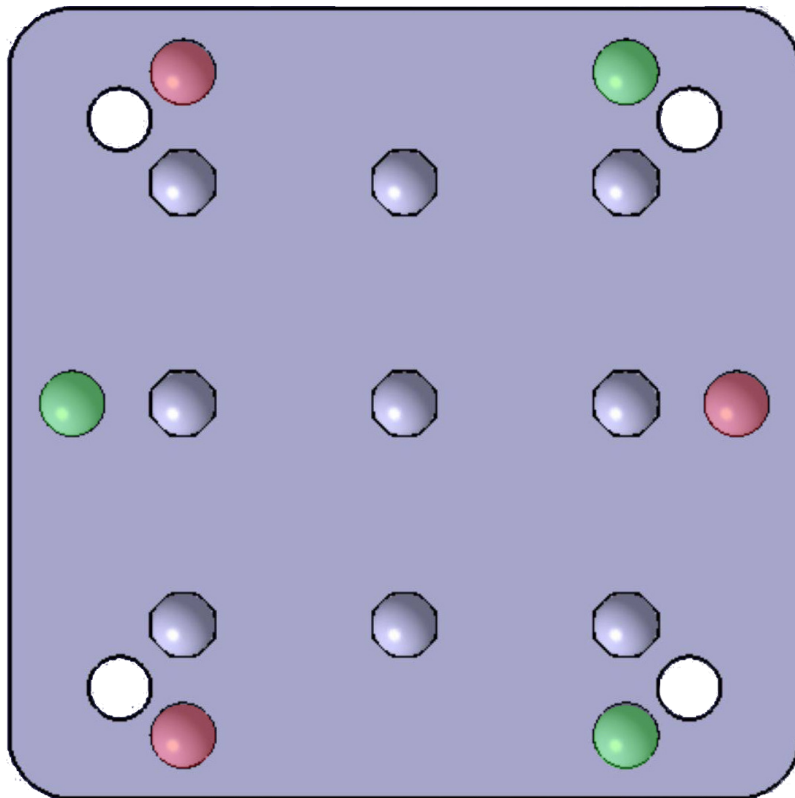


Figure 3.6: Top view of the revised build volume test artifact assembly.

3.2.2 Model stability

A model stability analysis was performed on the build volume test artifact using the 3-2-1 alignments intended for geometrical inspection. Different configurations of the alignments were used to find an alignment that gave an even sensitivity distribution. Figure 3.7 and 3.8 show two stability analyses done with two locating schemes. First configuration has an uneven distribution of the sensitivity while the second configuration has an even color distribution and also a lower peak sensitivity indicated by the color range. The red arrows indicate which direction has been locked on the reference spheres. The letters A, B and C next to the reference spheres indicate the locking combination.

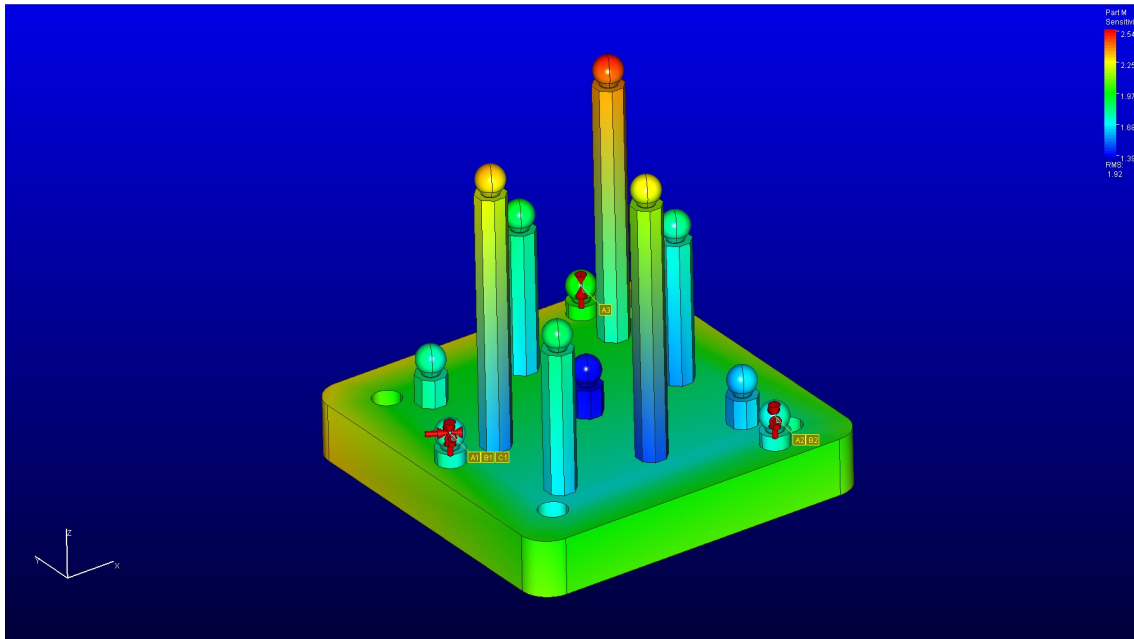


Figure 3.7: Stability analysis of the build volume test artifact with first locating scheme configuration.

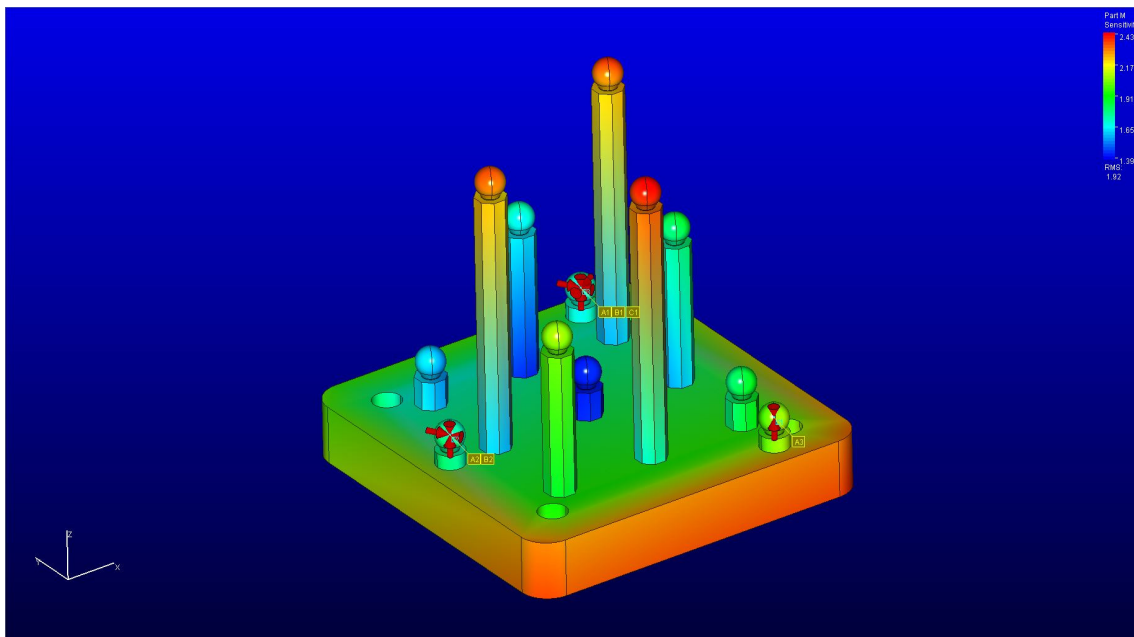


Figure 3.8: Stability analysis of the build volume test artifact with second locating scheme configuration.

The second locating scheme was planned to be used for the geometrical analysis but due to unforeseen problem with the reference spheres, the first locating scheme configuration had to be used.

3.3 AM machine settings and process parameters

The AM machine settings and process parameters used for the manufacturing of the test models are listed in table 3.1. The settings and parameters used are recommended by the machine operators.

Table 3.1: AM machine settings and process parameters.

Build name	316L-SLM	316L-EOS	410-SLM
Machine model	SLM 125 HL	EOS M290	SLM 125 HL
Material	316L	316L	410
Layer thickness	30 μm	20 μm	30 μm
Build plate material	316L	316L	H13
Laser power	200 W	-	200 W
No. of recycling	1	-	1
Powder size	20-53 μm	-	20-53 μm
Scan speed	800 mm/s	-	700 mm/s
Hatch distance	120 μm	-	120 μm

3.4 Measurement strategy

This subsection discusses the strategy for measuring the geometry and the surface roughness of the test artifacts.

3.4.1 3D scanner measurement strategy

Calibration is done prior to the measurement. Reference stickers are then adhered to the surface of the build in various locations for referencing and positioning. The build is then placed on the rotating table for scanning. Scanning camera is set at a certain measuring distance and measuring angle in order to cover the whole measurement volume. The measuring angle is highly depended on the model's shape but most builds are scanned using the angles 90°, 45° and 30°. The build in this thesis is scanned at 30° respective to the center point of the rotating table. Depending on the visibility of the build from different angles, the number of divisions in one rotation needs to be specified in the program ATOS Professional to ensure no hindering of the view. Temperature of the atmosphere at the 3D scanning station is recorded for referencing purpose. The scanning process has no problem performing under ambient light environment due to the use of 'Blue light technology' which filter out the extra reflecting light that is not the blue light emitted by the scanner. After the build has been scanned from all angles, ATOS Professional software stitches the data mesh into one file that will later need treatment such as removing of the miscalculated data points.

3.4.2 Surface area roughness measurement strategy

After 3D scanning, the samples are cut from the build using wire electrical discharging machine (EDM) and are inspected regarding the surface roughness with Sensofar S Neox machine which is placed on Accurion Halcyonics_i4 active vibration isolation platform. Aligning of the samples is done roughly by hand and the overview picture is taken with 5x magnification lens. The surface roughness data is obtained with 20x magnification lens through the means of confocal fusion mode which correlates the data from focus variation microscopy and confocal microscopy. The measurement area is 6.8 mm x 16.5 mm with the resolution of 0.64 $\mu\text{m}/\text{pixel}$. The measurement area is located roughly around the area shown in figure 3.9.

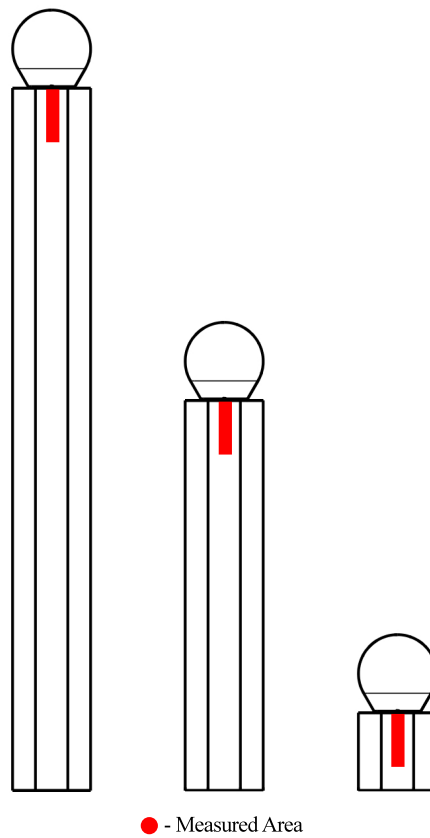


Figure 3.9: Measurement area specified by area marked in red.

The acquisition is done on four sides on all samples, namely x+, x-, y+ and y-, which are the side against the argon flow, along with the argon flow, along with scraper blade direction and against scraper blade direction, respectively.

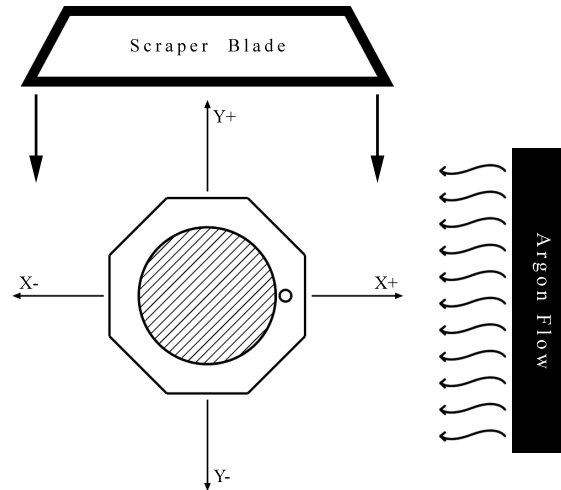


Figure 3.10: Nomenclature of sides name according to the sample orientation.

3.5 Inspection strategy

This subsection discusses the inspection strategy for the geometry and the surface roughness of the test artifacts.

3.5.1 Geometry inspection strategy

Fitting spheres are created from the spherical data points of each sphere, reference spheres and sample spheres, within the 3D scanned mesh file by best fitting method. The CAD file is then aligned to the 3D scanned mesh file with 3-2-1 alignment where the 6 degrees of freedom are locked in XYZ, YZ and Z directions at the reference spheres specified in figure 3.11. Deviation in the position of the center of the nominal sphere, from CAD file, and the fitting sphere, from 3D scanned mesh file, is then calculated.

Later on in the investigation, the effect of choosing the alignment system has become more essential for discussion therefore the following locating scheme is applied in addition to the one in figure 3.11 where X, Y and Z state the direction that has been locked at each sphere. Note that this alignment is still a 3-2-1 alignment.

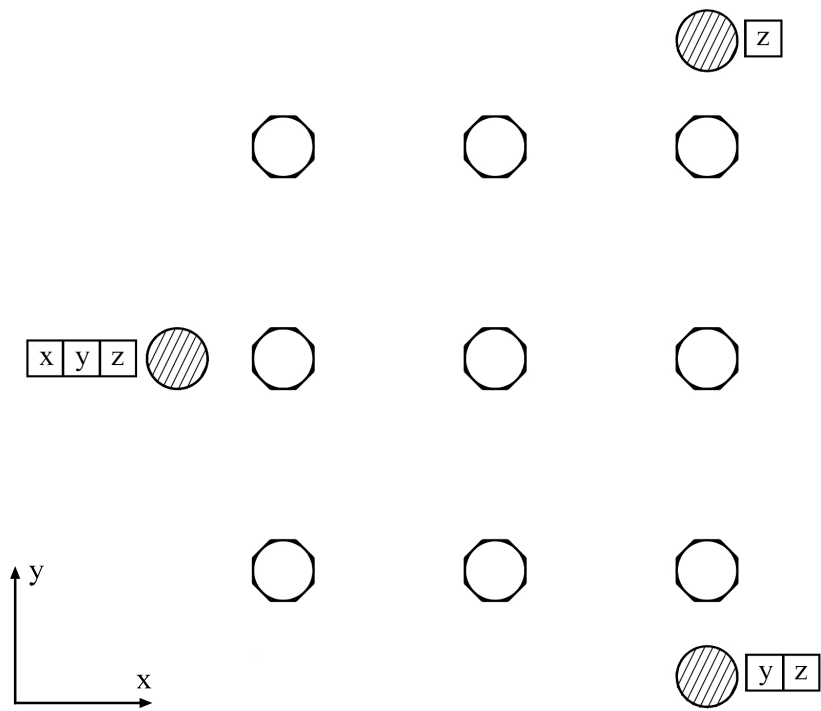


Figure 3.11: Locations of reference spheres (hatched) along with their locking axes.

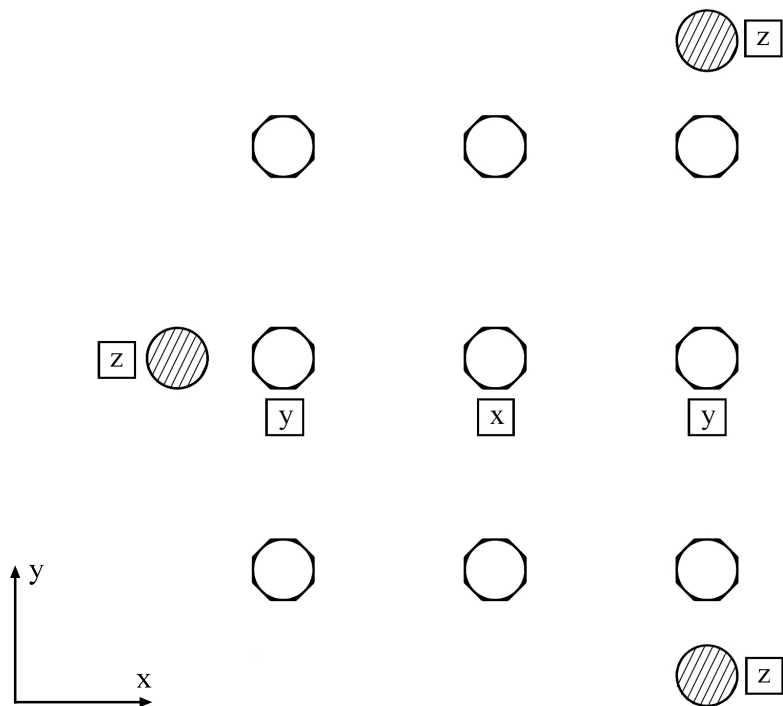


Figure 3.12: Alternative locating scheme.

For this thesis, locating schemes in figure 3.11 and 3.12 will be called "Alignment 1" and "Alignment 2", respectively.

3.5.2 Surface area roughness inspection strategy

The raw area roughness profile file must be processed before evaluating the areal roughness parameters to avoid introducing unwanted bias to the result. With the use of MountainsMap 7.4 software, first, the raw areal roughness profile is treated with form removal to flatten out the profile. The removed form is set to be a function of polynomial of degree of 2 because main form that exist on the sample is leveling. Then, the profile is treated with denoising spatial filter where the filter window size is set to be 3 by 3. Denoising filter will suppress any data point that acts as an outlying data point in that filter window size. Lastly, all the non-measured points are filled through a smooth shape algorithm to allow hybrid parameters, Sdr and Sdq, to be calculated.

3.6 Microstructure and chemical composition analysis strategy

This subsection contains the sample preparation method, microstructure analysis method and chemical composition analysis method.

3.6.1 Sample preparation

Only the 100 mm samples are prepared for microstructure and chemical composition analysis to lower the time consumption without losing significant sample data in the Z-direction. The cross section of interest is located 5 mm from the bottom of the model and 5 mm below the top of the octagon part. Figure 3.13 illustrates where the cross sections are located on the 100 mm sample and which side of the cross section is analyzed.

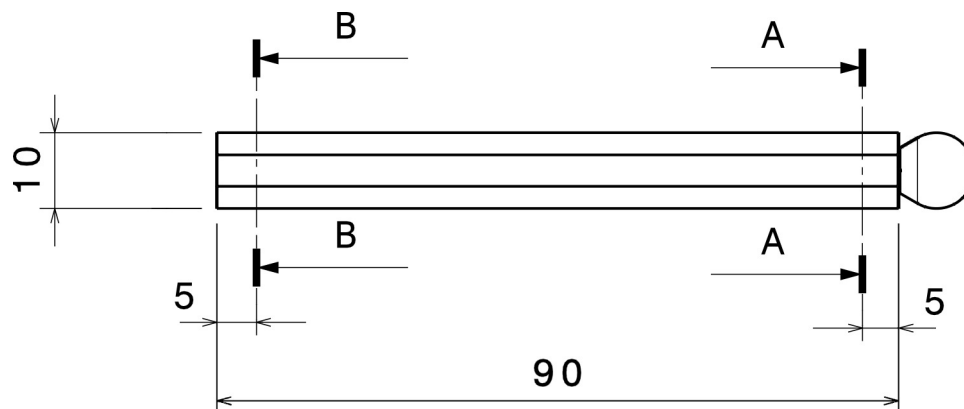


Figure 3.13: Locations of the cross sections of interest on the 100 mm sample.

One build has a total of six samples, three near the bottom and three near the top named as shown in figure 3.14. Each 100 mm model is cut into four pieces using the Struers Discotom-2 for easier mounting in the precision cutting machine Struers Accutom-5. The precision cut is done 2-3 mm from the cross section of interest to

3. Methods

leave enough material for the grinding and polishing process. With the samples cut, they are mounted in a PolyFast resin from Struers for the examination in a SEM. The mounting temperature is 180°C, the pressure is 250 bar and the total time including cooling is 6 minutes. The mounting equipment is a Struers CitoPress-5 with a 40 mm cylinder size. The six samples fit in two mountings but one extra dummy mounting is created for better balance during the grinding and polishing process. Grinding and polishing is done in the Struers Abramin machine . Each step is detailed in table 3.2 with abrasive type, rotational speed, force and time used. The samples are inspected by eye after each step to check if all the unwanted scratches on the surface have been removed. Each step is repeated if it does not pass the visual inspection.

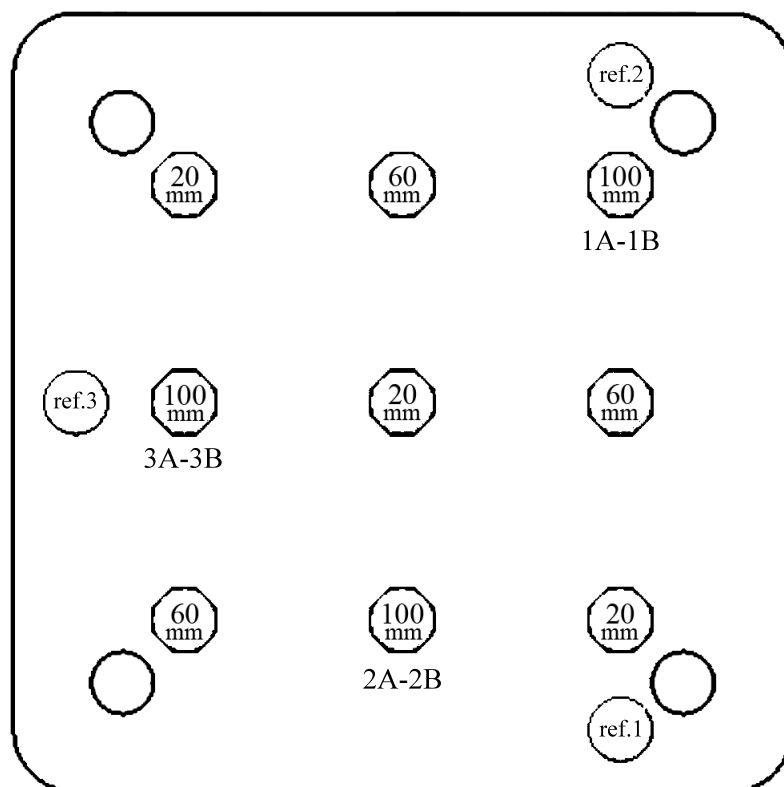


Figure 3.14: Nomenclature of the 100 mm samples.

Table 3.2: Summary of all the grinding and polishing steps.

Abrasive type	Rotational speed [rpm]	Force [N]	Time [min:s]
#320 SiC	300	100	1:30
#320 SiC	300	100	1:30
#1000 SiC	300	100	1:30
#1000 SiC	300	100	1:30
Largo $9\mu m$	150	110	7:30
Largo $9\mu m$	150	110	3:00
Dac $3\mu m$	150	90	7:30
OP-S, $0.04\mu m$	150	50	3:30
OP-S, $0.04\mu m$	150	50	2:00

OP-S is a chemical and abrasive polishing step that produces a surface free of scratches and deformation. It is an active reagent so it is best done a few days before inspecting with SEM. After polishing, the samples are cleaned using ethanol in a ultrasonic cleaner and dried out. The samples are stored in protective covers to protect the surface.

3.6.2 Microstructure and chemical composition analysis

The SEM used is a JEOL JSM-6610-LV using accelerating voltage of 15kV, working distance of 10 mm and high vacuum at ~ 0.1 mPa. The center of each sample is inspected at 50x and 500x magnification. SE and BSE images are taken at both magnifications along with an EDS spectrum at 50x. Elemental mapping is performed at 500x magnification on two samples that are furthest apart from each other on the build plate, illustrated in figure 3.14. The duration is 1 hour for each mapping. If the material is homogeneous and no defects are detected, then elemental mapping is not necessary for the rest of the samples.

4

Results

This chapter covers the results from the geometrical analysis with the 3-D scanner, the surface area roughness measurements and the microstructural and chemical analysis.

4.1 Geometrical analysis

Geometrical analysis and its result are presented in this section. It includes discussion over acquisition of the geometry, geometrical accuracy analysis and discussion over locating scheme and corresponding reference spheres.

4.1.1 Acquisition of geometry

Due to the complexity and some limitations in the acquisition algorithm of a 3D scanned mesh file, the 3D scanned mesh file is not always perfect. The method itself does not have an expected number of points per measured surface area to verify whether the scanning has been done satisfyingly. One of the cases that induce the occurrence of missing data points is when the surface is shiny. As observable in figure 4.1, the missing data points are shown on the flat surface (highlighted in red).

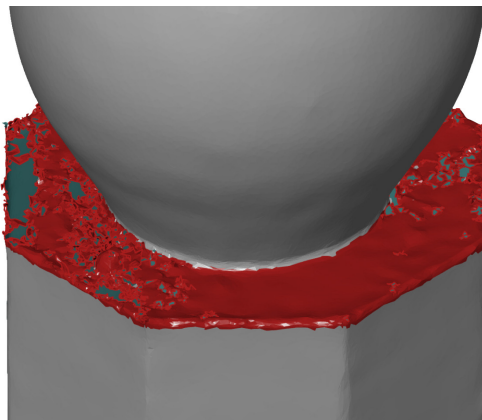


Figure 4.1: Shiny surface leads to missing data points.

Shadowing can also lead to problems regarding the missing data points but it can simply be fixed by varying the camera angle, re-designing the sample and having more divisions in one rotation during the scanning process. In addition to the issue with the missing data points, outlying data can be introduced to the 3D scanned

mesh when the stitching algorithm fails to stitch the scanned data point to its corresponding surface at the correct length, resulting in floating and outlying data points and potentially missing data.

The repeatability of the 3D scanning process itself is also another question that needs to be answered to ensure that the 3D scanned result is reliable. The 316L build by EOS M290 has been scanned twice and the 3D scanned file are compared to each other as shown in figure 4.2. The difference between the two scans mainly lies between $-15\mu\text{m}$ and $15\mu\text{m}$. Therefore, this range of difference is acceptable, because it is lower than layer thickness.

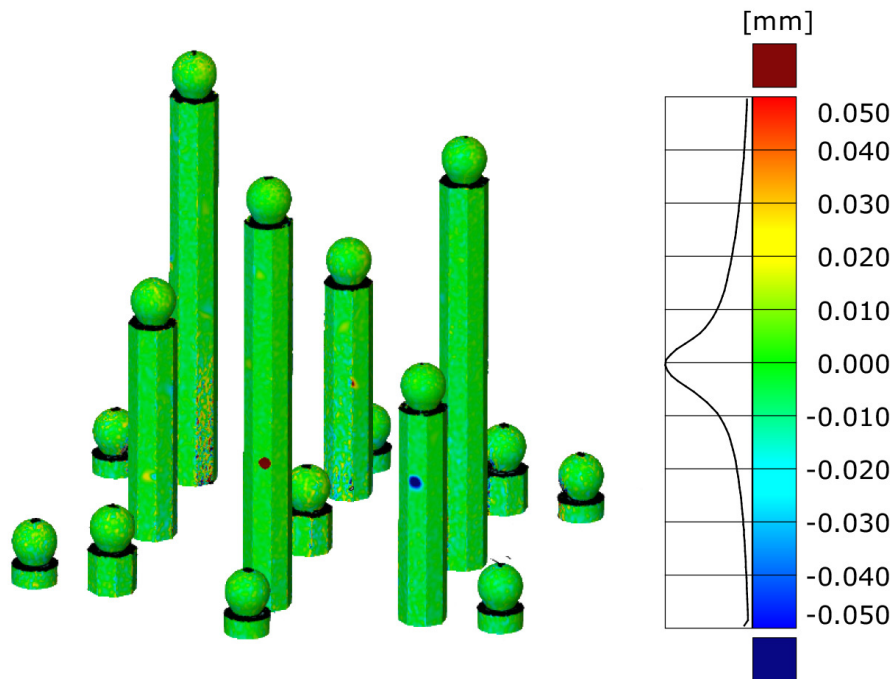


Figure 4.2: Surface comparison between two different scans of 316L-EOS.

4.1.2 X-, Y-, Z-direction and sphere diameter accuracy

X-, Y-, Z-direction and sphere diameter accuracy, along with their machine capability as obtained through alignment 1 (figure 3.11) and alignment 2 (figure 3.12) will be exhibited.

4.1.2.1 Alignment 1

With alignment 1, deviations of the center point position between the actual print and the CAD in X-, Y- and Z-direction and deviation of the printed sphere size as compared to nominal value of 10 mm are shown as an average ,along with their respective standard deviation in table 4.1.

Table 4.1: Average deviation in X- and Y- direction and their standard deviation for 316L-SLM, 316L-EOS and 410-SLM under alignment 1.

	dX [mm]	dY [mm]	dZ [mm]	dD [mm]
316L-SLM	0.128	-0.005	-0.037	-0.113
Standard dev.	0.162	0.139	0.029	0.041
316L-EOS	-0.229	-0.096	-0.069	0.038
Standard dev.	0.123	0.110	0.063	0.004
410-SLM	0.268	0.051	0.009	-0.059
Standard dev.	0.113	0.103	0.012	0.007

How samples from each build had deviated from their nominal X-,Y-position is shown in figure 4.3, 4.4 and 4.5. Note that the arrows are not to scale.

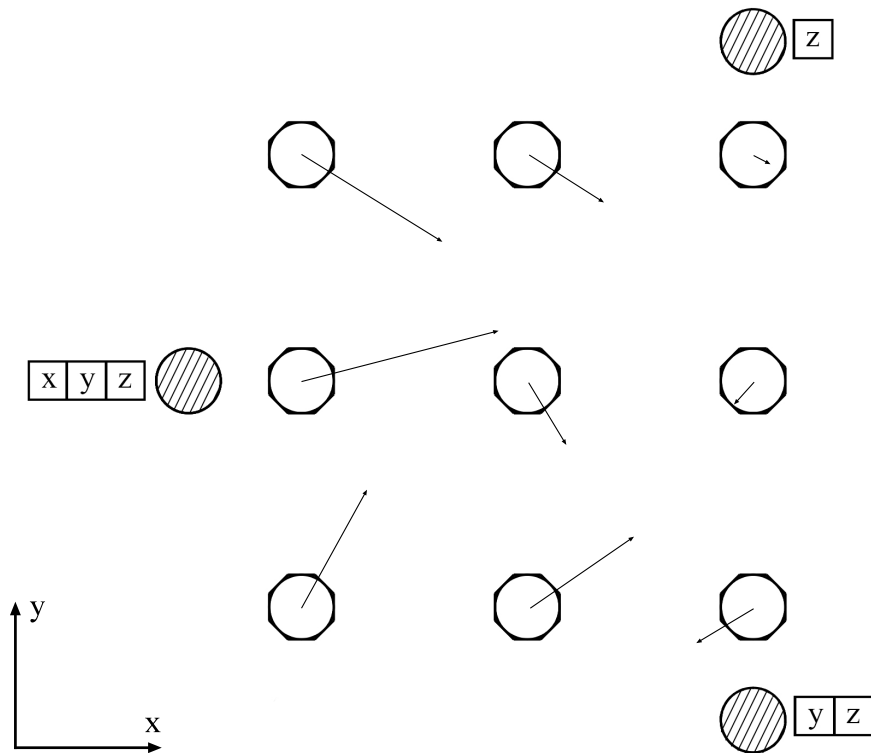


Figure 4.3: Deviation of each sample on 316L-SLM build under alignment 1.

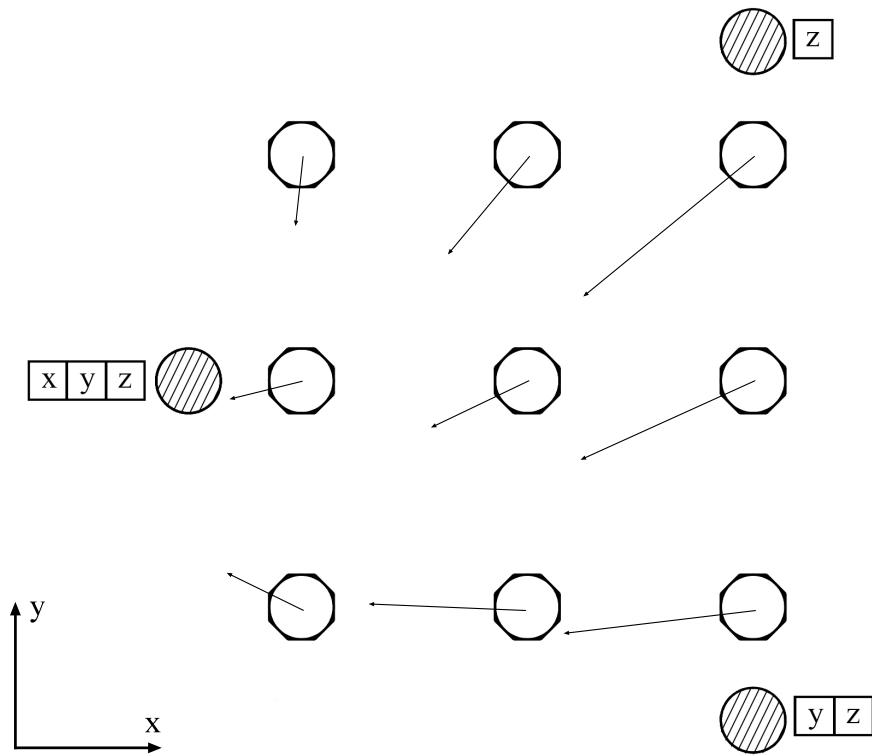


Figure 4.4: Deviation of each sample on 316L-EOS build under alignment 1.

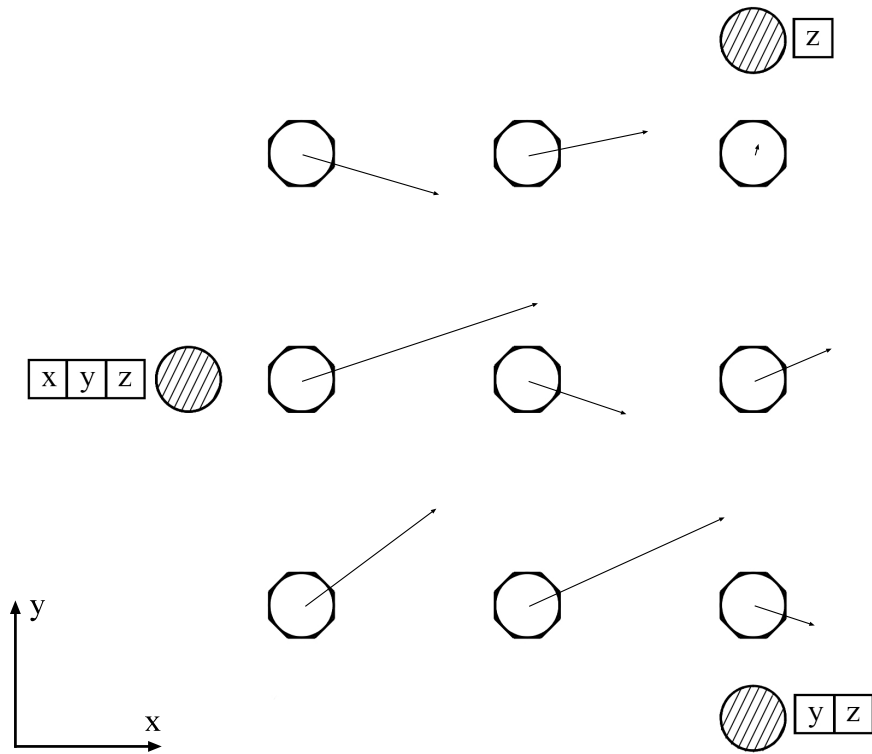


Figure 4.5: Deviation of each sample on 410-SLM build under alignment 1.

The tolerance limits for the deviation in X-, Y- and Z-direction along with the deviation in diameter are shown in table 4.2 or as depicted in figure 4.6, 4.7 and 4.8.

Table 4.2: Tolerance limits for the deviation in geometrical accuracy and sphere diameter under alignment 1: 316L-SLM, 316L-EOS and 410-SLM.

	dX [μm] $T_L - T_U$	dY [μm] $T_L - T_U$	dZ [μm] $T_L - T_U$	dD [μm] $T_L - T_U$
316L-SLM	-356 - 612	-420 - 410	-124 - 50	-236 - 10
316L-EOS	-597 - 139	-425 - 233	-257 - 119	26 - 50
410-SLM	-70 - 606	-257 - 359	-27 - 45	-80 - -38

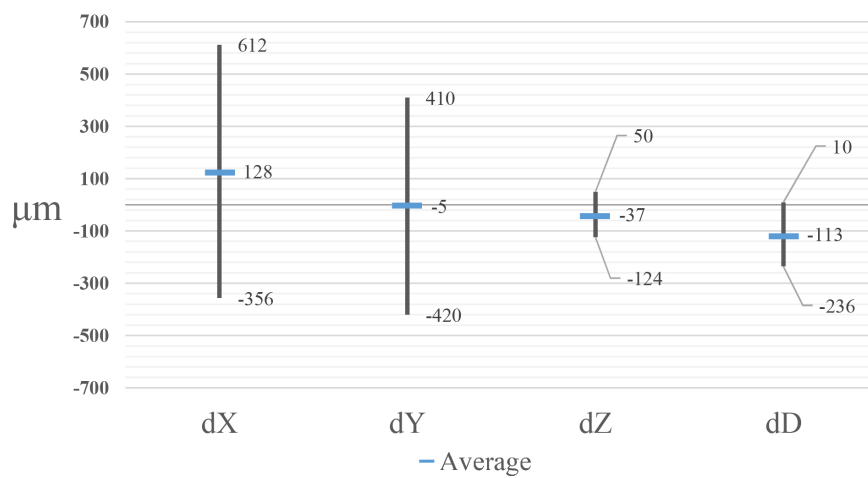


Figure 4.6: Tolerance limits for the deviation in geometrical accuracy and sphere diameter of 316L-SLM under alignment 1.

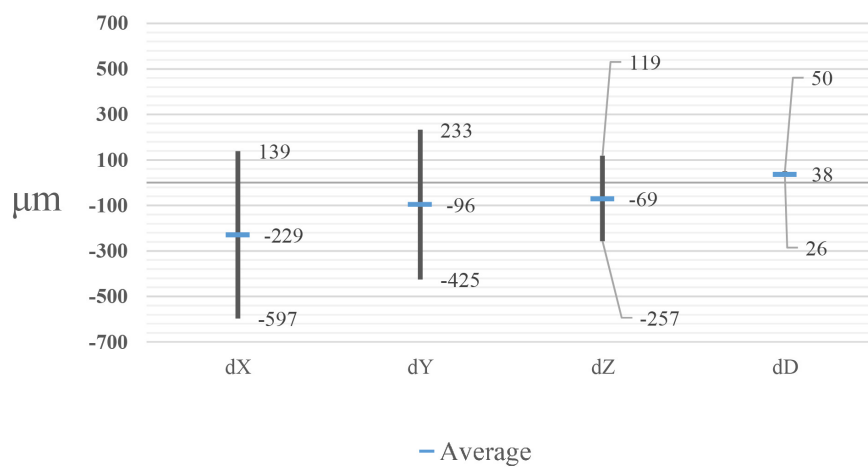


Figure 4.7: Tolerance limits for the deviation in geometrical accuracy and sphere diameter of 316L-EOS under alignment 1.

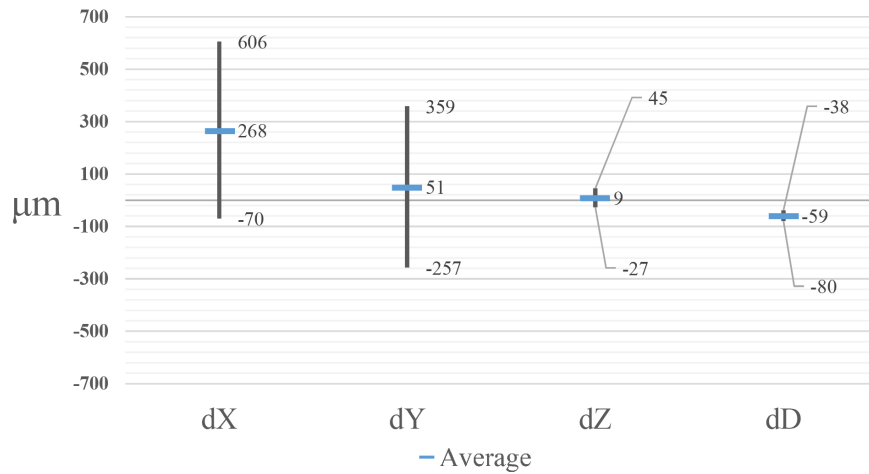


Figure 4.8: Tolerance limits for the deviation in geometrical accuracy and sphere diameter of 410-SLM under alignment 1.

4.1.2.2 Alignment 2

The effect of alignment system is investigated by using the alignment in figure 3.12. In the same manner as alignment 1 in section 4.1.2.1, the results of alignment 2 are exhibited below.

Table 4.3: Average deviation in X- and Y- direction and their standard deviation for 316L-SLM, 316L-EOS and 410-SLM under alignment 2.

	dX [mm]	dY [mm]	dZ [mm]	dD [mm]
316L-SLM	0.063	-0.039	-0.036	-0.114
Standard dev.	0.149	0.133	0.029	0.038
316L-EOS	-0.032	0.002	-0.069	0.038
Standard dev.	0.114	0.095	0.063	0.004
410-SLM	0.076	-0.058	0.009	-0.059
Standard dev.	0.115	0.098	0.012	0.007

How samples from each build had deviated from their nominal X-,Y-position is shown in figure 4.9, 4.10 and 4.11. Note that the arrows are not to scale.

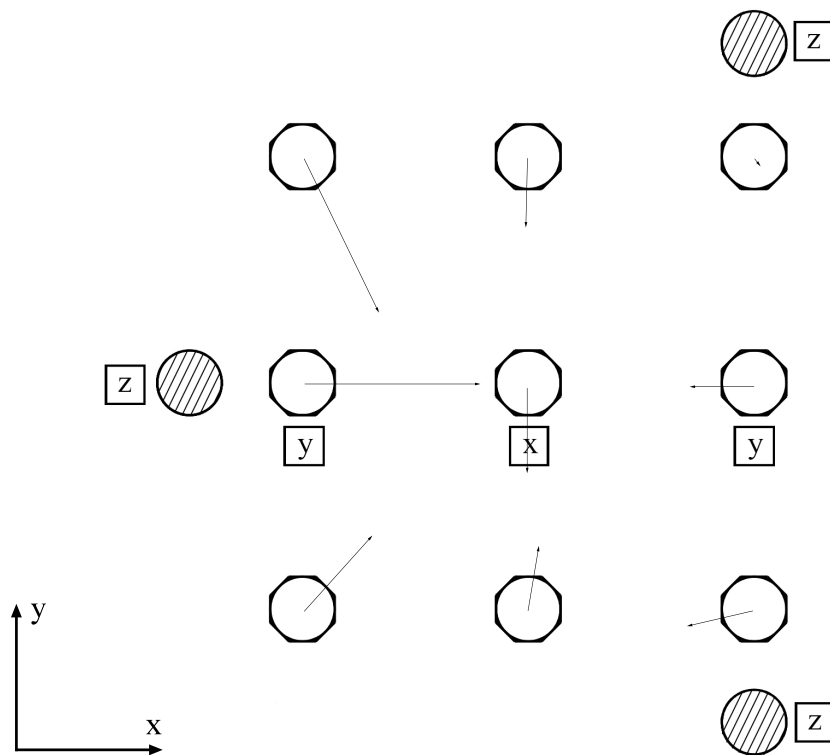


Figure 4.9: Deviation of each sample on 316L-SLM build under alignment 2.

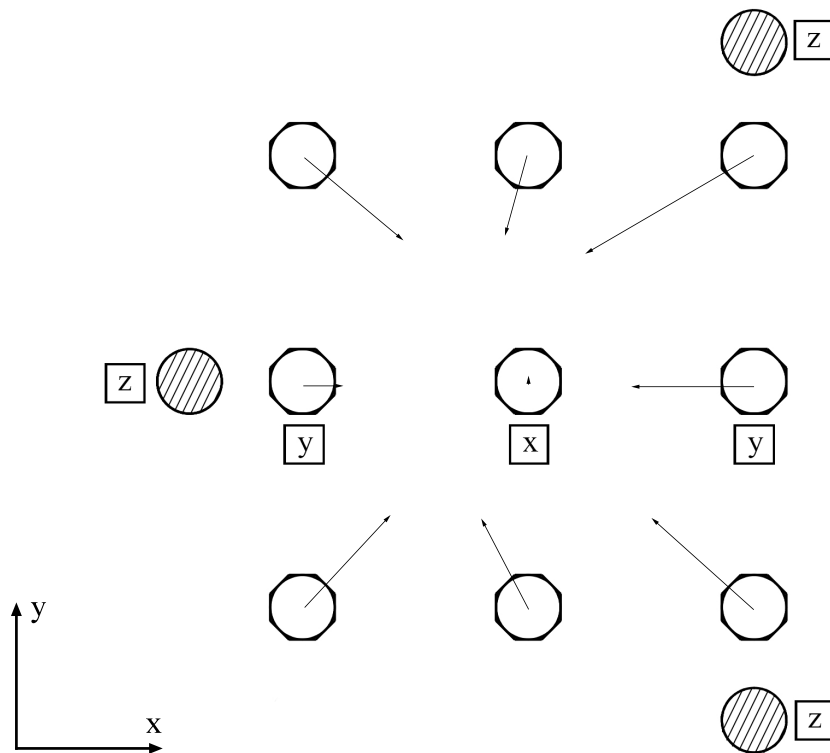


Figure 4.10: Deviation of each sample on 316L-EOS build under alignment 2.

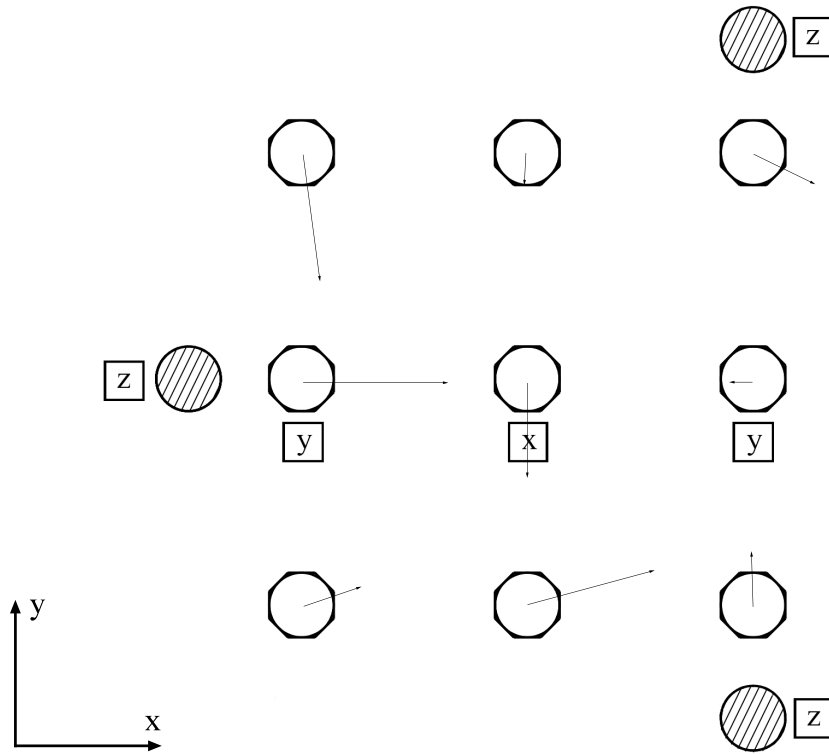


Figure 4.11: Deviation of each sample on 410-SLM build under alignment 2.

The tolerance limits for the deviation in X-, Y- and Z-direction along with the deviation in diameter are shown in table 4.4 or as depicted in figure 4.12, 4.13 and 4.14.

Table 4.4: Tolerance limits for the deviation in geometrical accuracy and sphere diameter under alignment 2: 316L-SLM, 316L-EOS and 410-SLM.

	dX [μm] $T_L - T_U$	dY [μm] $T_L - T_U$	dZ [μm] $T_L - T_U$	dD [μm] $T_L - T_U$
316L-SLM	-382 - 508	-437 - 359	-123 - 51	-228 - 0
316L-EOS	-373 - 309	-282 - 286	-257 - 119	26 - 50
410-SLM	-268 - 420	-351 - 235	-27 - 45	-80 - -38

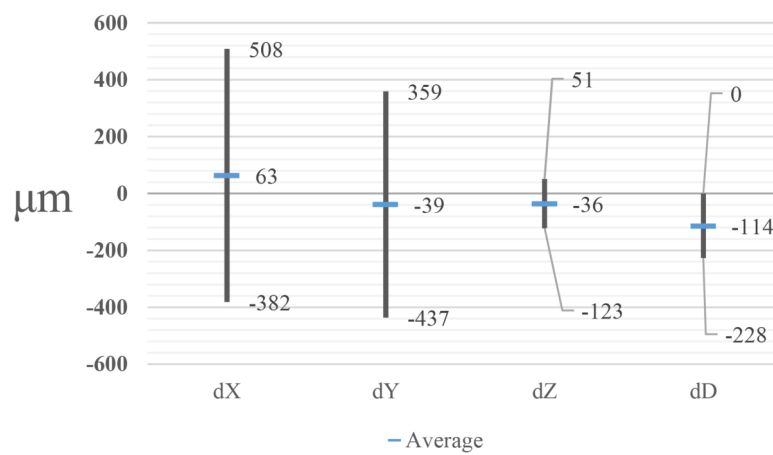


Figure 4.12: Tolerance limits for the deviation in geometrical accuracy and sphere diameter of 316L-SLM under alignment 2.

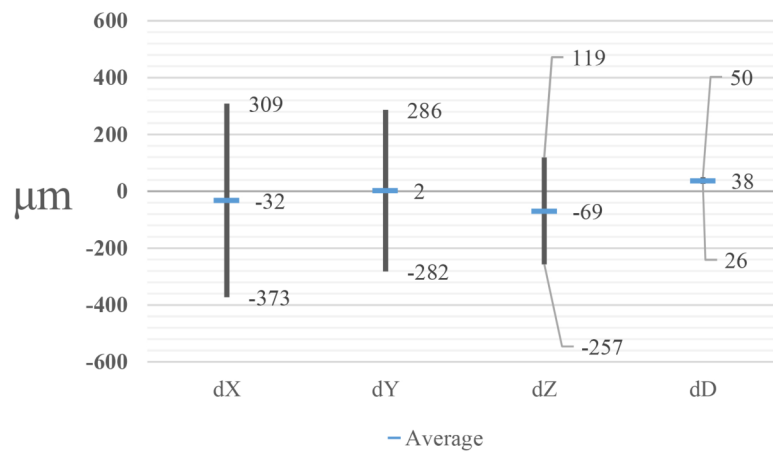


Figure 4.13: Tolerance limits for the deviation in geometrical accuracy and sphere diameter of 316L-EOS under alignment 2.

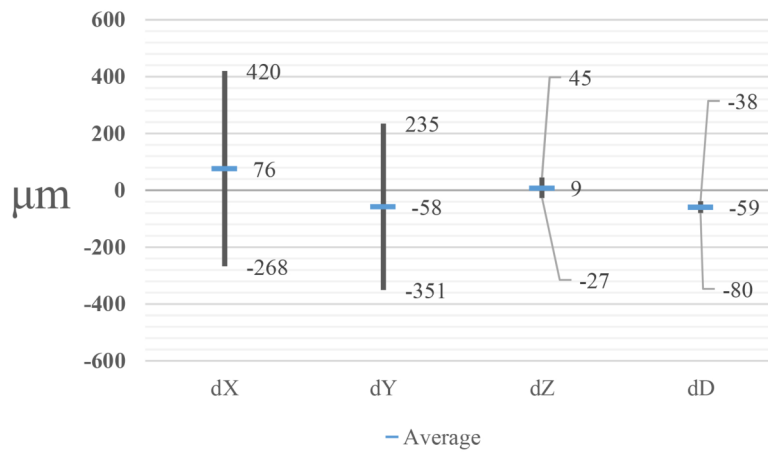


Figure 4.14: Tolerance limits for the deviation in geometrical accuracy and sphere diameter of 410-SLM under alignment 2.

4.1.3 Reference spheres and locating scheme

With 3-2-1 alignment that has locking directions as depicted in figure 3.11, deviations in the location of the reference spheres themselves should also be concerned as well. Table 4.5 shows the deviations in X-, Y- and Z-direction of the reference sphere denoted by their locking directions.

Table 4.5: Deviation in X-, Y- and Z-direction of the reference spheres in 316L-SLM, 316L-EOS and 410-SLM.

Build	Lock dir.	dX [mm]	dY [mm]	dZ [mm]
316L-SLM	XYZ	0	0	0
	YZ	-0.419	0	0
	Z	-0.220	-0.390	0
316L-EOS	XYZ	0	0	0
	YZ	-0.402	0	0
	Z	-0.236	-0.324	0
410-SLM	XYZ	0	0	0
	YZ	-0.167	0	0
	Z	-0.091	-0.154	0

4.2 Surface area roughness analysis

The result from the surface area roughness analysis is presented in this section. It includes surface area parameters, tolerance limits and anomalies.

4.2.1 Acquisition of surface area roughness

The average non-measured points (NMP) ratio for each surface roughness acquisition is shown in table 4.6. The values are calculated using 36 measurements per build. The missing points are mostly located at steep angles on the surface which cannot be detected by the optical microscope. Measurements of model 20 mm s2 x– from the builds 316L-SLM and 410-SLM are excluded from the overall parameters, comparison between different orientations and height. It is because they showed anomalies on the surface that skews the parameter values. Those measurements are treated and presented separately in the subsection "*Surface area roughness anomalies*".

Table 4.6: Non-measured points ratio and its standard deviation for the builds: 316L-SLM, 316L-EOS and 410-SLM.

Build	NMP [%]	Standard dev. [%]
316L-SLM	0.59	0.24
316L-EOS	0.76	0.22
410-SLM	0.99	0.41

Sample 20 mm s1 y– from the 316L-SLM build is shown in figure 4.15 as an example of a surface acquired by the optical microscope. The image is a height map of the surface with a colour range legend on the right side. The surface is isotropic with many peaks present as red and yellow dots on the surface, which likely come from the partly melted particles adhering to the surface.

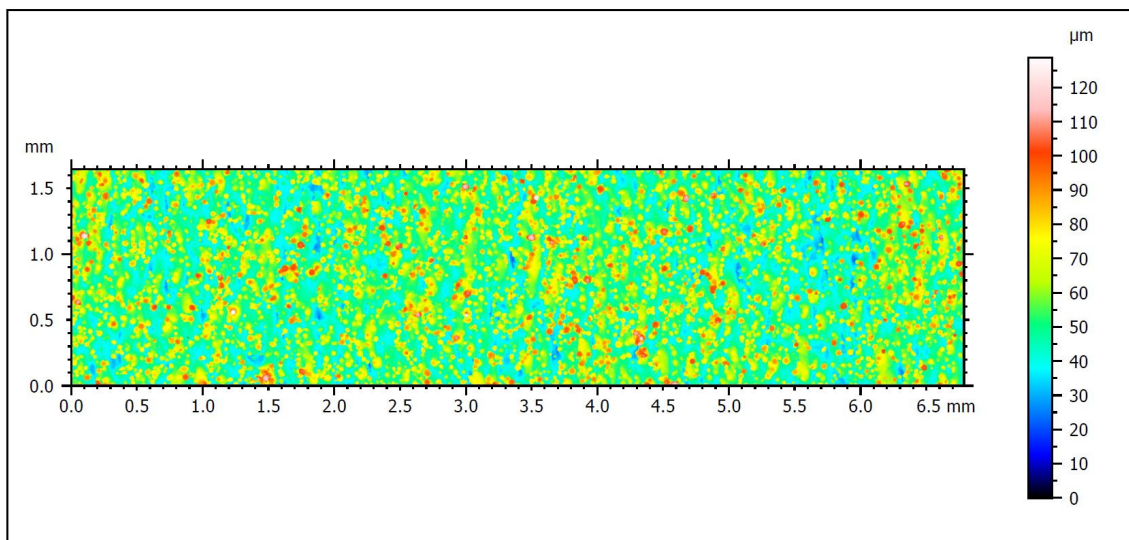


Figure 4.15: Surface texture of sample 20 mm s1 y– from 316L-SLM.

4.2.2 Overall height, spatial and hybrid parameter

The overall height, spatial and hybrid parameters for the three builds are presented in table 4.7. Each parameter value is averaged from 35 measurements except for

4. Results

316L-EOS with 36 measurements. The parameters presented are Sa (Arithmetical mean height), Sq (Root mean square height), Sdr (Developed interfacial area ratio), Sdq (Root mean square gradient), Ssk (Skewness), Sku (Kurtosis) and Str (Texture aspect ratio). The standard deviation for each parameter is under its corresponding parameter.

Table 4.7: Average height, spatial and hybrid parameters with corresponding standard deviation for the builds: 316L-SLM, 316L-EOS and 410-SLM.

	Sa [μm]	Sq [μm]	Sdr [-]	Sdq [-]	Ssk [-]	Sku [-]	Str [-]
316L-SLM	11.7	14.4	103	5.4	0.85	3.2	0.78
Standard dev.	1.01	1.05	9.99	0.4	0.16	0.5	0.04
316L-EOS	17.0	21.3	174	7.5	0.81	3.9	0.90
Standard dev.	0.85	1.10	14.3	0.4	0.14	0.6	0.03
410-SLM	12.3	14.8	119	6.1	0.73	2.9	0.81
Standard dev.	0.87	0.88	12.8	0.5	0.11	0.3	0.04

Tolerance limits for the height, spatial and hybrid parameters are calculated with a 3σ probability and the distribution is assumed to be normal. The values are presented in table 4.8 and 4.9.

Table 4.8: Tolerance limits for the height parameters for the builds: 316L-SLM, 316L-EOS and 410-SLM.

	Sa [μm] $T_L - T_U$	Sq [μm] $T_L - T_U$	Ssk [-] $T_L - T_U$	Sku [-] $T_L - T_U$
316L-SLM	8.7 - 14.7	11.2 - 17.5	0.38 - 1.32	1.8 - 4.7
316L-EOS	14.5 - 19.6	18.0 - 24.6	0.38 - 1.24	2.1 - 5.8
410-SLM	9.7 - 14.9	12.1 - 17.4	0.40 - 1.07	1.9 - 3.8

Table 4.9: Tolerance limits for the spatial and hybrid parameters for the builds: 316L-SLM, 316L-EOS and 410-SLM.

	Sdr [-] $T_L - T_U$	Sdq [-] $T_L - T_U$	Str [-] $T_L - T_U$
316L-SLM	73 - 133	4.1 - 6.7	0.66 - 0.91
316L-EOS	132 - 217	6.2 - 8.8	0.80 - 1.00
410-SLM	80 - 157	4.5 - 7.6	0.69 - 0.93

The overall parameter values and the tolerance limits are illustrated in figure 4.16 and 4.17. The blue line is the average parameter value and the dark grey vertical line is the tolerance limit range. The values are located next to each parameter in the chart. Sa and Sq values are higher for the 316L-EOS build compared with the builds by the SLM machine but the tolerance range is similar.

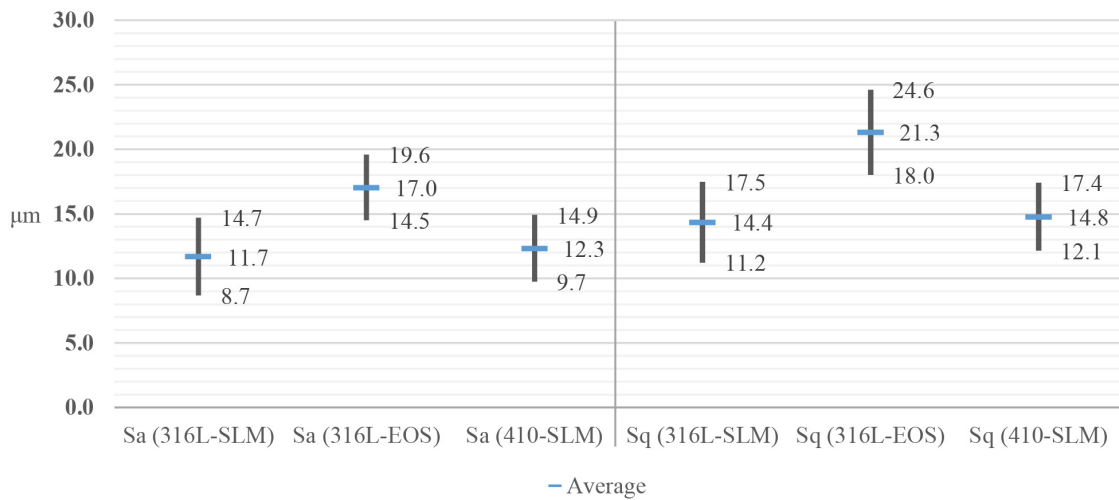
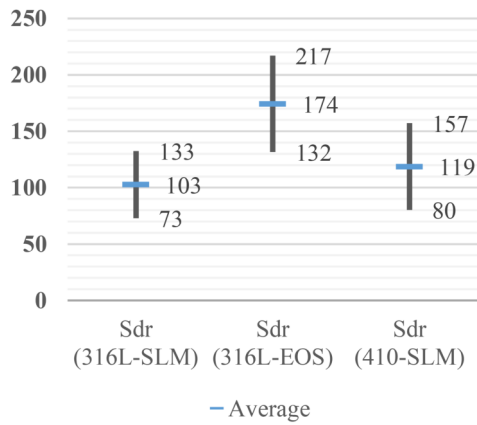


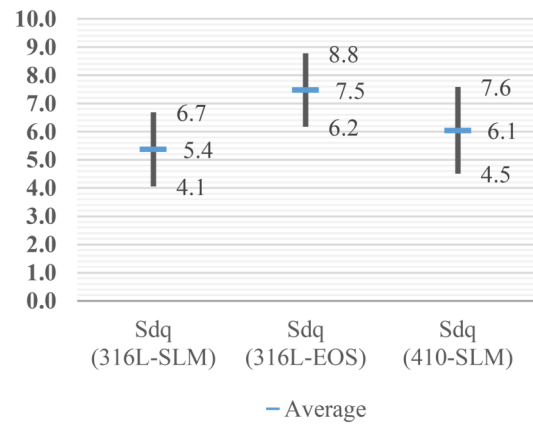
Figure 4.16: Diagram of Sa and Sq for 316L-SLM, 316L-EOS and 410-SLM.

The Sdr and Sdq values for 316L-EOS are higher than the builds by the SLM machine while Ssk and Sku have no significant difference between the builds as they are quite sensitive to outliers. The three builds have over double the surface area contributed by the texture, compared to a flat surface. Sdr is a useful value for adhesion applications and Sdq correlates with adhesive bond strength. Ssk correlates with the load carrying ability of a surface. For bearing applications a negative Ssk value is desired. A positive Ssk value indicates the presence of many peaks. The Sku value measures height distribution and the spikiness of the peaks. The Str values indicates that the surfaces for all builds are isotropic thus it is not shown as a diagram.

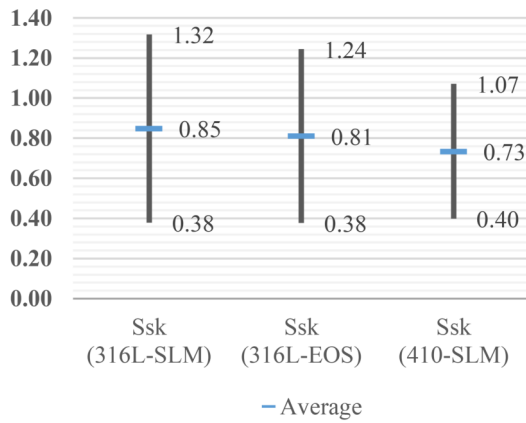
4. Results



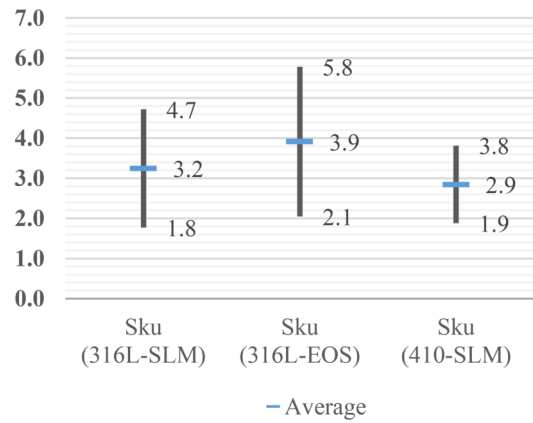
(a) Diagram of Sdr values.



(b) Diagram of Sdq values.



(c) Diagram of Ssk values.



(d) Diagram of Sku values.

Figure 4.17: Diagrams of Sdr, Sdq, Ssk and Sku for 316L-SLM, 316L-EOS and 410-SLM.

4.2.3 Surface roughness parameters at different heights

Height, spatial and hybrid parameters for measurements performed on models with the same height is shown in table 4.10, 4.11 and 4.12 for the three builds. The heights are 10 mm, 50 mm and 90 mm. The values are averaged out from 12 measurements per height except the 10 mm height for 316L-SLM and 410-SLM that uses 11 measurements.

Table 4.10: Height, spatial and hybrid parameters for the 316L-SLM build at different heights.

Height	Sa [μm]	Sq [μm]	Sdr [-]	Sdq [-]	Ssk [-]	Sku [-]	Str [-]
10 mm	10.6	13.3	93	4.9	0.99	3.6	0.77
50 mm	12.4	15.1	112	5.8	0.80	3.2	0.79
90 mm	12.0	14.6	103	5.4	0.77	3.0	0.79

Table 4.11: Height, spatial and hybrid parameters for the 316L-EOS build at different heights.

Height	Sa [μm]	Sq [μm]	Sdr [-]	Sdq [-]	Ssk [-]	Sku [-]	Str [-]
10 mm	17.1	21.4	175	7.5	0.89	4.1	0.90
50 mm	17.0	21.3	178	7.6	0.75	3.9	0.90
90 mm	17.0	21.2	170	7.3	0.79	3.8	0.89

Table 4.12: Height, spatial and hybrid parameters for the 410-SLM build at different heights.

Height	Sa [μm]	Sq [μm]	Sdr [-]	Sdq [-]	Ssk [-]	Sku [-]	Str [-]
10 mm	11.7	14.1	112	5.8	0.80	3.0	0.80
50 mm	13.2	15.6	128	6.5	0.66	2.7	0.83
90 mm	12.1	14.6	115	5.8	0.75	2.9	0.80

4.2.4 Surface roughness parameters at same orientation

Height, spatial and hybrid parameters for measurements performed on models facing the same orientation is shown in table 4.13, 4.14 and 4.15 for the three builds. The orientations are x+, x-, y+ and y-. The values are averaged out from 9 measurements per orientation. x- orientation values for 316L-SLM and 410-SLM uses only 8 measurements.

Table 4.13: Height, spatial and hybrid parameters for the 316L-SLM build for different orientations

Orientation	Sa [μm]	Sq [μm]	Sdr [-]	Sdq [-]	Ssk [-]	Sku [-]	Str [-]
x+	12.0	14.7	103	5.4	0.76	3.0	0.78
x-	11.4	14.1	102	5.3	0.95	3.6	0.79
y+	11.5	14.1	105	5.4	0.85	3.2	0.80
y-	11.8	14.5	101	5.3	0.84	3.2	0.77

Table 4.14: Height, spatial and hybrid parameters for the 316L-EOS build for different orientations.

Orientation	Sa [μm]	Sq [μm]	Sdr [-]	Sdq [-]	Ssk [-]	Sku [-]	Str [-]
x+	17.4	21.7	170	7.5	0.83	3.9	0.88
x-	17.4	21.6	184	7.8	0.74	3.6	0.88
y+	16.8	21.4	168	7.2	0.99	4.8	0.90
y-	16.7	20.6	176	7.4	0.69	3.3	0.91

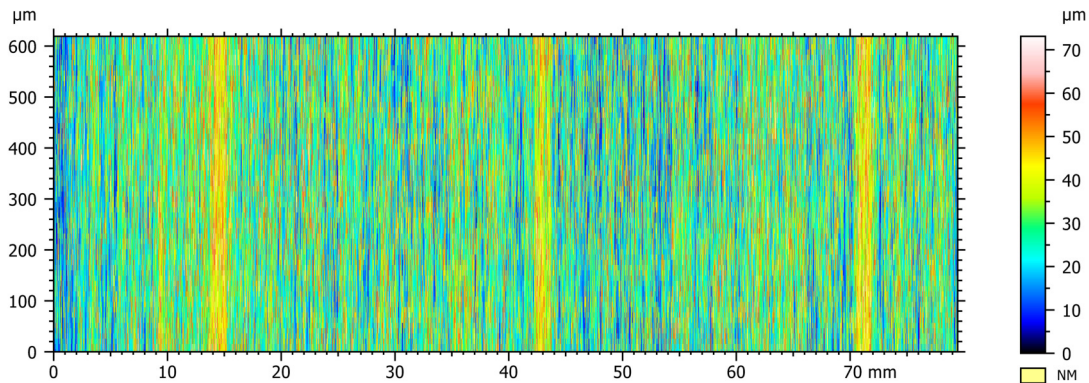
Table 4.15: Height, spatial and hybrid parameters for the 410-SLM build for different orientations.

Orientation	Sa [μm]	Sq [μm]	Sdr [-]	Sdq [-]	Ssk [-]	Sku [-]	Str [-]
x+	12.4	14.8	119	6.1	0.69	2.7	0.83
x-	12.0	14.4	114	5.9	0.80	2.9	0.83
y+	12.3	14.7	121	6.1	0.73	2.8	0.81
y-	12.6	15.1	121	6.1	0.73	3.0	0.78

The surface area roughness parameters do not deviate significantly with different orientations for each build.

4.2.5 Surface area roughness anomalies

Two anomalies were detected in the measurement results. The first one is form error on the 316L-SLM build that are located at the same heights for the entire build. The errors appears as hills and valleys with the form of bands only on the surfaces with the orientations x+ and x-. The bands are approximately 1 mm in height and cover the whole width of the model. Figure 4.18 shows the overview of the surface from 100 mm s1 x+. The form error can be identified as the three red bands at the position 19 mm, 47 mm and 75 mm.

**Figure 4.18:** Overview of the 100 mm s1 x+ surface from the 316L-SLM build.

The bands were measured and parameters calculated with and without long wavelength form removal. Only the second band of the 100 mm s1 x+ sample is here as other bands showed similar results. The images for the second band before and after the form removal are shown in figure 4.19, the form removed is also included. The band is located roughly between 2.5 mm and 4.1 mm. With the form removal, the surface looks similar to other surfaces on the 316L-SLM build.

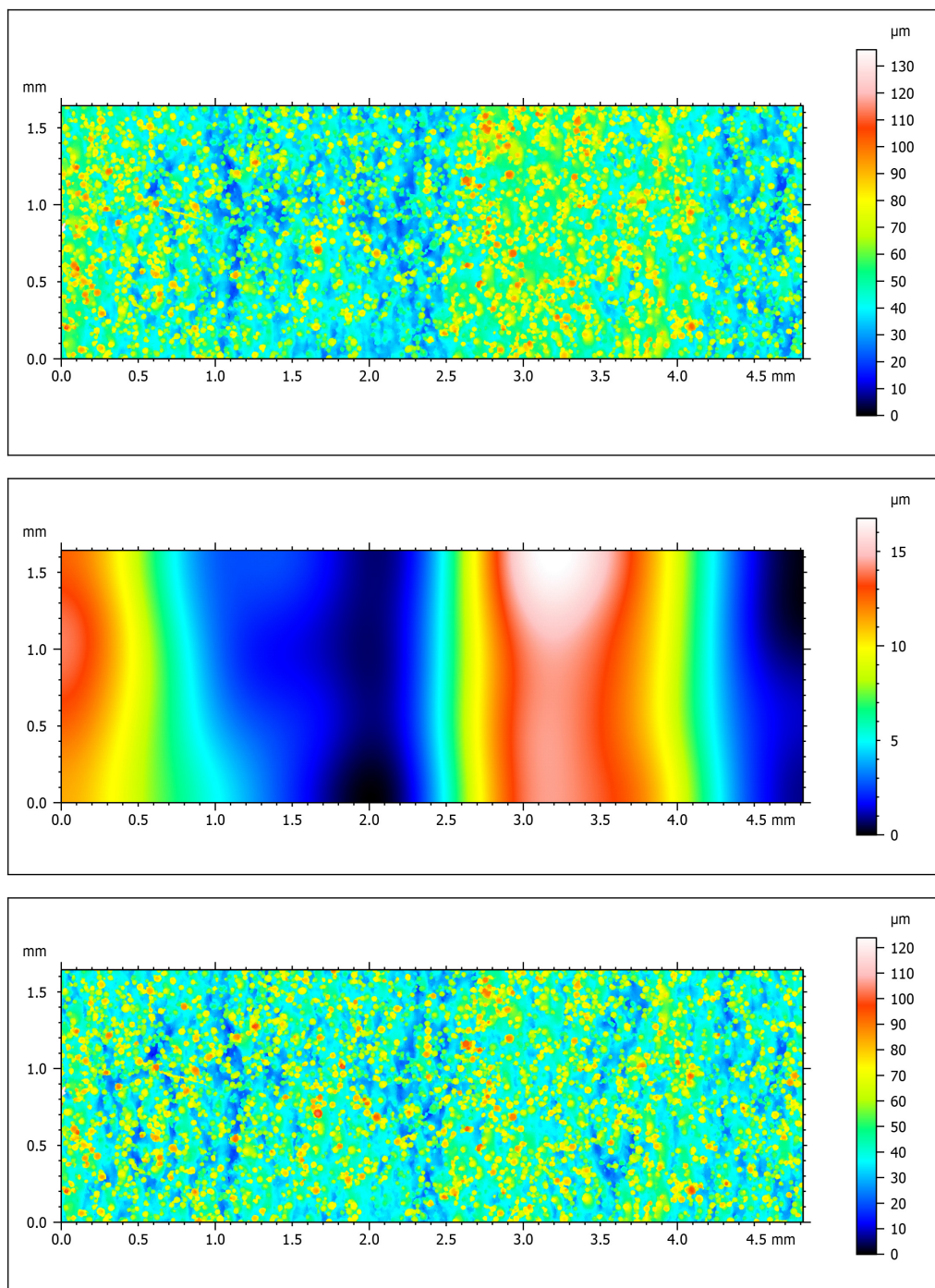


Figure 4.19: Surface area roughness image of 100 mm s1 x+ band 2 from the 316L-SLM build. Top image is before form removal, middle image is form removed and bottom image is after form removal.

Table 4.16 shows the surface area roughness parameters before and after the form removal. S_a and S_q decrease after the form removal as expected. S_{dr} and S_{dq} stay the same but S_{tr} increases twofold after the form removal. The surface texture goes from an anisotropic to an isotropic surface, similar to other measurements on the 316L-SLM build.

4. Results

Table 4.16: Height, spatial and hybrid parameters for the 100 mm s1 x+ band 2 surface before and after form removal.

Form removal	Sa [μm]	Sq [μm]	Sdr [-]	Sdq [-]	Ssk [-]	Sku [-]	Str [-]
Before	13.1	15.9	106	5.5	0.54	2.69	0.39
After	12.1	14.6	106	5.5	0.67	2.75	0.87

The second anomaly is from the measurements of the 20 mm s2 x- surface on the 316L-SLM and 410-SLM builds. The model is located in the center of the build. The images of the surface are shown in figure 4.20 and 4.21. The measurement area is 8.77 mm x 3.13 mm, covering the entire x- surface of the model. Both surfaces showed high peaks that come from the partly melted particles, higher than what is seen on the other measurements. Interestingly, the positions of the peaks are located at roughly the same position for both builds. From these peaks, both surfaces show an increased value of Ssk and Sku compared with the values from their own build. The height, spatial and hybrid parameters are shown in table 4.17.

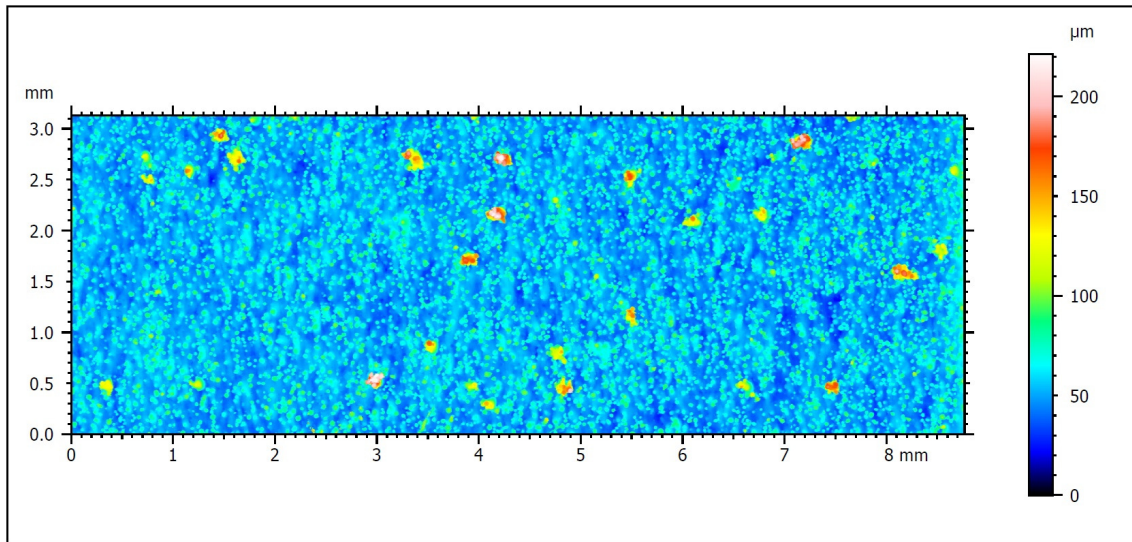


Figure 4.20: Surface area roughness image of 20 mm s2 x- from the 316L-SLM build.

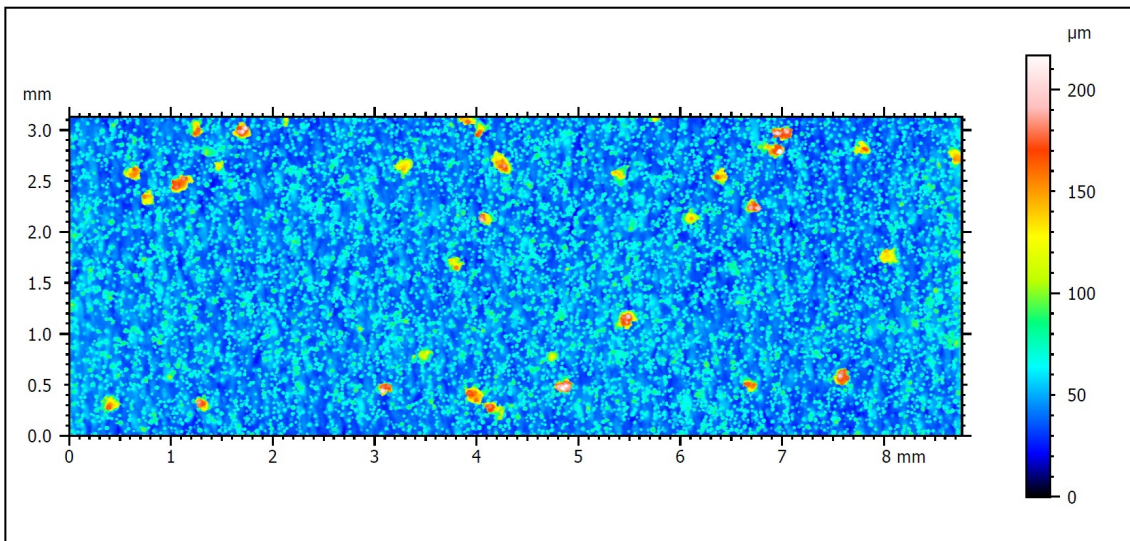


Figure 4.21: Surface area roughness image of 20 mm s2 x- from the 410-SLM build.

Ssk and Sku are sensitive to outliers such as high peaks. The skewness tells us that the height distribution is below the mean plane and the kurtosis indicates the presence of high peaks or valleys, in this case high peaks, which matches with what is seen in figure 4.20 and 4.21. Rest of the parameters remain similar to values from their individual build.

Table 4.17: Height, spatial and hybrid parameters for the 20 mm s2 x- surfaces from the 316L-SLM and 410-SLM builds.

	Sa [μm]	Sq [μm]	Sdr [-]	Sdq [-]	Ssk [-]	Sku [-]	Str [-]
316L-SLM	12.2	17.4	92	5.2	2.76	17.1	0.93
410-SLM	13.7	19.0	105	5.9	2.62	15.3	0.92

4.3 Microstructure and chemical analysis

This section contains the microstructure and chemical analysis result of the 316L-SLM build.

4.3.1 Microstructure difference at different positions and heights

All the polished samples were first investigated at the center of the cross-section with 50x magnification as shown in figure 4.22 and 4.23. At this magnification, all samples show an isotropic microstructure but no difference between locations and heights. Note that all of the lacks of fusion are enclosed with white rectangles in both SE image and BSE image of the samples at the same location.

4. Results

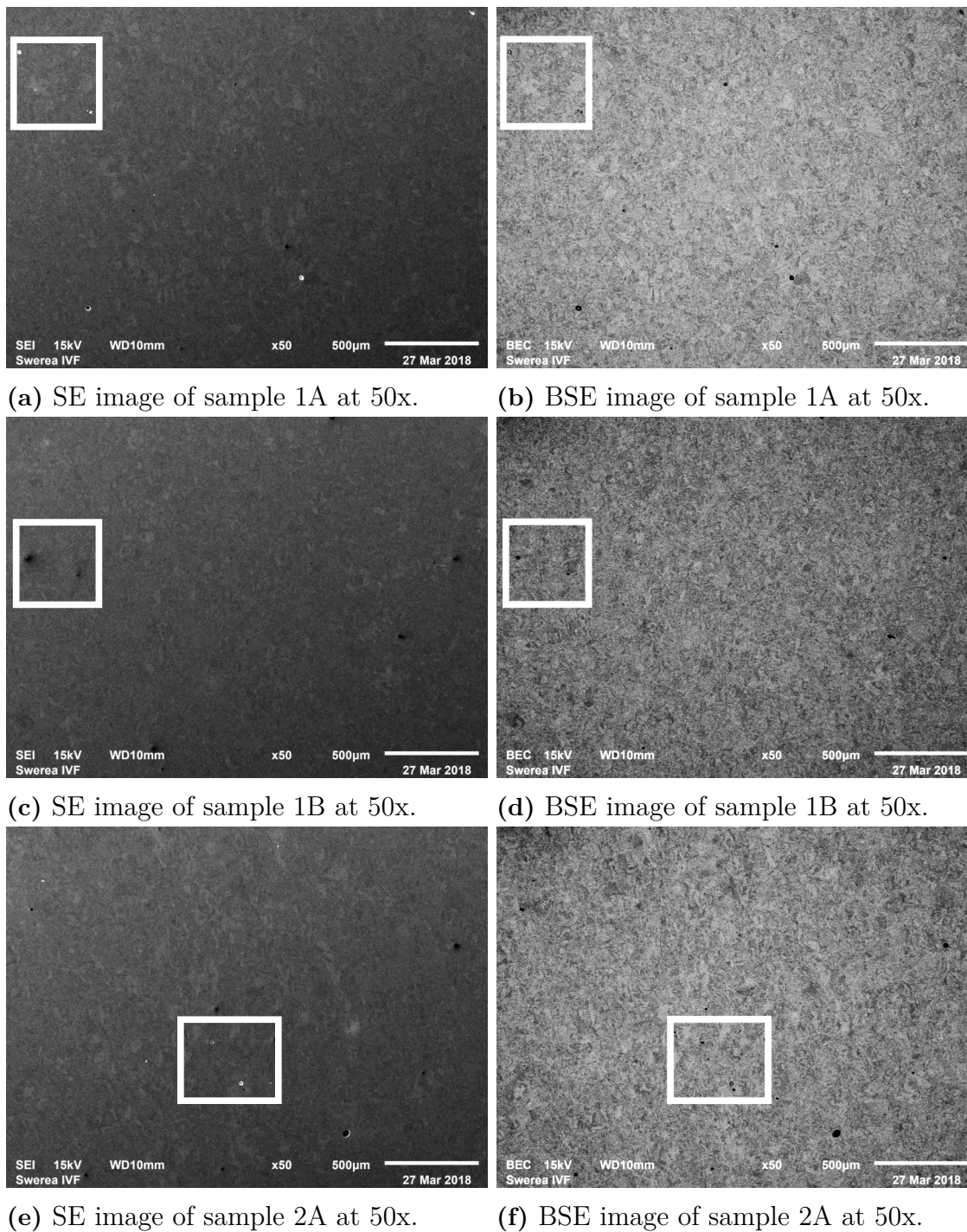


Figure 4.22: SE and BSE images of sample 1A, 1B and 2A at 50x magnification

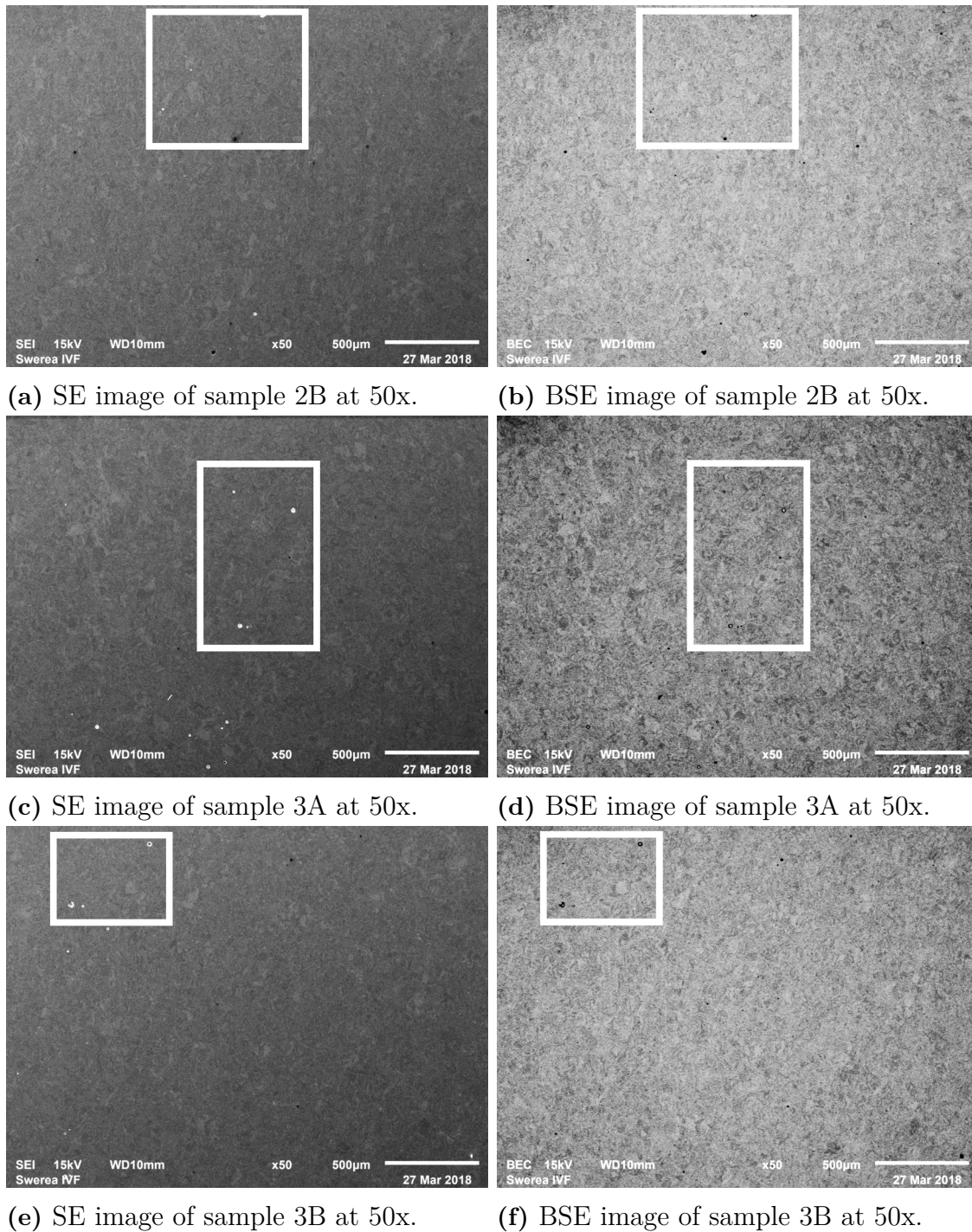


Figure 4.23: SE and BSE images of sample 2B, 3A and 3B at 50x magnification.

More images were taken at a higher magnification, 500x, in order to further the investigation. Sample 1B and sample 3A were chosen, due to the fact they are the samples furthest away from each other in the X-, Y- and Z-direction. The results are shown in figure 4.24

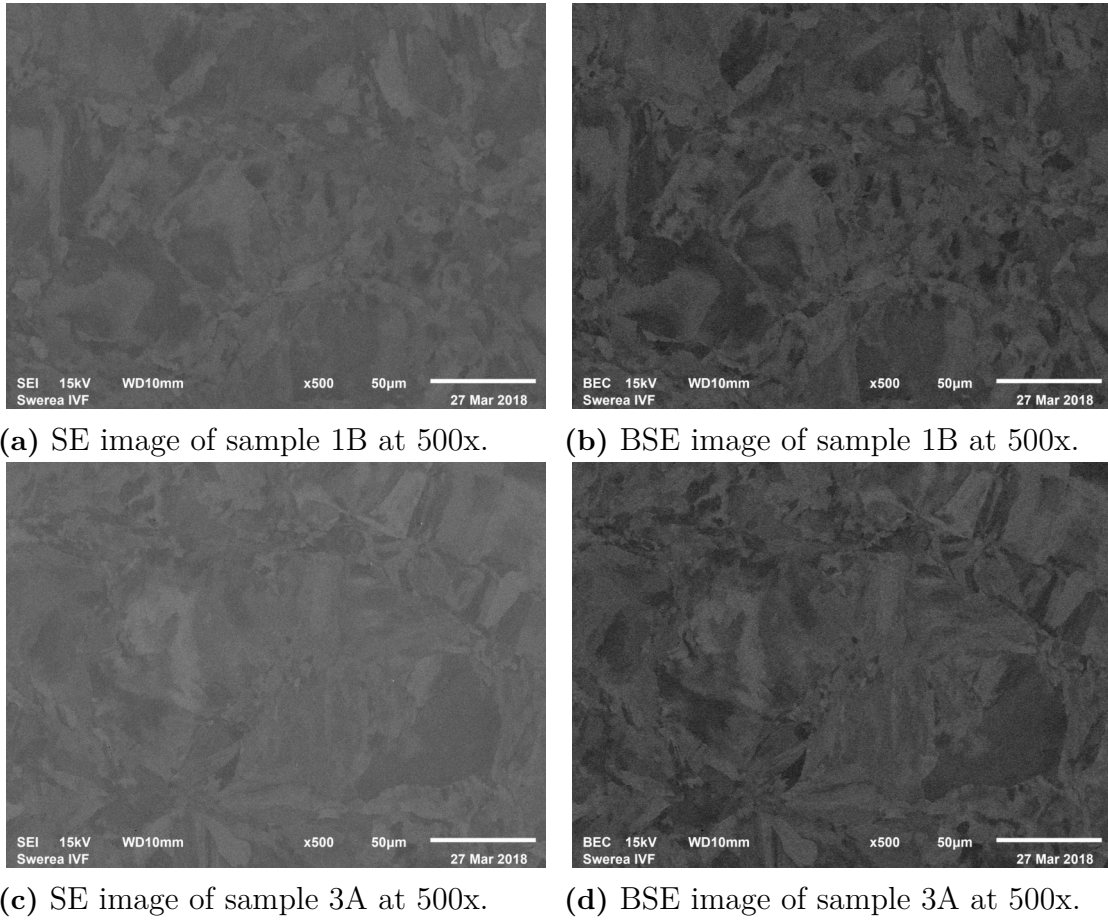


Figure 4.24: SE and BSE images of sample 1A, 1B and 2A at 50x magnification.

4.3.2 EDS spectrum and quantification

The quantification of the EDS spectrum taken on the six samples from the 316L build by the SLM 125 HL machine are presented in table 4.18. The values are shown in wt%. The spectra are taken using 50x magnification.

Table 4.18: Chemical composition of the 316L build.

Sample	Fe	Cr	Ni	Mo	C	Mn	S	Si	O
1A	65.1	16.4	12.4	2.3	1.6	1.4	0.0	0.7	0.1
1B	65.0	16.5	12.2	2.6	1.5	1.4	0.0	0.8	0.0
2A	65.0	16.6	12.4	2.2	1.6	1.4	0.1	0.7	0.0
2B	65.1	16.4	12.5	2.3	1.5	1.4	0.0	0.7	0.0
3A	65.1	16.4	12.5	2.3	1.6	1.4	0.1	0.7	0.0
3B	65.2	16.5	12.5	2.1	1.5	1.3	0.1	0.7	0.0

The six EDS spectra are compiled into a single figure shown in figure 4.25. Each individual spectrum is color coded according the legend in the figure. The spectra overlap each other due to their similarity in chemical composition, which is also shown in table 4.18.

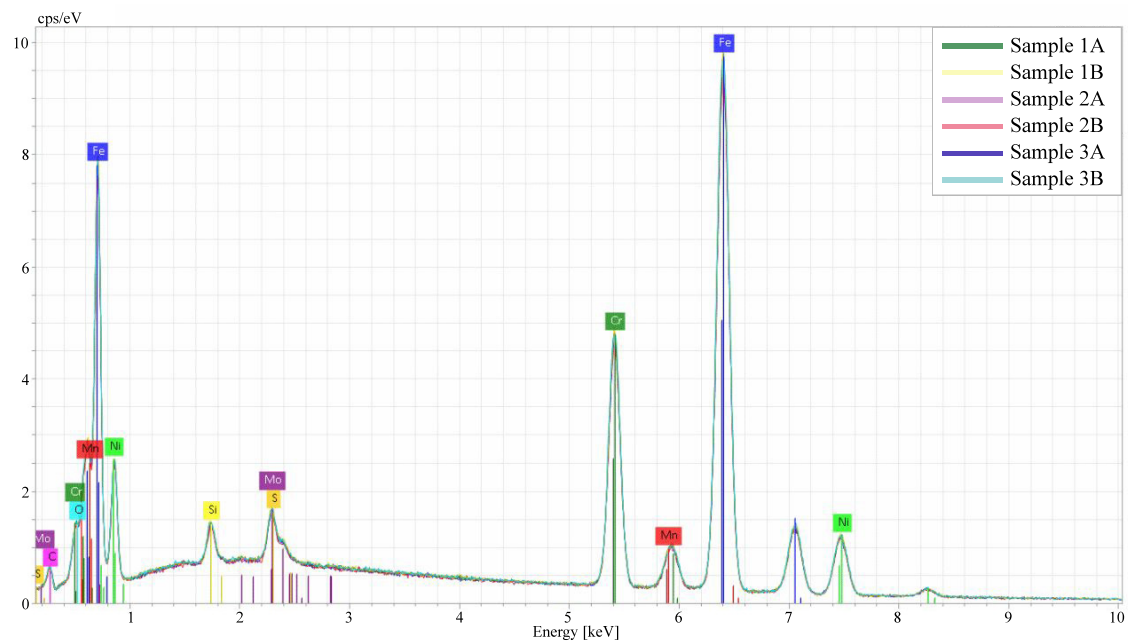
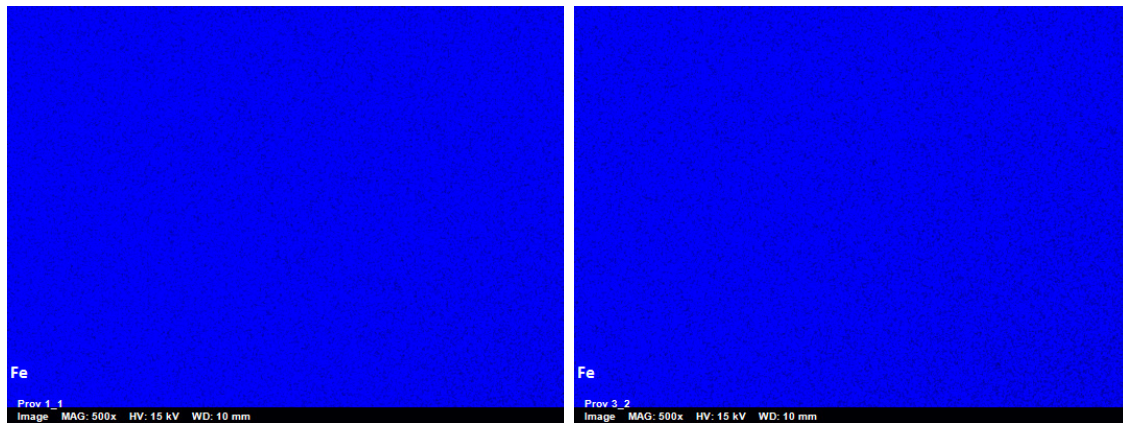


Figure 4.25: EDS spectra of the 316L build.

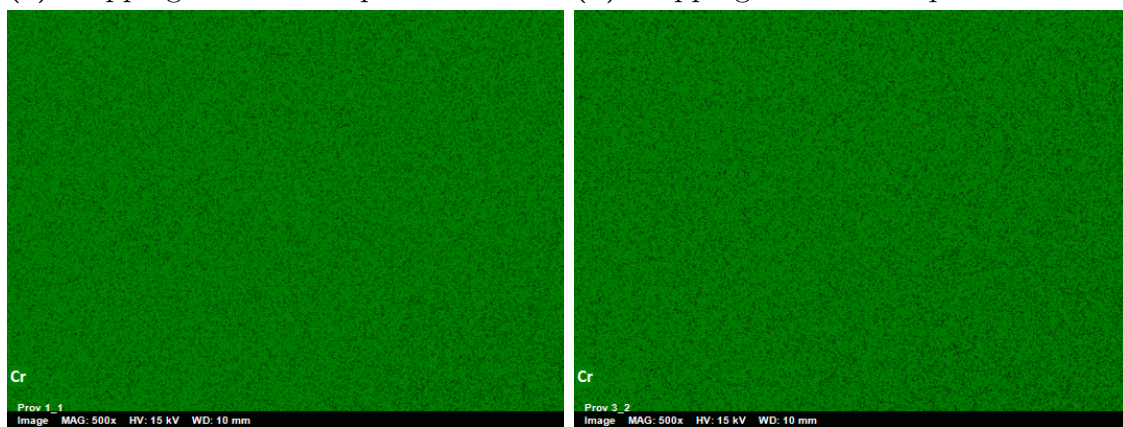
The result of the elemental mapping of samples 1B and 3A at 500x magnification are shown in figure 4.26, 4.27 and 4.28. Sample 1B is located on the left side of the figures and sample 3A is located on the right side of the figures. They are placed side by side for direct comparison. Figure 4.26 shows the elemental mapping for Fe, Cr and Ni. Figure 4.27 shows the elemental mapping for Mo, C, and Mn. Figure 4.28 shows the elemental mapping for S, Si and O. The mappings show an evenly distributed solid solution without, phase segregation.

4. Results



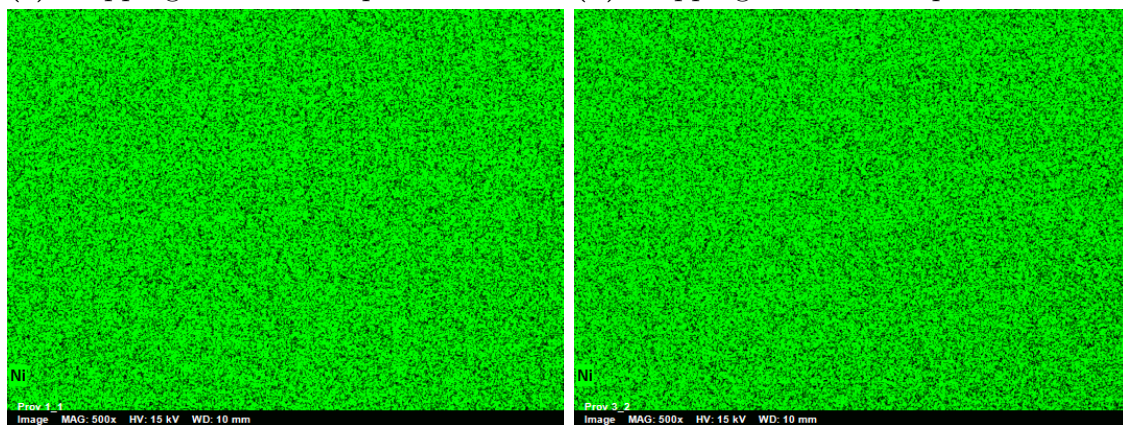
(a) Mapping of Fe in sample 1B.

(b) Mapping of Fe in sample 3A.



(c) Mapping of Cr in sample 1B.

(d) Mapping of Cr in sample 3A.



(e) Mapping of Ni in sample 1B.

(f) Mapping of Ni in sample 3A.

Figure 4.26: Elemental mapping of Fe, Cr and Ni in the 316L build by Swerea.

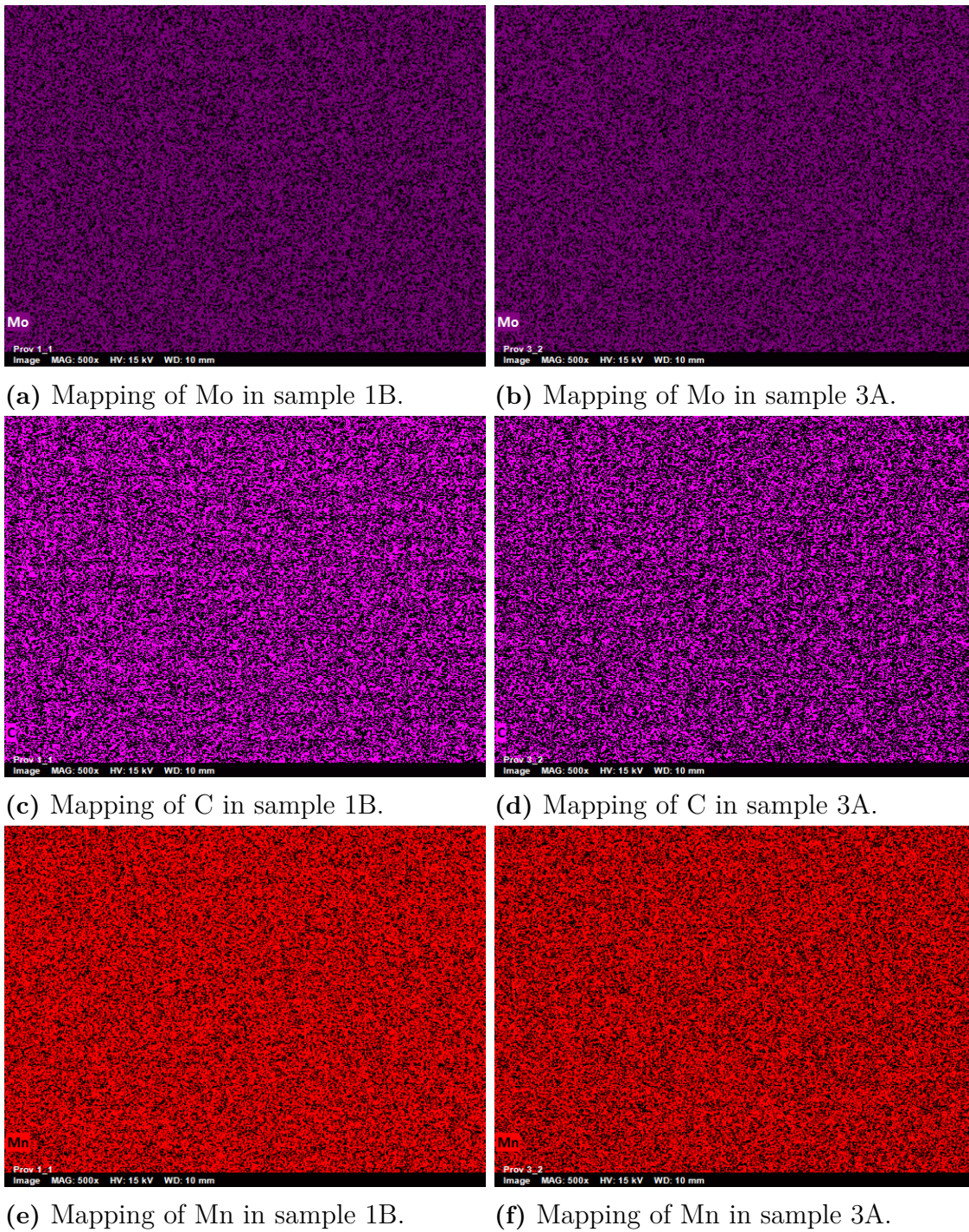


Figure 4.27: Elemental mapping of Mo, C and Mn in the 316L build by Swerea.

4. Results

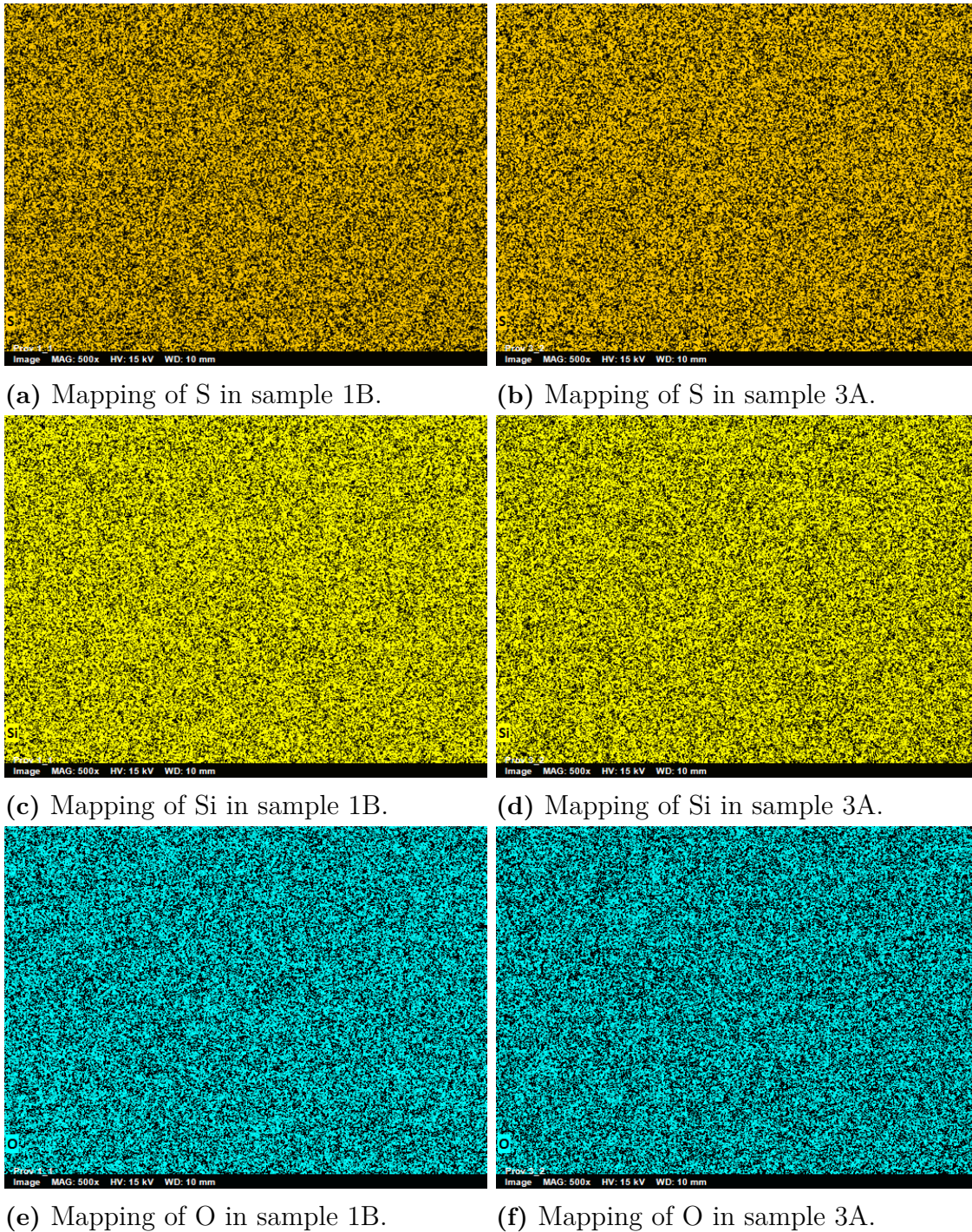


Figure 4.28: Elemental mapping of S, Si and O in the 316L build by Swerea.

No difference in the chemical composition and distribution in the 316L build was found by EDS analysis and elemental mapping. A decision was made to not continue performing chemical analysis on further builds as it would consume time without yielding any interesting results.

5

Conclusion

This chapter contains the conclusions of the methodology and the experimental work from the geometrical accuracy analysis, surface area roughness analysis and the microstructure and chemical composition analysis. Discussion of the methodology and recommendations is also included.

5.1 Methodology

This section contains the conclusion of the methodology:

1. The design of the test artifact depends on what is going to be answered; this thesis answers the dependency of height and location hence the build is designed as in figure 3.2.
2. Variation sensitivity should be validated through RD&T to ensure high stability for the chosen locating scheme; stability validation through RD&T is suggested and will work for other model as well.
3. If another model is designed with an intention to use with the 3D scanner, shadowing effect must be concerned in order to ensure a successful scanning.
4. Confocal fusion mode is recommended for AM samples for surface roughness profile acquisition because it yields low NMP and sufficient later resolution.
5. Manual selection of scanned mesh point cloud will contribute to the deviation in the final dimensions and positions of the fitted spheres.
6. For AM sample, the acquisition area for surface roughness does not need to be as large as the work in this thesis as the surface is mainly isotropic.

5.2 Geometrical accuracy of laser beam melting additive manufacturing

Results obtained from geometrical inspection has yielded the following conclusion:

1. General trend of X- and Y-direction deviation could be observed in SLM 125 HL and EOS M290.
2. The deviation in Z-direction is lower than for X- and Y-direction for all builds.
3. The selected method of acquiring the 3D scanned mesh file, 3D scanning, does not substantially contribute to the result of the geometrical inspection.

4. The way the locating scheme is defined determines the result of the geometrical inspection.
5. Current set of reference spheres cannot handle the case where the reference spheres themselves are deviated from their nominal positions from manufacturing process.

5.3 Surface area roughness of laser beam melting additive manufacturing

With the results from surface area roughness analysis in hand, following conclusions can be made:

1. Height, location or orientation of the surface does not affect Sa, Sq, Sdr, Sdq, Ssk, Sku and Str.
2. The surface texture is isotropic with many sharp peaks which lead to a larger surface area.
3. There is no significant difference in the parameter values between 316L and 410 built by the SLM machine.
4. There is a difference in the surface area roughness between the SLM machine and EOS using the same material with different process parameters and powder condition.
5. Surface anomalies with very high peaks at the same location and same orientation exists on the builds by the SLM machine.

It is worth noting that both 316L and 410 are stainless steels but 316L is austenitic and 410 is martensitic. The difference in the material might not be significant enough for the surface texture to be different from each other.

5.4 Microstructure and chemical composition

Following conclusions can be drawn from the material analysis result:

1. No microstructure and chemical composition differences from the different heights or positions were observed on the samples manufactured by SLM 125 HL.
2. Carbon content reported is significantly higher than the nominal value specified by the powder supplier. It is mainly because of the carbon contamination on the sample surfaces and because the powder supplier uses a different quantification technique with higher accuracy.

Due to time limit and lack of interesting results, 316L-EOS and 410-SLM were not analyzed in terms of microstructure and chemical composition.

5.5 Discussion

- The 3D scanning equipment by GOM acquired the geometry of the test model with sufficient accuracy for evaluating geometrical accuracy. There are however limitations on the technique. Sharp corners, shadowed parts and shiny surfaces usually yield data points with bad accuracy or missing data points. Precaution has to be taken when interpreting the scan results with those anomalies and the test model has to be designed with regards to the measurement technique used.
- The confocal fusion technique used at 20x magnification gives a good combination of measurement area, lateral resolution and NMP. Lower magnification yield a larger measurement area but lower lateral resolution, the other way around for higher magnification if the same technique is used. Vertical resolution is also improved with higher magnification. The confocal fusion option is available with 20x and 100x magnification in the Sensofar microscope but a compatible external ring light was not available for the 100x magnification.
- Focus variation technique can also analyze metal AM surfaces but yields a higher amount of NMP compared with the confocal fusion. Standard confocal microscopy and coherence scanning interferometry are not capable of capturing the steep angles on the side of the peaks present on the surfaces from metal AM parts, thus yield a high amount of NMP.
- SEM is more than capable for imaging microstructure at 50x and 500x magnification. EDS works good enough for comparing results within a build. EDS cannot quantify the chemical composition of the material with good enough accuracy to be able to compare with a nominal value or with another build. The sample preparation method produces samples good enough for the SEM usage as expected.
- The test artifact could be improved by adjusting the scale of the model to increase the amount of samples or add more samples for larger build plates. The cone angle can also be adjusted to increase the surface of the sphere for geometrical measurements.
- The origin of the surface roughness anomalies is unknown but they affect the parameter values locally. They appear at the same location for two different builds from the same machine. It is of interest to investigate further if anomalies are present in future print jobs and why they occur.
- The build volume test model's octagonal shape proved to be possible but difficult clamp onto for sectioning for the material analysis. It is recommended to use a conventional square model if analyzing microstructure and chemical composition is the main priority.
- The test model dictates what can be analyzed. E.g. the current build volume test model is limited to analyzing surface roughness on the vertical surfaces whereas horizontal surfaces and surfaces at an angle are not possible. A model has to be designed with the research question in mind. If analyzing surface roughness is the main priority then the model needs to include the possibility to analyze horizontal and angled surfaces.

Bibliography

- [1] Mats Deleryd. “Process capability studies in theory and practice”. Licentiate Thesis. Luleå University of Technology, June 1996.
- [2] Leonard A. Doty. *Statistical process control*. 2. ed. New York: Industrial Press, 1996. ISBN: 0-8311-3069-5 ;
- [3] *ASME Y14.5 - 2009 Dimensioning and Tolerancing*. ASME, 2009.
- [4] Gene R. Cogorno. *Geometric dimensioning and tolerancing for mechanical design*. English. 2nd. New York: McGraw-Hill, 2011. ISBN: 9780071772129;
- [5] Shawn Moylan et al. “An Additive Manufacturing Test Artifact”. English. In: *Journal of Research of the National Institute of Standards and Technology* 119 (2014), pp. 429–459. ISSN: 1044-677X.
- [6] Lara Rebaioli and Irene Fassi. “A review on benchmark artifacts for evaluating the geometrical performance of additive manufacturing processes”. English. In: *The International Journal of Advanced Manufacturing Technology* 93.5 (2017), pp. 2571–2598. ISSN: 1433-3015.
- [7] Wen Shifeng et al. “Effect of molten pool boundaries on the mechanical properties of selective laser melting parts”. In: 214 (Nov. 2014), pp. 2660–2667. ISSN: 0924-0136.
- [8] Bo Cheng, Subin Shrestha, and Kevin Chou. “Stress and deformation evaluations of scanning strategy effect in selective laser melting”. In: *Additive Manufacturing* 12 (2016). Special Issue on Modeling & Simulation for Additive Manufacturing, pp. 240–251. ISSN: 2214-8604.
- [9] Luke N. Carter et al. “The influence of the laser scan strategy on grain structure and cracking behaviour in SLM powder-bed fabricated nickel superalloy”. In: *Journal of Alloys and Compounds* 615 (2014), pp. 338–347. ISSN: 0925-8388.
- [10] Kai Guan et al. “Effects of processing parameters on tensile properties of selective laser melted 304 stainless steel”. In: 50 (Sept. 2013), pp. 581–586. ISSN: 0261-3069.
- [11] Christ P. Paul et al. “Investigating laser rapid manufacturing for Inconel-625 components”. In: *Optics Laser Technology* 39 (June 2007), pp. 800–805. ISSN: 0030-3992.
- [12] Lore Thijs et al. “A study of the microstructural evolution during selective laser melting of Ti–6Al–4V”. In: *Acta Materialia* 58.9 (2010), pp. 3303–3312. ISSN: 1359-6454.
- [13] Loong E. Loh et al. “Effect of laser beam profile on melt track in Selective Laser Melting”. In: (Jan. 2014), pp. 83–87.
- [14] Sheng Zhang et al. “Effects of Powder Characteristics on Selective Laser Melting of 316L Stainless Steel Powder”. In: *Manufacturing Process Technology*.

- Vol. 189. Advanced Materials Research. Trans Tech Publications, Apr. 2011, pp. 3664–3667.
- [15] Jun H. Tan, Wai L. E. Wong, and Kenneth W. Dalgarno. “An overview of powder granulometry on feedstock and part performance in the selective laser melting process”. In: *Additive Manufacturing* 18 (2017), pp. 228–255. ISSN: 2214-8604.
- [16] Rainer J. Hebert. “Viewpoint: metallurgical aspects of powder bed metal additive manufacturing”. In: *Journal of Materials Science* 51.3 (Feb. 2016), pp. 1165–1175. ISSN: 1573-4803.
- [17] Ruidi Li et al. “Balling behavior of stainless steel and nickel powder during selective laser melting process”. In: *The International Journal of Advanced Manufacturing Technology* 59.9 (Apr. 2012), pp. 1025–1035. ISSN: 1433-3015.
- [18] Adriaan B. Spierings and Gideon Levy. “Comparison of Density of Stainless Steel 316L Parts Produced with Selective Laser Melting Using Different Powder Grades”. en. In: *Solid freeform fabrication proceedings : August 2009*. Ed. by David L. Bourell et al. SFF Symposium 2009; Conference Location: Austin, Texas, USA; Conference Date: August 3-5, 2009; . University of Texas at Austin, 2009, pp. 342–353.
- [19] Henry H. Hausner. “Friction Conditions in a Mass of Metal Powder.” In: *Int. J. Powder Met., 3: No. 4, 7-13(Oct. 1967)*. (1967).
- [20] Eugene Hecht. *Optics*. Pearson, 2016. ISBN: 9780133977226.
- [21] Marco Grasso and Bianca M. Colosimo. “Process defects and in situ monitoring methods in metal powder bed fusion: a review”. In: *Measurement Science and Technology* 28.4 (2017), p. 044005.
- [22] Anil Kumar Sinha. *Defects and Distortion in Heat-Treated Parts, Heat Treating, ASM Handbook*. Vol. 4. 1991, pp. 601–619.
- [23] Tognola Gabriella et al. “A fast and reliable system for 3D surface acquisition and reconstruction”. In: *Image and Vision Computing* 21.3 (2003), pp. 295–305.
- [24] Rikard Söderberg and Lars Lindkvist. “Computer Aided Assembly Robustness Evaluation”. In: *Journal of Engineering Design* 10.2 (1999), pp. 165–181.
- [25] Richard Leach. *Optical Measurement of Surface Topography*. Springer Berlin Heidelberg, 2011. ISBN: 9783642120121.
- [26] Aitor Matilla et al. “Three-dimensional measurements with a novel technique combination of confocal and focus variation with a simultaneous scan”. In: *Proc SPIE* 9890 (2016).
- [27] Richard Leach. *Characterisation of areal surface texture*. June 2013.
- [28] Joseph Goldstein. *Scanning Electron Microscopy and X-ray Microanalysis: A Text for Biologists, Materials Scientists, and Geologists*. Plenum Press, 1992. ISBN: 9780306441752.

A

Appendix 1

A.1 Geometrical inspection

This section contains the raw data regarding the deviation of the position of the center point of each sphere as well as the diameter deviation of the sphere in Alignment 1 and Alignment 2.

A.1.1 316L-SLM; Alignment 1

Sample	dX	dY	dZ	dD
-	μm	μm	μm	μm
316L SLM 20 mm 1	-0.116	-0.07	-0.01	-0.133
316L SLM 20 mm 2	0.078	-0.127	-0.02	-0.132
316L SLM 20 mm 3	0.289	-0.179	0.009	-0.135
316L SLM 60 mm 1	-0.041	-0.043	-0.049	-0.134
316L SLM 60 mm 2	0.154	-0.098	-0.06	-0.126
316L SLM 60 mm 3	0.133	0.242	-0.054	-0.115
316L SLM 100 mm 1	0.034	-0.021	-0.014	-0.007
316L SLM 100 mm 2	0.216	0.147	-0.076	-0.114
316L SLM 100 mm 3	0.402	0.103	-0.058	-0.122

A.1.2 316L-EOS; Alignment 1

Sample	dX	dY	dZ	dD
-	μm	μm	μm	μm
316L EOS 20 mm 1	-0.382	-0.047	0.004	0.034
316L EOS 20 mm 2	-0.196	-0.095	0	0.032
316L EOS 20 mm 3	-0.015	-0.139	0.001	0.039
316L EOS 60 mm 1	-0.348	-0.159	-0.06	0.042
316L EOS 60 mm 2	-0.163	-0.197	-0.07	0.044
316L EOS 60 mm 3	-0.152	0.075	-0.074	0.037
316L EOS 100 mm 1	-0.342	-0.28	-0.125	0.039
316L EOS 100 mm 2	-0.315	0.012	-0.145	0.035
316L EOS 100 mm 3	-0.145	-0.038	-0.154	0.041

A.1.3 410-SLM; Alignment 1

Sample	dX	dY	dZ	dD
-	μm	μm	μm	μm
410 20 mm 1	0.117	-0.038	-0.008	-0.055
410 20 mm 2	0.192	-0.065	0.003	-0.058
410 20 mm 3	0.269	-0.078	-0.005	-0.047
410 60 mm 1	0.149	0.064	0.002	-0.063
410 60 mm 2	0.235	0.048	0.013	-0.057
410 60 mm 3	0.256	0.191	0.02	-0.05
410 100 mm 1	0.351	0.009	0.022	-0.07
410 100 mm 2	0.384	0.174	0.026	-0.067
410 100 mm 3	0.462	0.154	0.013	-0.061

A.1.4 316L-SLM; Alignment 2

Sample	dX	dY	dZ	dD
-	μm	μm	μm	μm
316L SLM 20 mm 1	-0.122	-0.028	-0.01	-0.133
316L SLM 20 mm 2	0	-0.157	-0.02	-0.132
316L SLM 20 mm 3	0.138	-0.282	0.009	-0.135
316L SLM 60 mm 1	-0.119	0	-0.049	-0.134
316L SLM 60 mm 2	0.003	-0.128	-0.06	-0.126
316L SLM 60 mm 3	0.127	0.139	-0.054	-0.115
316L SLM 100 mm 1	0.011	-0.012	-0.009	-0.013
316L SLM 100 mm 2	0.21	0.118	-0.076	-0.114
316L SLM 100 mm 3	0.323	0	-0.058	-0.122

A.1.5 316L-EOS; Alignment 2

Sample	dX	dY	dZ	dD
-	μm	μm	μm	μm
316L EOS 20 mm 1	-0.125	0.112	0.004	0.034
316L EOS 20 mm 2	0	0.004	0	0.032
316L EOS 20 mm 3	0.121	-0.101	0.001	0.039
316L EOS 60 mm 1	-0.151	0	-0.06	0.042
316L EOS 60 mm 2	-0.027	-0.098	-0.07	0.044
316L EOS 60 mm 3	0.105	0.113	-0.074	0.037
316L EOS 100 mm 1	-0.206	-0.121	-0.125	0.039
316L EOS 100 mm 2	-0.058	0.111	-0.145	0.035
316L EOS 100 mm 3	0.052	0	-0.154	0.041

A.1.6 410-SLM; Alignment 2

Sample	dX	dY	dZ	dD
-	μm	μm	μm	μm
410 20 mm 1	-0.03	-0.102	-0.008	-0.055
410 20 mm 2	0	-0.174	0.003	-0.058
410 20 mm 3	0.031	-0.232	-0.005	-0.047
410 60 mm 1	-0.043	0	0.002	-0.063
410 60 mm 2	-0.003	-0.061	0.013	-0.057
410 60 mm 3	0.108	0.038	0.02	-0.05
410 100 mm 1	0.113	-0.054	0.022	-0.07
410 100 mm 2	0.236	0.065	0.026	-0.067
410 100 mm 3	0.269	0	0.013	-0.061

A.2 Surface area roughness measurements

This section contains the raw data from the surface area roughness measurements.

A.2.1 316L-SLM

Sample	Direction	Sa	Sq	Sdr	Sdq	Ssk	Sku	Str	NMP ratio
-	-	μm	μm	-	-	-	-	-	-
316L SLM 20 mm 1	x+	11.57	14.24	93.98	5.07	0.83	3.19	0.76	1.02
	x-	9.93	12.61	96.85	4.91	1.12	3.75	0.79	0.4
	y+	9.95	12.31	90.07	4.7	0.89	3.16	0.86	0.28
	y-	11.96	14.86	96.18	5	0.84	3.3	0.74	0.35
316L SLM 20 mm 2	x+	10.84	13.73	85.72	4.8	1.05	3.67	0.77	0.65
	x-	11.47	15.95	98.82	5.24	2.55	17.18	0.87	0.39
	y+	11.22	13.95	102.56	5.38	0.97	3.52	0.78	0.48
	y-	10.96	13.9	90.91	4.97	1.09	3.95	0.77	0.48
316L SLM 20 mm 3	x+	9.88	12.65	83.47	4.57	1.08	3.78	0.8	0.24
	x-	9.41	12.03	90.73	4.59	1.03	3.92	0.71	0.28
	y+	10.67	13.58	96.59	5.03	1.01	3.79	0.72	0.45
	y-	10.11	12.66	92.79	4.69	0.95	3.6	0.8	0.32
316L SLM 60 mm 1	x+	13.28	16.17	106.45	5.56	0.55	2.78	0.74	0.7
	x-	11.85	14.74	106.6	5.56	0.95	3.38	0.76	0.48
	y+	12.85	15.39	124.75	6.25	0.75	2.82	0.8	0.78
	y-	12.1	14.93	103.88	5.6	0.9	3.28	0.8	0.42
316L SLM 60 mm 2	x+	13.27	16.07	116.05	6.04	0.68	2.83	0.83	0.87
	x-	12.47	15.55	105.5	5.72	1.14	4.99	0.71	0.74
	y+	12.92	15.66	113.7	5.88	0.77	2.97	0.8	0.76
	y-	11.84	14.52	103.43	5.47	0.87	3.2	0.82	0.68
316L SLM 60 mm 3	x+	12.31	14.97	122.25	6.15	0.61	2.76	0.75	0.64
	x-	11.66	14.2	111.74	5.39	0.74	3	0.83	0.47
	y+	10.94	13.35	112.56	5.56	0.9	3.19	0.84	0.33
	y-	12.77	15.49	118.69	5.91	0.72	2.96	0.78	0.71
316L SLM 100 mm 1	x+	12.46	14.93	115.87	5.93	0.66	2.67	0.77	0.6
	x-	11.19	13.71	96.8	5.21	0.96	3.2	0.84	0.44
	y+	12.06	14.63	106.26	5.64	0.84	3.02	0.8	0.63
	y-	11.09	13.71	92.51	5.08	0.79	3.12	0.7	0.38
316L SLM 100 mm 2	x+	12.26	14.69	96.46	5.14	0.66	2.69	0.82	0.88
	x-	12.59	15.38	101.48	5.45	1.01	3.92	0.84	0.6
	y+	11.35	13.81	96.64	5.03	0.79	3.26	0.78	0.44
	y-	12.8	15.42	109.34	5.54	0.62	2.78	0.77	0.71
316L SLM 100 mm 3	x+	12.5	14.95	106.52	5.78	0.75	2.69	0.81	1.38
	x-	12.08	14.41	104.06	5.54	0.67	2.67	0.85	0.74
	y+	11.79	14.23	102.44	5.49	0.76	2.85	0.78	0.74
	y-	12.18	14.94	104.22	5.56	0.74	3	0.74	0.88

A.2.2 316L-EOS

Sample	Direction	Sa	Sq	Sdr	Sdq	Ssk	Sku	Str	NMP ratio
-	-	μm	μm	-	-	-	-	-	-
316L EOS 20 mm 1	x+	15.47	19.36	151.64	6.69	0.9	3.88	0.83	1.33
	x-	17.75	21.98	172.36	7.6	0.77	3.45	0.9	2.04
	y+	16.05	20.96	144.78	6.49	1.19	5.35	0.92	1.2
	y-	16.38	20.08	172.42	7.39	0.7	3.22	0.91	1.18
316L EOS 20 mm 2	x+	17.43	21.83	181.99	7.75	0.86	3.97	0.88	1.3
	x-	17.35	21.5	205.15	8.19	0.74	3.51	0.89	1.2
	y+	17.32	22.28	194.01	7.94	1.09	5.05	0.89	1.14
	y-	16.83	20.81	203.43	8.05	0.73	3.52	0.9	1.17
316L EOS 20 mm 3	x+	18.98	23.77	166.99	7.85	0.92	4.04	0.94	1.74
	x-	16.93	21.25	178.18	7.51	0.89	3.88	0.84	1.62
	y+	16.91	21.47	155.84	6.91	1.08	5.07	0.91	1.63
	y-	17.56	21.86	167.97	7.57	0.83	3.87	0.92	1.78
316L EOS 60 mm 1	x+	16.28	20.34	176.46	7.35	0.8	4.1	0.8	0.81
	x-	18.29	22.87	189.43	8.05	0.78	3.92	0.89	2.13
	y+	17.24	22.03	177	7.61	0.9	4.82	0.89	2
	y-	16.66	20.44	183.05	7.66	0.6	3.19	0.9	1.77
316L EOS 60 mm 2	x+	17.63	21.94	173.43	7.65	0.79	3.79	0.94	2.14
	x-	18.05	22.48	195.58	8.18	0.73	3.54	0.89	1.9
	y+	17.36	22.11	180.12	7.6	0.95	4.71	0.91	1.93
	y-	17.45	21.53	185.64	7.71	0.65	3.28	0.96	1.78
316L EOS 60 mm 3	x+	17.71	22	180.81	7.85	0.69	3.56	0.88	2.12
	x-	16.28	20.42	181.47	7.61	0.77	4.05	0.89	1.6
	y+	16.27	20.83	151.55	6.88	0.75	4.34	0.95	2.22
	y-	15.19	18.7	166.98	6.94	0.62	3.19	0.9	1.25
316L EOS 100 mm 1	x+	17.48	21.77	156.51	7.2	0.84	3.9	0.87	2.1
	x-	19	23.73	183.36	8.09	0.61	3.51	0.9	3.28
	y+	16.07	20.35	152.91	6.63	1.01	4.4	0.94	1.48
	y-	17.41	21.46	171.4	7.43	0.64	3.18	0.94	1.94
316L EOS 100 mm 2	x+	17.26	21.32	183.56	7.72	0.69	3.44	0.89	1.83
	x-	16.56	20.5	183.68	7.58	0.68	3.41	0.88	1.62
	y+	16.84	21.75	182.71	7.57	1.03	5.45	0.84	1.68
	y-	16.2	19.94	168.59	7.2	0.67	3.16	0.89	1.47
316L EOS 100 mm 3	x+	17.93	22.55	159.33	7.15	0.94	4.28	0.91	2.02
	x-	16.04	19.78	163.1	7.12	0.7	3.55	0.85	1.89
	y+	16.84	21.14	174.64	7.33	0.86	3.99	0.89	1.59
	y-	16.45	20.33	160.86	7.01	0.76	3.37	0.91	1.72

A.2.3 410-SLM

Sample	Direction	Sa	Sq	Sdr	Sdq	Ssk	Sku	Str	NMP ratio
-	-	μm	μm	-	-	-	-	-	-
410 SLM 20 mm 1	x+	11.78	14.11	104.98	5.52	0.68	2.64	0.8	1.75
	x-	10.61	13.05	92.66	5.06	0.94	3.11	0.81	0.79
	y+	11.69	14.03	117.63	5.99	0.9	3.24	0.8	0.77
	y-	13.05	15.74	114.12	6.08	0.65	2.75	0.71	1.39
410 SLM 20 mm 2	x+	10.76	13.26	88.16	5.02	0.95	3.28	0.84	1.67
	x-	12.95	16.7	106.74	5.78	1.96	11.67	0.82	1.44
	y+	12.04	14.34	110.42	5.9	0.74	2.67	0.83	1.62
	y-	12.95	15.42	116.64	6.1	0.67	2.68	0.74	1.49
410 SLM 20 mm 3	x+	10.66	13.14	108.18	5.62	0.89	3.17	0.82	0.26
	x-	10.84	13.21	115.16	5.74	0.85	3.12	0.83	0.28
	y+	12.4	14.97	135.63	6.66	0.77	3.12	0.81	0.54
	y-	11.6	13.9	129.77	6.35	0.74	2.78	0.81	0.31
410 SLM 60 mm 1	x+	13.14	15.55	124.85	6.39	0.59	2.51	0.82	0.85
	x-	13.43	15.81	132	6.85	0.74	2.59	0.82	0.75
	y+	13.1	15.46	133.01	6.61	0.65	2.57	0.83	1.12
	y-	12.56	15.1	116.21	6.07	0.7	2.79	0.77	0.71
410 SLM 60 mm 2	x+	14.2	16.64	157.87	7.42	0.5	2.35	0.85	0.52
	x-	12.79	15.22	119.14	6.36	0.82	3.15	0.85	0.76
	y+	13.44	15.94	130.33	6.63	0.66	2.65	0.82	0.56
	y-	13.15	15.75	128.6	6.67	0.83	3.33	0.82	0.62
410 SLM 60 mm 3	x+	13.33	15.62	132.9	6.76	0.55	2.4	0.87	1.5
	x-	12.61	14.95	119.67	6.24	0.68	2.61	0.85	0.68
	y+	13.22	15.39	119.53	6.08	0.6	2.38	0.87	1.45
	y-	13.15	15.72	127.25	6.41	0.62	2.64	0.79	0.96
410 SLM 100 mm 1	x+	12.77	15.28	116.26	5.92	0.63	2.63	0.8	1.62
	x-	11.62	14.1	101.38	5.29	0.84	2.87	0.82	0.66
	y+	11.93	14.28	114.07	5.69	0.68	2.72	0.84	1.49
	y-	12.21	14.89	110.81	5.73	0.93	3.93	0.79	1.13
410 SLM 100 mm 2	x+	12.12	14.45	108.57	5.62	0.62	2.52	0.88	1.13
	x-	12.52	14.93	116.06	5.88	0.74	2.97	0.8	1.36
	y+	11.31	13.7	106.15	5.42	0.81	3.07	0.69	1.25
	y-	12.25	14.79	117.14	5.73	0.64	2.78	0.77	1.19
410 SLM 100 mm 3	x+	12.69	15.24	130.45	6.34	0.75	2.87	0.8	0.96
	x-	11.78	14.27	116.23	5.76	0.79	2.86	0.82	0.8
	y+	11.67	14.12	119.12	5.81	0.78	2.87	0.78	0.88
	y-	12.17	14.76	126.42	6.04	0.8	3.15	0.8	0.92